On-Chip Integrated Label-Free Optical Biosensing

Thesis by

Jacob Benjamin Sendowski

In Partial Fulfillment of the Requirements

for the Degree of

Doctor of Philosophy

California Institute of Technology

Pasadena, California

2013

(Defended May 28, 2013)

For my parents

Acknowledgments

I would like to thank the many friends, colleagues, and mentors who have helped to guide me through my education and have aided in the production of this work. Firstly, I would like to acknowledge Professor Amnon Yariv, my academic advisor, for bringing me into his research group and allowing me to join the great legacy of students and work that have emerged from it. His guidance, suggestions, and leadership have helped me grow as a researcher. I would like to thank Professor Richard Flagan for approaching our group with the idea of collaborating on the label-free optical biosensing project, and for his help and guidance on that undertaking. Thanks to Professor Scott Fraser for his support, ideas, and consultations on the project. I would also like to thank Professor Bruno Crosignani for his support, encouragement, and for livening up weekly group meetings.

I would like to thank my colleagues and fellow group members with whom I have had the privilege of working closely. Firstly, former group member and mentor Professor Avi Zadok for taking me under his wing in the laboratory during my first two years as a student. My friend and collaborator Dr. Naresh Satyan who helped me further develop my experimental skills and with whom I have enjoyed exploring the natural beauty of Southern California. I have enjoyed working on the swept frequency laser and related projects with Arseny Vasilyev as well as our many interesting discussions. I am truly grateful for the opportunity to have worked with my friend, roommate, and collaborator, Christos Santis, whose efforts on the fabrication of the microdisk resonators made this work possible. I also enjoyed working with Dr. Jason Gamba on the initial phases of this work.

I would also like to thank my friends from the Yariv group past and present who

have been an important part of my time at Caltech. I have enjoyed many fruitful discussions, Friday afternoon coffee breaks, dinners, and off campus excursions with Yasha Vilenchik , Scott Steger, Mark Harfouche, Sinan Zhao, Dr. Hsi-Chun Liu, and Dr. Xian-Kai Sun. I would also like to thank Dr. Reginald Lee and Dr. George Rakuljic for helpful discussions and suggestions.

More recently I have had the pleasure of working closely with Marilena Dimotsantou, and Dongwan Kim who have contributed to recent progress on this work in chemistry and biology and who will be continuing on with the label-free biosensing project.

Thanks to the Caltech and Yariv group staff for keeping the lab running. Particularly to Connie Rodriguez for her help placing orders, keeping us organized, and for taking care of group. I would also like to thank Ali Ghaffari for his training on microfluidic fabrication and general encouragement.

Finally, I would like to thank my friend and surfing buddy Branden Williams for helping me get out of the lab a little bit and for teaching me to take some risks. Thanks to my parents, brother, and family for their love and unwavering support of all of my academic endeavors. I would also like to thank my grandfather, Jack Sendowski, for helping to sow the seeds of my scientific curiosity and love of building things.

Abstract

This thesis investigates the design and implementation of a label-free optical biosensing system utilizing a robust on-chip integrated platform. The goal has been to transition optical micro-resonator based label-free biosensing from a laborious and delicate laboratory demonstration to a tool for the analytical life scientist. This has been pursued along four avenues: (1) the design and fabrication of high-Q integrated planar microdisk optical resonators in silicon nitride on silica, (2) the demonstration of a high speed optoelectronic swept frequency laser source, (3) the development and integration of a microfluidic analyte delivery system, and (4) the introduction of a novel differential measurement technique for the reduction of environmental noise.

The optical part of this system combines the results of two major recent developments in the field of optical and laser physics: the high-Q optical resonator and the phase-locked electronically controlled swept-frequency semiconductor laser. The laser operates at a wavelength relevant for aqueous sensing, and replaces expensive and fragile mechanically-tuned laser sources whose frequency sweeps have limited speed, accuracy and reliability. The high-Q optical resonator is part of a monolithic unit with an integrated optical waveguide, and is fabricated using standard semiconductor lithography methods. Monolithic integration makes the system significantly more robust and flexible compared to current, fragile embodiments that rely on the precarious coupling of fragile optical fibers to resonators. The silicon nitride on silica material system allows for future manifestations at shorter wavelengths. The sensor also includes an integrated microfluidic flow cell for precise and low volume delivery of analytes to the resonator surface. We demonstrate the refractive index sensing action of the system as well as the specific and nonspecific adsorption of proteins

onto the resonator surface with high sensitivity. Measurement challenges due to environmental noise that hamper system performance are discussed and a differential sensing measurement is proposed, implemented, and demonstrated resulting in the restoration of a high performance sensing measurement.

The instrument developed in this work represents an adaptable and cost-effective platform capable of various sensitive, label-free measurements relevant to the study of biophysics, biomolecular interactions, cell signaling, and a wide range of other life science fields. Further development is necessary for it to be capable of binding assays, or thermodynamic and kinetics measurements; however, this work has laid the foundation for the demonstration of these applications.

Contents

List of Figures

List of Tables

Chapter 1

Overview

1.1 Introduction

Optical biosensing has proven to be an important enabling technology for biochemical characterization and analysis in the life sciences. Many optical biosensing systems exhibit high sensitivity and specificity in the detection and analysis of the interaction of chemicals or biomolecules of interest. These attributes portend the potential impact of optical biosensing in applications such as medical diagnostics and analytical chemistry and biology. Established commercial optical biosensing techniques exist; however, these commercial approaches are of limited sensitivity and/or high cost.

Nascent label-free optical sensing techniques employing optical micro-resonators have demonstrated performance beyond the capabilities of commercially available systems. Several signal pathways exist, though the majority of optical resonator sensors are essentially refractive index (RI) transducers. These systems measure changes in the resonant frequency of a high quality optical resonator that occur when a target analyte molecule binds to the resonator surface perturbing the refractive index of the optical mode. Various measurements can be performed with such a system including binding assays, chemical detection, and association/dissociation kinetics. Additionally, many optical micro-resonator sensor architectures are rooted in semiconductor materials and processing and therefore posses the potential for integration and wafer scale fabrication.

This work develops and demonstrates a label-free optical biosensing instrument

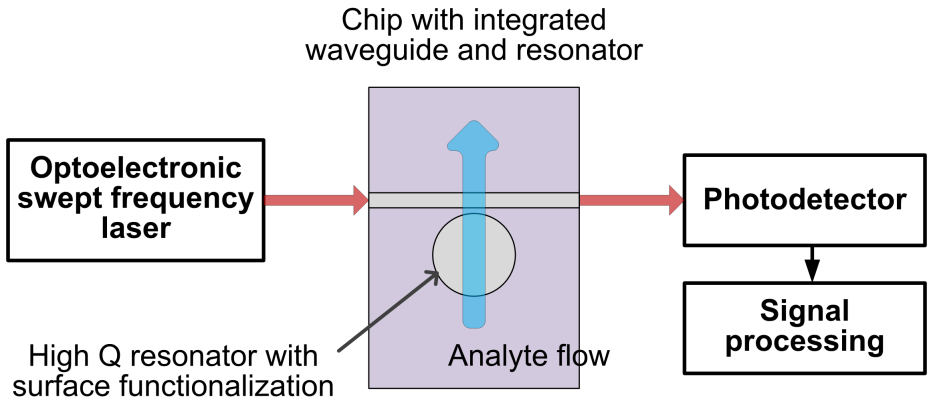

Figure 1.1: A schematic diagram of an integrated on-chip optical micro-resonator based label-free optical biosensing system.

based on the integration of an electronically controlled linear swept-frequency semiconductor laser, an on-chip planar high quality factor (Q) optical resonator, and a micro-fluidic flow cell for analyte delivery. We address a number of key issues that currently prevent this technology from becoming an accessible, affordable, and useful tool.

1.2 Label-free optical biosensing

Studying the behavior of biomelecules at low concentrations, often a necessity due to their rarity, is typically accomplished using fluorescence measurements such as the enzyme-linked immunosorbent assay (ELISA) [9]. A critical disadvantage of this method is that it requires the biomolecule to have inherent fluorescence or that it or its conjugate be labeled with a fluorescent molecule. The former is uncommon and the later requires a series of reactions that can significantly alter a molecule's subsequent behavior. Additionally, many chemical species of interest are not available with fluorescent labels. Label-free technologies therefore present a tremendous advantage in probing biomolecules in their natural state or in performing specific measurements of target analyte molecules.

Many label-free optical biosensing techniques rely on monitoring changes in the properties of a sensitive optical structure as analyte molecules bind to its surface.

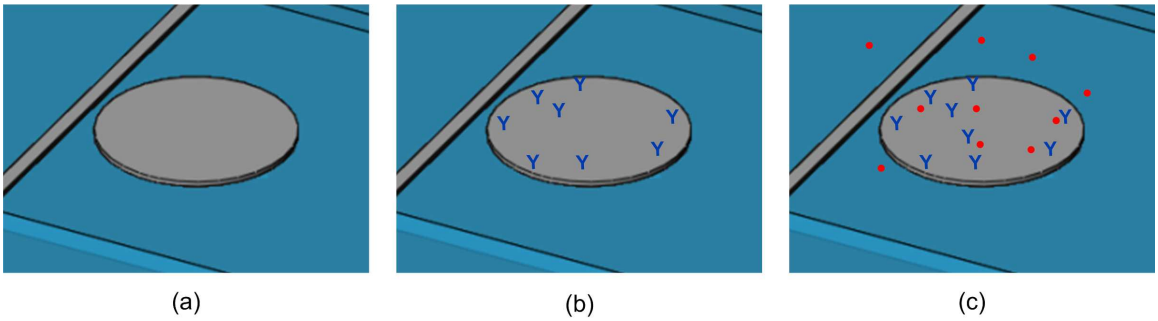

Figure 1.2: A cartoon depiction of a label-free specific sensing experiment using an integrated microdisk resonator. (a) The disk is immersed in a buffer solution. (b) The resonator surface is functionalized with an antibody by fluid flow. (c) Analyte solution containing antigen molecules is flown over the disk resulting in antibody antigen binding.

The effective refractive index of a composite dielectric structure is one such optical property that is modified by the binding of molecules. Biomolecules have a refractive index that is different, typically higher, than the refractive index of the solution they are dissolved in. Therefore molecule binding events perturb a dielectric structure's effective index. In the case of a dielectric resonator structure, index perturbations elongate the effective optical path length within the resonator and modify the resonance condition resulting in a red shift in optical frequency.

Surface plasmon resonance (SPR) [10] is one alternative label-free sensing technology that shares some of the benefits of the optical micro-resonator method and is commercially available from several companies including GE. This technology involves exciting a surface plasmon in a gold film and monitoring the changing resonance condition (wavelength or incidence angle) of the plasmon as analyte molecules such as antibodies bind to the film. SPR is highly sensitive to refractive index perturbations; however, the resonance has a particularly wide linewidth. Typical limits of detection for commercial SPR systems are > 10 pM [11].

High-Q optical resonator structures fill an important role in label-free optical biosensing providing both high sensitivity to refractive index perturbations and high resolution. Additionally, the dielectric resonator surface can be chemically functionalized with conjugate or partner molecules, e.g. an antibody, thereby restricting it

to interactions with only specific analyte species. The focus of much of the research on optical micro-resonator biosensors has been on the demonstration of extreme sensitivity down to the single molecule [12], viron [13], or nano-particle [14–16] level. However, single unit sensitivity is not necessary in many applications where analyte concentrations in the 10 fM to 100 nM regime are more prevalent. This work is directed at creating and developing a label-free refractive index-based optical biosensing system that addresses the shortcomings of contemporary systems and provides relevant sensitivity.

Optical resonator biosensing systems typically comprise three subsystems, an optical resonator and coupling scheme for signal transduction, a tunable laser for measuring resonator transmission spectra, and an analyte fluid delivery system. This work seeks to improve each of these three areas in order to develop a system that is robust, low cost, amenable to mass production, and relatively easy to use. A basic system schematic is shown in figure 1.1.

1.2.1 Optical resonator

The need for simple, sensitive, label-free, highly specific detection of biomolecules has led to increased interest in optical microresoantor sensors. Many resonator geometries have been proposed and demonstrated including microspheres [13, 15–17], microtoroids [12], photonic crystals [18], microrings [6, 19, 20], and microdisks [5, 21]. These devices can be characterized by their quality factor or, Q, which is a measure of the power lost by the resonator per optical cycle. Whispering gallery mode (WGM) type resonators, such as microspheres and microtoroids, have garnered much attention in the biosensing community and elsewhere due to their ability to achieve quality factors on the order of 10^8. Successful implementations of microspheres and microtoroids involve a fabrication step to reduce the surface roughness of the resonator. This is accomplished by either melting or polishing the surface, reducing the roughness. However, the change in size of the resonator that occurs during this complicated process demands post fabrication positioning of delicate optical components

to couple light into the resonant mode. Such positioning, and the fragile nature of these optical coupling schemes preclude on-chip integration of the resonator, coupling waveguide, and fluid delivery. These cavity geometries are therefore incongruous with the goal of developing a miniature and robust optical biosensor.

This work focuses on the development of lithographically defined high-Q resonator structures on-chip using established semiconductor processing tools and methods. Specifically, we fabricate planar microdisk resonators with integrated waveguides in a silicon nitride on silicon oxide material system. The microdisk resonators achieve high loaded quality factors enabling them to provide high resolution frequency shift measurements. Additionally, the silicon nitride material system has low absorption loss in the wavelength regime of interest, 1.3–0.7 μm, allowing for sensor operation at wavelengths where water absorption losses are also low.

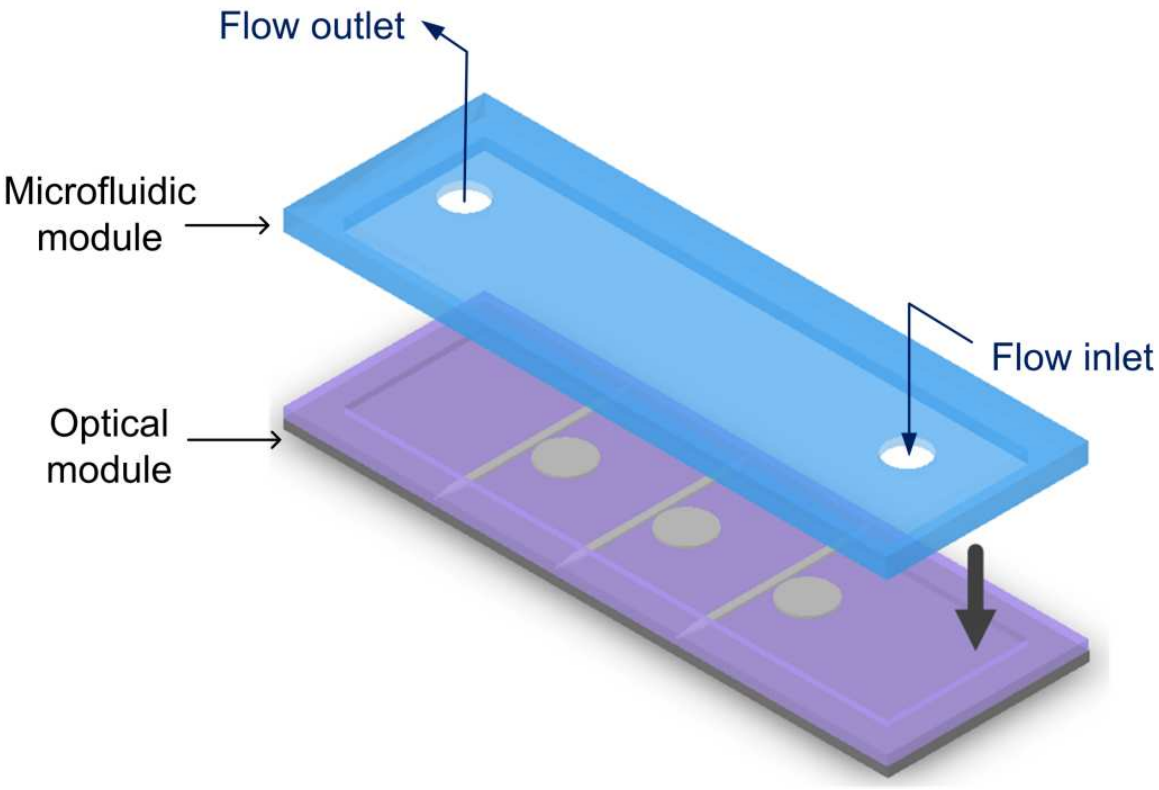

Figure 1.3: A three-dimensional rendering of the integrated silicon nitride microdisk resonator sensor with micro-fluidic channel. The depiction is not to scale.

1.2.2 Swept frequency laser source

Resonator based label-free sensing measurement requires continuous monitoring of the resonant frequency of the device as analyte molecules adsorb onto its surface. This is accomplished using a swept frequency laser to rapidly and repeatedly interrogate the transmission spectrum of the resonator. A reliable, robust, and precise laser source is therefore needed in order to enable practical use of the optical biosensing system. Current commercially available swept frequency lasers used in label-free optical biosensing systems rely on the mechanical tuning of an external cavity. These mechanically tuned lasers are beset by limitations on sweep speed and linearity and are also fragile and expensive [22, 23]. Previous work in our group has produced a novel, precisely controlled, optoelectronic swept frequency laser (SFL) based on a semiconductor laser in a feedback loop [24].

The SFL leverages several unique properties of semiconductor lasers including size, power output, reliability, narrow linewidth, and low cost to produce optical frequency sweeps with bandwidths that are capable of covering the magnitude of frequency shifts encountered in measuring dielectric resonator biosensors. The SFL has no moving parts and generates precise, repeatable, highly linear optical chirps. Additionally, the SFL system architecture can be implemented at several wavelengths of interest including 1550 nm, 1310 nm, and 1064 nm. The work presented in this thesis mostly used a 1310 nm SFL. The SFL wavelength used in experiments is noted throughout the text.

1.2.3 Sensor flow system

For an optical biosensing system to be an effective analytical or diagnostic tool, it must consume as little analtye as possible during the course of a measurement. Additionally, it should be constructed from inert biologically compatible materials. Micro-fluidic devices made from the soft polymer polydimethylsiloxane (PDMS) have become invaluable tools for these reasons [25]. We use standard photolithographic techniques to fabricate PDMS flow delivery devices. The micro-fluidic device and

optical resonator chip are treated with oxygen plasma and permanently bonded. The integrated resonator and waveguide are a natural fit with a PDMS microfluidic anaylte delivery system. Complex microfludic devices incorporating valves and recirculating pumps can also be fabricated enabling highly sensitive assays that use only minute quantities of analyte.

1.3 Organization of the thesis

The thesis has the following organizational structure. The optoelectronic swept frequency laser and some of its applications are described in Chapter 2. This includes the design of the control loop used for creating linear optical chirps as well as demonstrations of several swept frequency laser systems. Some non biosensing applications of the swept frequency laser, including experimental demonstrations are also presented.

Whispering gallery mode optical micro-resonators are described in Chapter 3. The basic concepts behind traveling wave optical resonator structures are presented. Optical resonances in disk type dielectric optical resonators are described; detailed numerical simulations of the whispering gallery modes of silicon nitride on silica microdisks are also shown. Coupling between a microdisk resonator and a single mode optical waveguide is explored using a coupled mode approach. Microdisk resonators are fabricated and measured demonstrating resonances with quality factors of 7×10^6.

Chapter 4 covers refractive index-based sensing using silicon nitride microdisk resonators. Design considerations for optical resonator sensors operating in an aqueous environment are discussed. Bulk refractive index sensing is described, simulated, and experimentally demonstrated. The results for several biosensing experiments including both nonspecific and specific adsorption of proteins are presented.

Chapter 5 discusses the challenges and sources of environmental and measurement noise associated with high-Q micro-resonator based RI sensing measurements. A solution to many of these issues, in the form of a differential measurement utilizing dual microdisk resonators, is proposed, analyzed, and experimentally demonstrated. The dual resonator approach is shown to dramatically improve the performance of

the label-free optical biosensing system.

Chapter 6 summarizes the thesis and presents the outlook for future of the project. A covalent surface functionalization scheme is described and potential improvements to the microfluidic channel structure are briefly discussed.

Chapter 2

The optoelectronic swept-frequency laser

2.1 Introduction

The semiconductor laser (SCL) has become one of the foundations of modern optical communication because of its compact size, efficiency, low cost, ease of integration with electronic circuits, and maturity of fabrication techniques. SCLs bring a unique combination of coherence, low physical volume, cost, and practicality that have enabled it to become the workhorse of fiber optic networks.

Amongst the many unique properties of SCLs, one that is less desirable in optical telecommunications is their high frequency sensitivity to both injection current and temperature. The direct modulation of SCLs for data transmission can result in optical pulses with a frequency chirp. These chirps can conspire with group velocity dispersion (GVD) in an optical fiber resulting in temporally broadened optical pulses and reduced data transmission rates. The strong frequency-temperature sensitivity often necessitates high quality packaging with internal temperature control systems for frequency stabilization.

At first blush, the frequency sensitivity of SCLs may seem entirely disadvantageous. However, these properties enable the use of a semiconductor laser diode as a current controlled oscillator (CCO). In electronics, the CCO and the voltage controlled oscillator (VCO) are critical components for feedback systems such as phase-

locked loops (PLL). The existance of an opto-electronic CCO enables the construction of optoelectronic feedback systems such as optical phaselocked loops (OPLLs) [26–28] and the optoelectronic swept frequency laser (SFL).

In this chapter we discuss the broadband frequency-current tuning response, and the frequency modulation (FM) response of the single section distributed feedback (DFB) semiconductor laser. We also report on the use of these characteristics in designing optoelectronic feedback systems to generate and control the properties of broadband linear optical frequency sweeps. The basic operating principals of the SFL are discussed and experimental demonstrations of several SFL systems are presented. Linear optical frequency sweeps, and therefore SCL based SFL systems, have applications in many fields including three-dimensional imaging, LIDAR, spectroscopy, and particularly the main subject of this thesis, label-free optical biosensing. The use of SFL systems in the applications of range resolution imaging and spectroscopy are explained and demonstrated experimentally.

2.2 Semiconductor laser frequency-current tuning

The output frequency of the SCL varies strongly with injection current from the lasing threshold to the maximum possible input current. This injection current tuning goes hand in hand with the variation in optical output power as a function of injection current. Figures 2.1a and 2.1b demonstrate the relationship of both of these parameters with input current. To investigate the tuning, the injection current into a $\lambda_0 \approx 1310$ nm DFB laser was varied from 0 mA to the manufacturer's recommended operating maximum. The optical output power was measured with an integrating power meter and the optical frequency was measured using a wavemeter.

During these experiments, the SCL was mounted in a temperature controlled mount and its temperature was maintained at 25° C throughout the measurement. Figure 2.1b represents the DC tuning characteristic of the DFB-SCL. The DC tuning

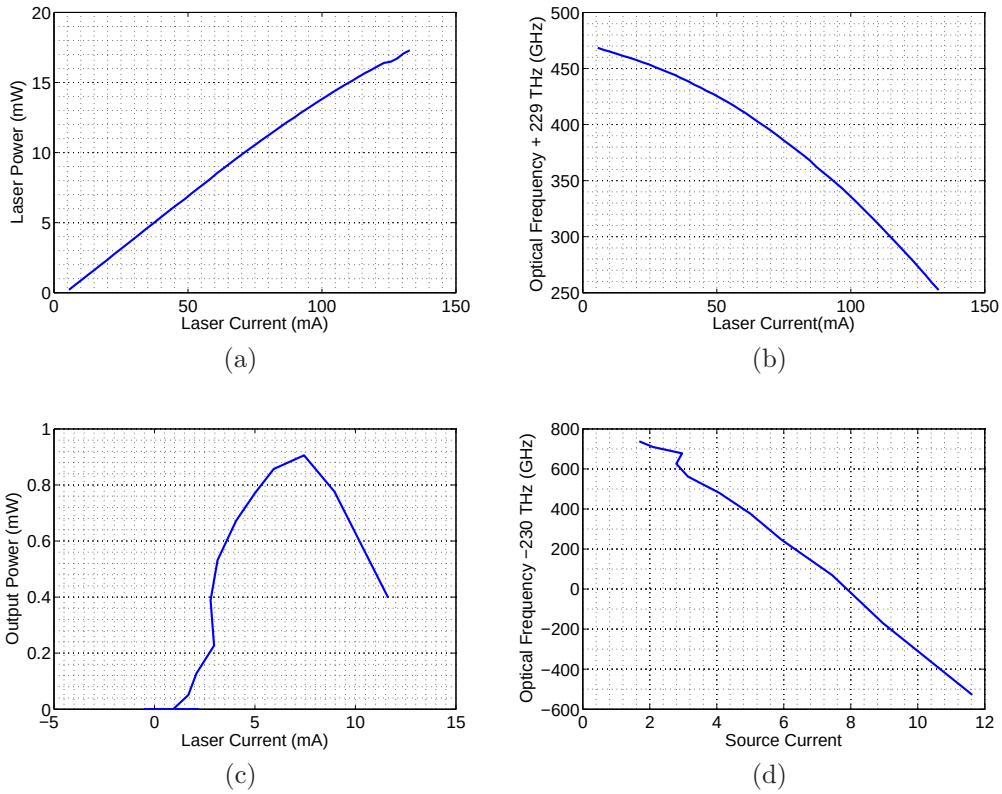

Figure 2.1: (a)The optical output power vs. input current (LI) characteristic of a $\lambda_0 \approx$ 1310 nm DFB laser. (b) The output optical frequency vs. input current characteristic of the same DFB laser as in (a). (c) The optical output power vs. input current (LI) characteristic of a $\lambda_0 \approx 1310$ nm vertical cavity surface emitting laser (VCSEL) (d) The output optical frequency vs. input current characteristic of the same VCSEL as in (c).

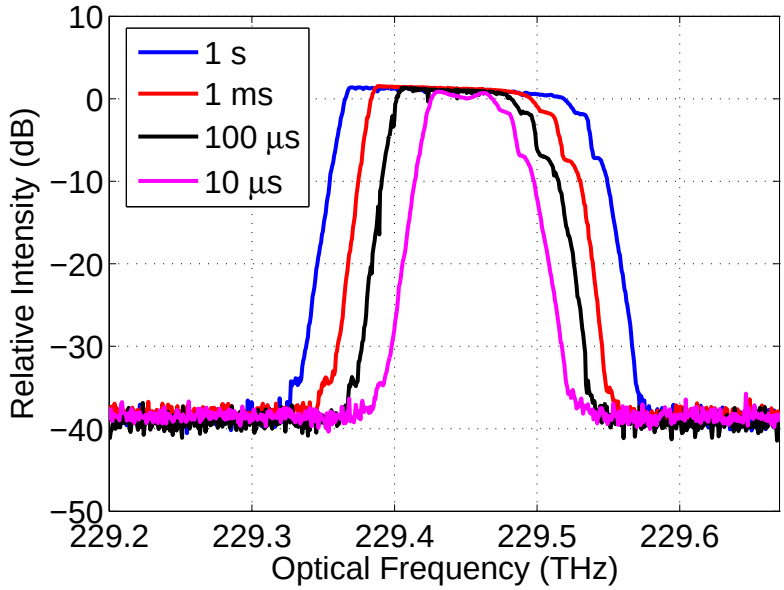

Figure 2.2: Optical spectra of a $\lambda_0 \approx 1310$ nm DFB laser with a triangle wave drive current waveform. The frequency of the drive current waveform is stepped over several orders of magnitude providing ramp durations from 1 s to 10 μs.

characteristics of vertical cavity surface emitting lasers (VCSELs) were also investigated at a variety of wavelengths including 1550 nm, 1310 nm, and 850 nm though only the results from the 1310 nm experiments are shown in Figures 2.1a through 2.1d. From Figures 2.1c and 2.1d we can see that the VCSEL is capable of single mode tuning over a much larger optical bandwidth than the DFB laser. This is attributable to the shorter cavity length of the VCSEL.

The current-frequency tuning of the laser is accompanied by a modulation in the output power of the laser. This amplitude modulation, a parasitic effect from the perspective of constructing a swept frequency laser (SFL), can be corrected with a second feedback loop incorporating either a variable optical attenuator (VOA), or a semiconductor optical amplifier (SOA).

Dynamic tuning of the SCL, as opposed to the static DC tuning shown in 2.1b and 2.1d, effects the characteristics of the generated frequency sweep or chirp. The total frequency tuning bandwidth decreases as the speed with which the ramped input current is increased. This is due to the slow nature of the thermal tuning mechanism responsible for the large signal frequency response of the SCL [29, 30]. Particularly,

it reflects the inability of the thermal response to follow rapidly varying injection currents. To measure the possible chirp bandwidth range of the 1310 nm DFB laser at several chirp rates, the modulation input of the laser driver circuit was connected to a waveform generator outputting a 2 V peak-to-peak triangle voltage waveform with a DC offset of 1 V. The corresponding current output of the laser driver was a triangle wave varying from 122 mA to 42.3 mA. The low point current was still well above the laser's threshold value. The frequency of the modulation waveform was varied between 0.5 Hz and 50 kHz in steps of factors of 10. The output of the DFB laser was put through an SOA and the optical spectrum was observed using an optical spectrum analyzer in max hold mode. The results are shown in Figure 2.2. The temperature of the laser was set to 28°C and was maintained by a temperature controller.

From Figure 2.2 we can see that the full tuning range of the laser decreases by several tens of GHz as the current ramp speed is increased. With a sweep duration of 1 s (0.5 Hz triangle wave) the 3 dB chirp bandwidth is 163 GHz. The chirp bandwidth further decreases to 119 GHz at 1 ms, 90 GHz at 100 μs, and 59 GHz at 10 μs. The relative flatness of the output optical spectra is due to the presence of the SOA which was operated in a gain saturated mode due to the relatively high output power, approximately 10 dBm, of the DFB laser itself. For the applications under consideration in this work, frequency chirp rates on the order of 10^{14} Hz/s or 100 GHz in 1 ms are adequate, though it should be noted that this laser is capable of producing sweeps as fast as 10^{15} Hz/s. Some VCSELs are capable of producing chirps up to 10^{16} Hz/s or 1 THz in 100 μs.

The SCL output frequency is also highly sensitive to its operating temperature which in many cases is maintained by a temperature controller. Adjusting the steady-state temperature setpoint of the SCL provides coarse tuning of the optical frequency. Utilizing the coarse temperature setpoint-based tuning, adjacent portions of the optical spectrum can be addressed using a single laser diode. This functionality is of particular usefulness in investigating the transmission spectra of multimode optical resonators or in spectroscopic measurements. The coarse temperature tuning of cur-

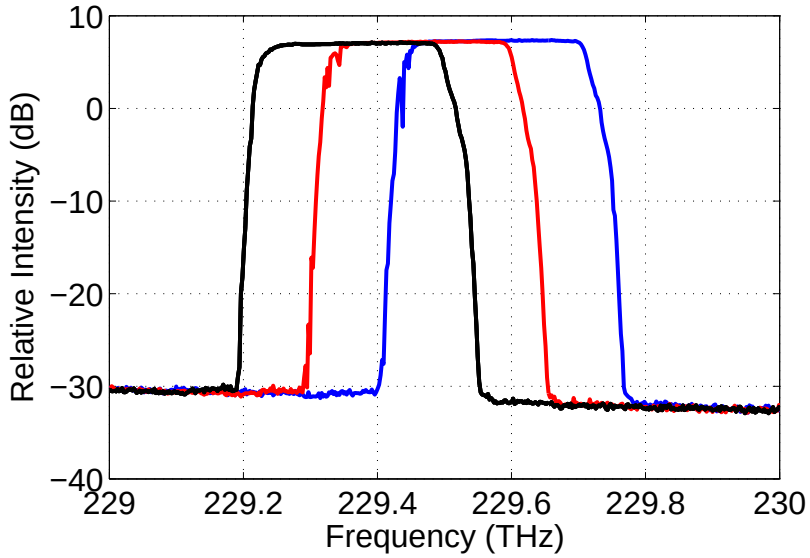

Figure 2.3: Optical spectra of a dynamically tuned 1310 nm DFB laser at three different steady state operating temperatures. The black, red, and blue traces were taken at temperatures of 34°C, 28°C, and 22°C respectively.

rent tuned laser frequency sweeps is shown in Figure 2.3. The current waveform used for dynamic tuning in this experiment was the same 1 ms duration triangle waveform input described above.

2.3 SFL system description

The frequency tuning of single section DFB lasers and VCSELs, discussed in Section 2.2, is nonlinear with injection current. This nonlinearity limits the usefulness of frequency chirps generated by SCL sources in applications of interest including range resolution imaging, spectroscopy, and label-free optical biosensing. In many cases linear optical chirps are desired because they provide a simple mapping from time to optical frequency. To linearize frequency sweeps generated by SCL sources, feedback control techniques using a fiber-based interferometer and a lock-in amplifier [31] have been proposed and demonstrated. However, that work produced optical frequency sweeps limited to 100 GHz in 10 ms, which according to Figure 2.2 is considerably slower than what a single section DFB laser should be capable of achieving.

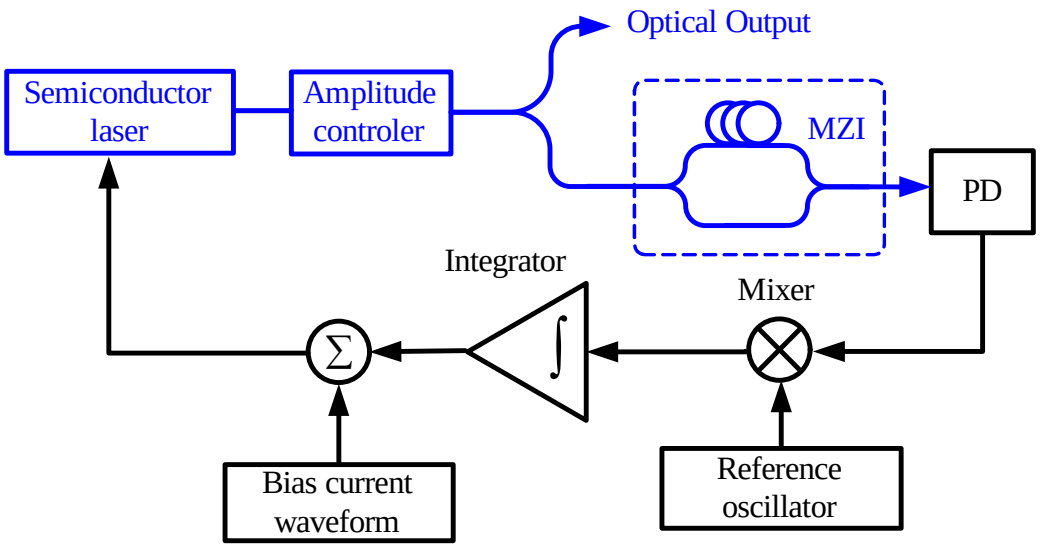

Figure 2.4: The system schematic of the optoelectronic swept frequency laser system (SFL). PD is a photodiode and MZI is a differential delay Mach-Zhender interferometer. The optical path is highlighted in blue.

Figure 2.4 illustrates the feedback system used, first reported in [24], to produce high speed precisely linear chirps from single section DFB SCLs and VCSELs. In this system, a small portion of the output light from an SCL is tapped off using a fused fiber 90/10 coupler and fed into an SOA based amplitude control loop followed by an optical fiber differential delay Mach-Zhender interferometer (MZI) and a photodiode. The MZI serves as a frequency discriminator [32], converting frequency modulation at the input into amplitude modulation. The fiber MZI is stabilized from mechanical vibrations by careful packaging in an enclosure. The photodiode produces an electrical signal which is mixed with a reference sinusoid from a high quality monochromatic electronic oscillator. The resulting error signal is integrated, summed with the large signal bias current waveform (nominally a linear ramp) and fed back into the SCL current driver. The laser drive current is limited in its allowed range and must be ramped and then reset to sweep again thereby producing optical chirps of relatively short duration. The feedback loop operates in a gated fashion. Therefore, the loop must acquire the locked state at the initiation of each sweep. By contrast, in recent work on and development of these swept frequency laser sources, the laser is driven in a manner more akin to a triangle wave, resulting in linear optical frequency chirps

both up and down [33]. This mode of operation is both necessary and desirable in certain applications such as the suppression of stimulated brillouin scattering (SBS) in high power fiber amplifiers [33, 34].

2.3.1 Steady state analysis

To understand how the feedback system shown in Figure 2.4 produces precisely linear frequency sweeps, we first look at the feedback loop from the perspective of a steady state analysis. Assume that the laser is generating a linearly varying frequency output $\omega(t)$ that can be described by

$$\omega(t) = \omega_0 + \xi t, \tag{2.1}$$

where ω_0 is the starting frequency of the sweep and ξ is its slope. This corresponds to a time varying optical phase $\phi(t)$ given by the integral of equation 2.1, namely

$$\phi(t) = \frac{1}{2}\xi t^2 + \omega_0 t + \phi_0. \tag{2.2}$$

The intensity of the output of the MZI consists of both time varying and DC terms (which we will ignore). The non-DC terms are proportional to

$$I_{MZI} \propto cos\left(\phi(t) - \phi(t-\tau)\right), \tag{2.3}$$

where τ is the differential delay of the interferometer. Substituting 2.2 into 2.3, we arrive at an expression for the photocurrent i_{PD} given by

$$i_{PD}(t) = K_{PD} cos\left(\xi\tau t + \omega_0\tau - \frac{\xi\tau^2}{2}\right) \tag{2.4}$$

where K_{PD} is the gain of the photodiode. From Equation 2.4 we can begin to see the function of the MZI. The photodiode signal oscillates at a frequency proportional to both the interferometer delay and the slope of the optical chirp. Additionally, the starting phase of this signal (a gated sinusoid) contains information about the

starting frequency of the chirp.

$$\omega_{PD} = \xi\tau, \phi_{PD} = \omega_0\tau - \frac{\xi\tau^2}{2} \tag{2.5}$$

Mixing the photocurrent with a high quality electronic oscillator results in both a sum and difference term. We will ignore the sum frequency term, as it will be filtered out by the loop, and focus on the difference term given by

$$i_{mix}(t) = K_{PD}K_{mix}cos\left(\xi\tau t + \omega_0\tau - \frac{\xi\tau^2}{2} - \omega_{Ref}t - \phi_{Ref}\right). \tag{2.6}$$

With an appropriate choice for the electronic reference oscillator frequency ω_{Ref}, namely

$$\omega_{Ref} = \omega_{PD} = \xi\tau, \tag{2.7}$$

the mixer difference signal becomes

$$i_{mix}(t) = K_{PD}K_{mix}cos\left(\omega_0\tau - \frac{\xi\tau^2}{2} - \phi_{Ref}\right) \tag{2.8}$$

This DC signal is then integrated producing a linear current ramp which when added to the open loop bias current waveform is fed back into the laser once again yielding the linear frequency sweep of Equation 2.1. We have therefore arrived at a self consistent steady state solution for the SFL.

It is important to recognize that the actual steady state criteria imposed by the feedback loop is

$$\frac{di_{mix}}{dt} = \frac{d}{dt}\left(K_{mix}K_{PD}cos\left(\phi(t) - \phi(t-\tau) - (\omega_{Ref}t + \phi_{Ref})\right)\right) = 0. \tag{2.9}$$

In the approximation that $\phi(t) - \phi(t-\tau)$ is small, Equation 2.9 becomes

$$\frac{d}{dt}\left(\phi(t) - \phi(t-\tau) - \phi_{Ref}\right) = \omega_{Ref}. \tag{2.10}$$

If we further assume that τ itself is small enough to use only the first order terms

from a Taylor expansion, the steady state condition can be reduced to

$$\begin{aligned} \frac{d^2\phi\left(t\right)}{dt^2}\tau &= \omega_{Ref}, \\ \frac{d\omega\left(t\right)}{dt}\tau &= \omega_{Ref}, \end{aligned} \tag{2.11}$$

which has solutions in the form of a linear frequency vs. time (ω vs.t) dependence.

The slope of the frequency sweeps and the starting frequency of each sweep, in locked steady state operation are therefore given by

$$\xi = \frac{\omega_{Ref}}{\tau}, \omega_0 = \frac{\phi_{Ref} + 2\pi m}{\tau}. \tag{2.12}$$

We note that the steady state solution of the feedback system is actually a family of linearly varying frequency sweeps where the sweep speed is locked to the frequency of an electronic oscillator, and the allowed starting frequencies of the sweeps are separated by the free spectral range (FSR) of the MZI used in the feedback loop. The FSR is given by $1/\tau$. The actual solution, and therefore the absolute starting frequency of the sweep, will depend on both the bias current and temperature set point of the SCL. This feature of the SFL is of extreme importance in the applications of spectroscopy and optical biosensing.

The validity of the approximations made in this analysis rely on the free running nonlinearity of the frequency sweep (that produced by the open loop bias current waveform) to be small and the loop gain to be high. Both of these conditions can be met and are discussed in Section 2.3.3.

2.3.2 Small signal analysis

Further understanding of the operation of the optoelectronic swept frequency laser can be gained by performing a small signal analysis of the feedback loop in the frequency domain.

Assuming the steady state operating point derived in the previous section, the propagation of phase fluctuations in the feedback loop of Figure 2.4 can be represented

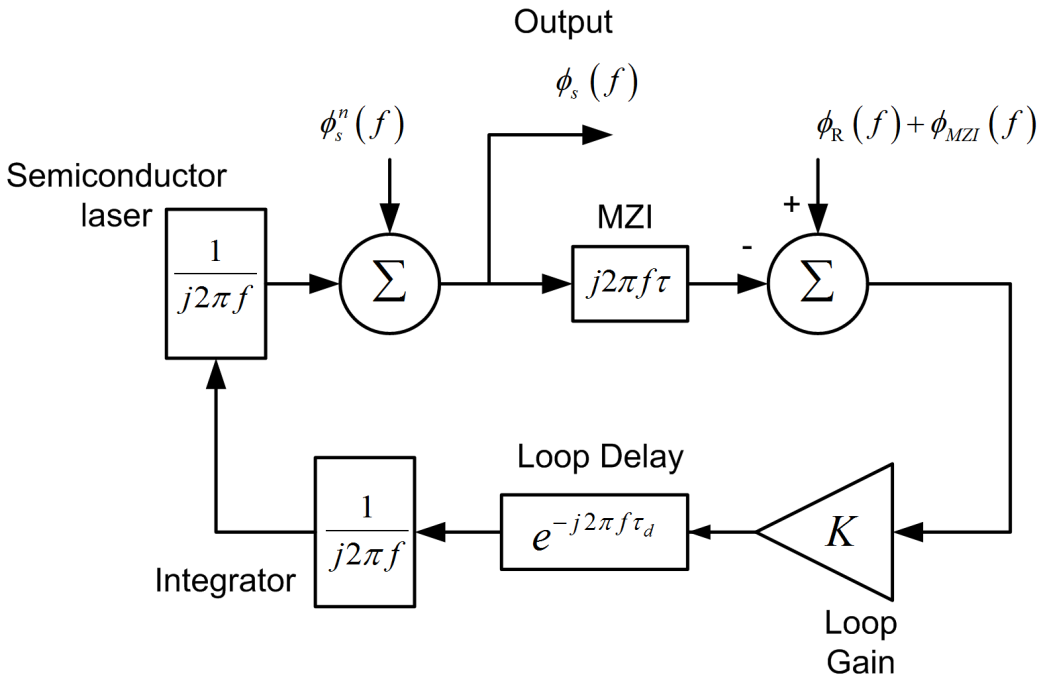

Figure 2.5: The small signal model for the optoelectronic swept frequency laser system (SFL). MZI is a differential delay Mach-Zhender interferometer.

by the small signal model shown in Figure 2.5. In this model, the laser acts as a current controlled oscillator whose output phase is proportional to the integral of the input current modulation. The true FM response of an SCL is non-uniform and rather complicated [29]. However for our purposes, it is sufficient to use a simple integrator model. The phase noise of the laser and its deviations from the steady state solution (sweep nonlinearity) are encompassed in the variable $\phi_s^n(f)$. The MZI is modeled as an ideal frequency discriminator which is valid in the regime in which the small signal frequency fluctuations are much less than the FSR of the interferometer. The phase noise of the RF source and the interferometer noise are accounted for by $\phi_R(f)$ and $\phi_{MZI}(f)$ respectively. The DC loop gain K lumps together the photodetector, mixer, integrator, and laser gains. The effect of the finite loop delay τ_d is given by $e^{-j2\pi f\tau_d}$. The integrator is assumed to be ideal.

To gain an understanding of how the feedback loop effects the output phase $\phi_s(f)$ we can write the propagation of the phase noise in the loop as

$$\phi_s(f) = \left(-\phi_s(f)\, j2\pi f\tau + \left(\phi_R(f) + \phi_{MZI}(f)\right)\right) K e^{-j2\pi f\tau_d} \left(\frac{1}{j2\pi f}\right)^2 + \phi_s^n(f). \tag{2.13}$$

Rearranging terms we obtain

$$\begin{aligned}\phi_s(f) = {} & \phi_s^n(f) \left(\frac{j2\pi f}{j2\pi f + \tau K e^{-j2\pi f\tau_d}}\right) \\ & + \left(\phi_R(f) + \phi_{MZI}(f)\right) \left(\frac{K e^{-j2\pi f\tau_d}}{j2\pi f\left(j2\pi f + \tau K e^{-j2\pi f\tau_d}\right)}\right).\end{aligned} \tag{2.14}$$

From the first term of Equation 2.14 we can see that the loop seeks to minimize the laser phase noise and sweep nonlinearity term $\phi_s^n(f)$ within the delay limited loop bandwidth. We therefore expect the loop not only to ensure the generation of linear frequency chirps but also to enhance the coherence of the laser within the loop bandwidth. The other sources of loop error contained in the second term of Equation 2.14, are dependent on the stability of the MZI and the electronic oscillator. In practice the phase noise of the electronic oscillator is negligible and can be ignored. However, special care must be taken in the construction and packaging of the fiber interferometer to ensure its stability.

2.3.3 Open-loop laser bias current waveform

Throughout the prior discussion on operation of the optoelectronic swept frequency laser it has been assumed that a nominally linear open loop frequency sweep could be achieved by the laser if it were driven by an appropriate bias current waveform. In fact, for the small signal analysis of the previous section to hold, and more generally for the feedback loop to acquire lock, this must be the case. In other words, for the system to perform as intended, deviations of the laser frequency sweep from linearity must indeed be of a small signal nature. Unfortunately, as the characterization of both the DC and dynamic tuning of a single section SCL in Section 2.2 demonstrated, a linear injection current vs. time waveform does not generate such a nominally linear

frequency vs. time optical output. Here, we present an empirical method for the determination of an open loop bias current waveform that produces a suitably linear output chirp to be further improved by the feedback system.

Continuing with the assumption that the single section SCL can be modeled as a CCO, we can construct a simple model of the laser output frequency as a function of the injection current expressing it as

$$\omega(t) = \omega_0 + K(i)\, i(t), \tag{2.15}$$

where $K(i)$ is the current dependent gain of semiconductor laser and $i(t)$ is the injection current. ω_0 is the nominal output frequency of the laser.

Our previous small signal analysis of the feedback system used the MZI as a frequency discriminator to determine sweep nonlinearity and to provide a small signal correction to the laser. It is also possible to use the MZI to measure the open loop sweep nonlinearity and determine an appropriate open loop bias current waveform to generate a more linear sweep. Using the model for the SCL in Equation 2.15, the frequency of the photocurrent at the output of the MZI is given by

$$\begin{aligned} \omega_{PD}(t) &= \tau \frac{d\omega}{dt} \\ &= \tau \frac{di}{dt} \times \left(K_{DC} + i(t) \frac{dK}{di} \right). \end{aligned} \tag{2.16}$$

We can then define a nonlinear distortion function $F_{dist}(i)$ that is a function of the current such that

$$\omega_{PD} \equiv \frac{di}{dt} \times F_{dist}(i). \tag{2.17}$$

By using a linearly varying injection current, and therefore a known di/dt, and measuring the resultant MZI photocurrent frequency ω_{PD}, we can calculate the nonlinear sweep characteristic of the laser $F_{dist}(i)$. It is then possible to use this nonlinear response measurement and the desired frequency output profile, in the case of a linear sweep $\omega_{PD} =$ constant, to solve the differential Equation 2.17 for the appropriate nonlinear injection current waveform. Iterating this procedure provides an improvement

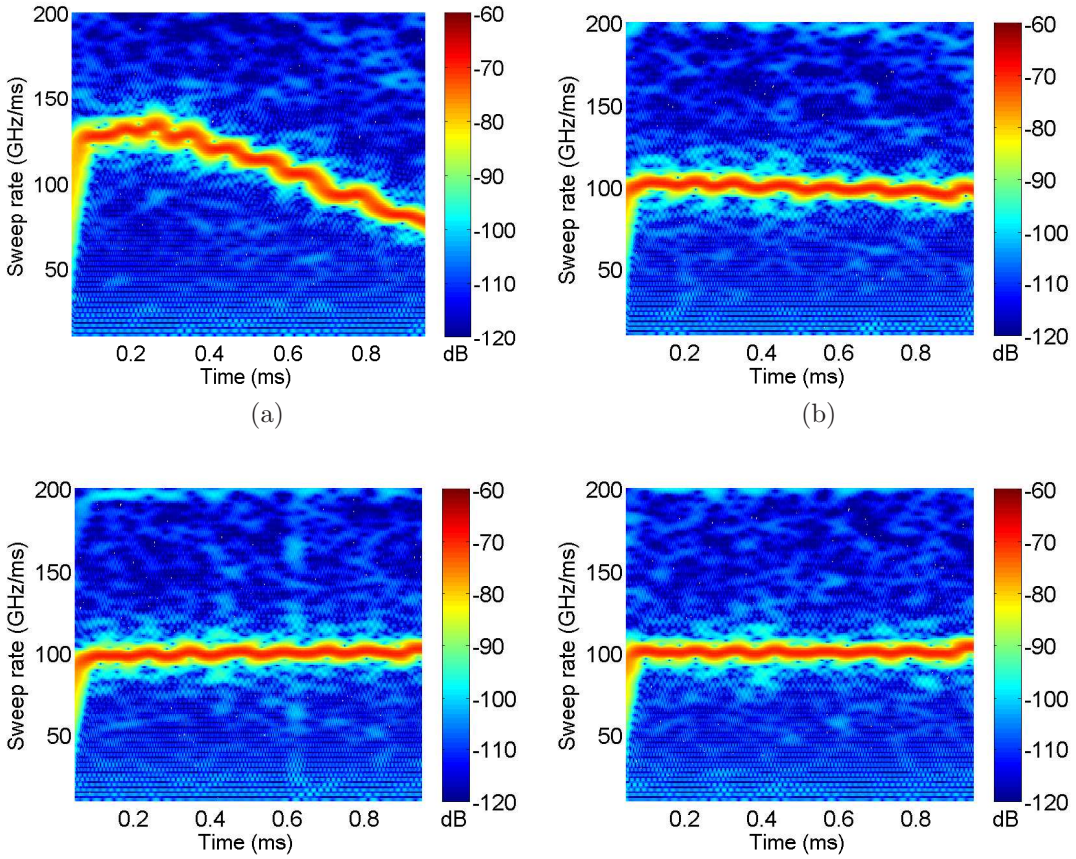

Figure 2.6: (a) Spectrogram of the post MZI photodetector current of a 1310 nm DFB laser with a linearly varying injection current waveform. (b) The spectrogram of the same laser after one predistortion, (c) after two predistortions, (d) after three predistortions.

in the resultant open loop sweep.

To characterize the linearity of the sweep generated by the SCL and the improvements to the sweep linearity made by the open loop bias current correction and feedback system, we utilize a spectrogram of the photodiode current. The spectrogram depicts the evolution of the Fourier spectrum of the photocurrent over the duration of the sweep. A linear frequency sweep would be represented as a flat line (i.e. constant slope) and a quadratic sweep by a line with a constant slope. Figures 2.6a, 2.6b, 2.6c, and 2.6d demonstrate the improvements to the linearity of the generated optical chirps as a result of the open loop correction as well as the benefit of iterating the procedure.

The response to a linear current ramp of the particular laser diode measured in the experiment shown in Figure 2.6a contains both short range nonlinearity (the chirp slope oscillates around a mean value) and long range nonlinearity. The open loop predistortion is able to remove much of the long range nonlinearity sweep within two iterations (Figure 2.6c). The short range nonlinearity persists even after further iterations (Figure 2.6d) and must be corrected by the feedback loop. It is rather interesting that a simple phenomenological model of the laser frequency-current tuning response such as Equation 2.15 is able to provide helpful corrections to the open loop large signal response of the laser. Even more interesting is the convergence of the open loop tuning characteristic to linearity after several iterations. This topic certainly warrants further study. It is important to note that the current-frequency tuning characteristic of the single section DFB SCL is dependent on its operating temperature, and changes as the laser ages. The open loop bias current predistortion procedure must therefore be performed often, typically at start-up of the SFL system, to achieve best results.

2.4 Experimental demonstration

Experimental demonstrations of the full optoelectronic swept frequency laser system shown in Figure 2.4 were performed with a large variety of SCLs in several wavelength

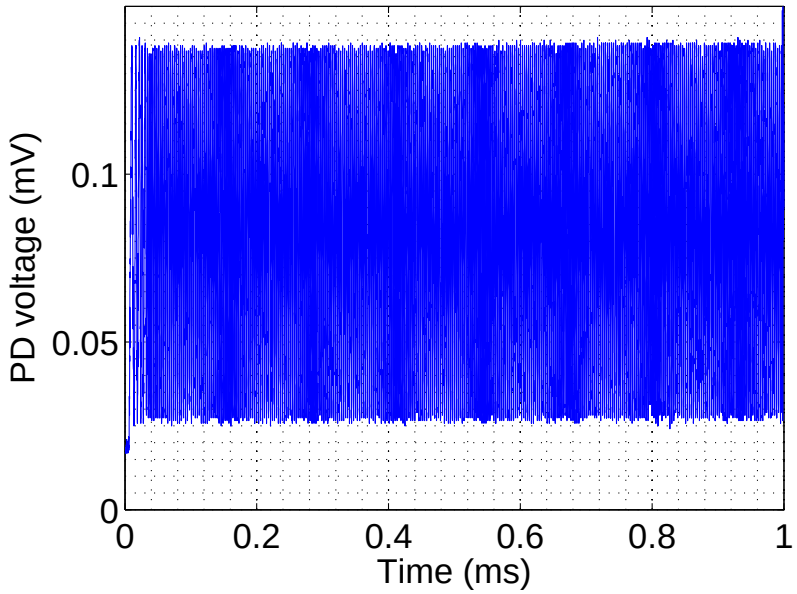

Figure 2.7: The time domain photodiode output of the optoelectronic swept frequency laser operating in the closed loop locked condition. The laser was a $\lambda_0 = 1310$ nm DFB SCL.

regimes including DFB at 1539 nm (Fitel), VCSEL at 1550 nm (Raycan), DFB at 1310 nm (Archcom), VCSEL at 1310 nm (Raycan), and DFB at 1064 nm (QDLaser). In the following section we present the details of the experimental demonstrations for selected SFL systems.

Figure 2.7 shows the output signal of the photodiode from the feedback loop of Figure 2.4. Recall that the feedback loop operates in a gated fashion and is reset at the end of each sweep. Figure 2.7 therefore shows the photodiode output signal from one representative sweep, that had a duration of 1 ms. The MZI differential delay in this experiment was 3.3 ns corresponding to a FSR of 300 MHz and a physical fiber length of approximately 67 cm. To determine the average sweep rate of the chirp from Figure 2.7 we take the Fourier transform of this signal. The main lobe of the spectrum shown in Figure 2.8a is at a frequency of 333 kHz. Given the known interferometer delay τ_{MZI}, this value corresponds to to a sweep rate of $\xi = 10^{14}$ Hz/s as desired. The linearity of the feedback locked chirp is also transform limited. The 3 dB spectral width of the peak in Figure 2.8a is 1 kHz corresponding to the transform

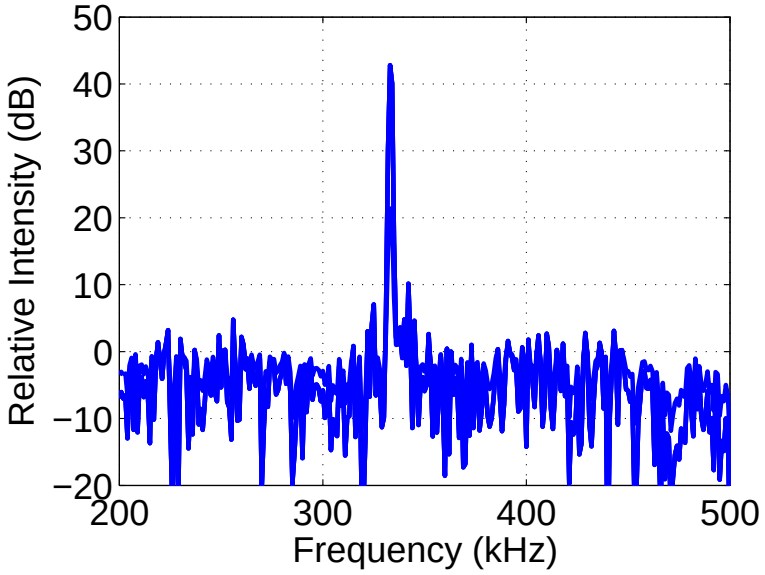

(a)

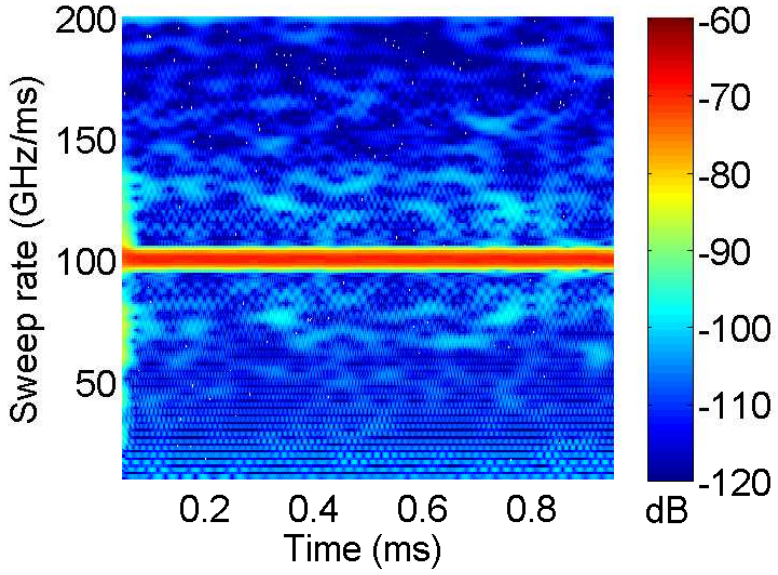

(b)

Figure 2.8: (a) The Fourier transform (computed by FFT) of the locked SFL photodiode output shown in Figure 2.7, (b) A spectrogram of the same signal as in (a).

limit of a 1 ms duration signal.

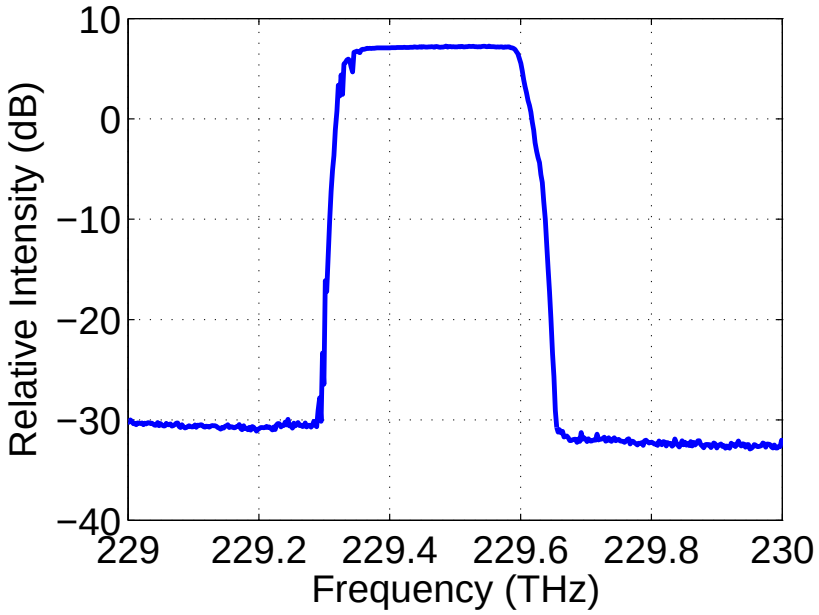

Figure 2.9: The optical spectrum of a linear frequency sweep as generated by the optoelectronic swept frequency laser with a total frequency excursion of 100 GHz. The nominal wavelength is 1310 nm.

With knowledge of both the duration and sweep rate of the generated optical chirp, we can calculate the total optical frequency excursion. In the example we have been following thus far, a 1 ms sweep at a rate of $\xi = 10^{14}$ Hz/s results in a total optical frequency excursion of 100 GHz or a total wavelength excursion of approximately 0.6 nm with a nominal wavelength of 1307 nm. We also used an optical spectrum analyzer (OSA) to observe directly the wavelength/frequency range of the optical output. The full breadth of the optical spectrum of the 1310 nm SFL is shown in Figure 2.9. The optical spectrum of the SFL shown here includes not only the light from the sweep that is controlled by the feedback system, i.e. the linear well behaved portion, but also the portion of the optical output of the system when the feedback loop and drive current are reset in between chirps. This unstructured light output is not used in any practical measurements involving the SFL but is present in the OSA measurement at hand, resulting in a broader looking optical spectrum than would be expected.

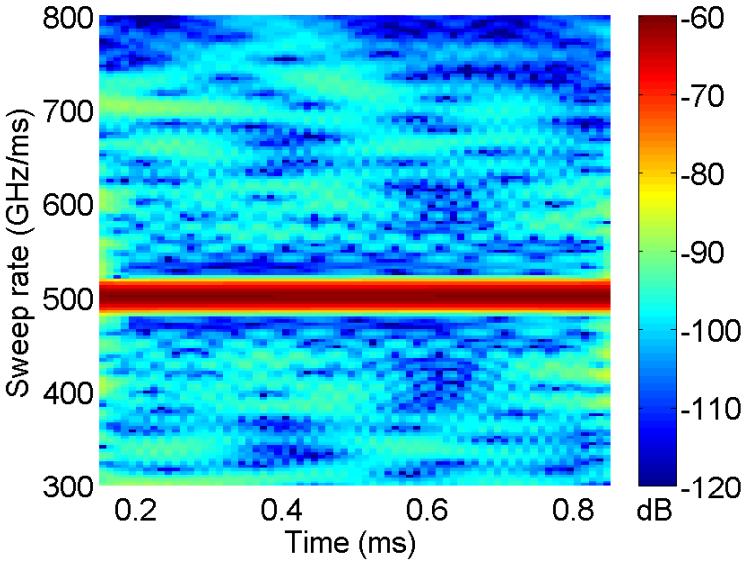

(a)

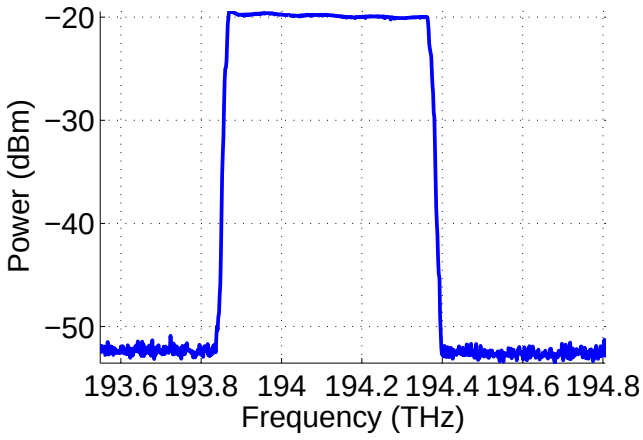

(b)

Figure 2.10: (a) A spectrogram of the locked 1550 nm VCSEL SFL output. (b) The optical spectrum of the locked 1550 nm VCSEL SFL output.

A nearly identical SFL system using a VCSEL at 1550 nm was also built. Typically, due to the small size of the laser cavity, VCSELs have much lower threshold and operating currents than DFB lasers. Accordingly, they generally produce much lower optical output power. The design of the VCSEL based SFL required alterations to the laser current driver (to source nearly 10x less current) and the use of an SOA based amplitude control loop to boost the overall output signal (a previously built 1539 nm DFB based SCL used a variable optical attenuator-based amplitude control loop).

The VCSEL cavity also has a much larger current tuning response characteristic than that of the DFB laser, as demonstrated in Figure 2.1d. VCSEL based SFLs are therefore able to produce optical frequency sweeps of a much larger bandwidth than DFB laser based SFLs. Unfortunately, VCSELs tend to have poorer optical coherence characteristics than those of DFB lasers, with linewidths typically on the order of 50 MHz to 100 MHz as opposed to 1 MHz for DFBs. Both the coherence of the laser source and the total sweep bandwidth of the SFL are important parameters in determining the appropriate MZI delay τ to use in constructing the feedback loop. The proper delay should be long enough to help suppress chirp nonlinearity but also be shorter than the coherence time of the laser source to avoid noise in the photocurrent i_{pd} due to incoherence of the light in the signal and reference arms of the MZI. Additionally, the choice of τ_{MZI}, along with the desired sweep rate ξ of the SFL, determine the locking frequency of the loop ω_{PD}. This frequency must be chosen carefully to be within the bandwith of the feedback loop and all of its components including mixers, filters, electronic reference oscillators, and summing amplifiers. In the case of the 1550 nm VCSEL SFL, we employed a fiber based MZI with a delay of approximately 0.29 ns corresponding to a FSR of 3.4 GHz or length of nearly 20 cm in SMF-28 fiber. The 1550 nm VCSEL SFL produced chirps with an optical bandwidth of approximately 500 GHz with a duration of either 1 ms or 100 μs corresponding to chirp rates of $\xi = 5 \times 10^{14}$ Hz/s and 5×10^{15} Hz/s respectively. The spectrogram of one such optical chirp is shown in Figure 2.10a. The optical spectrum of the chirp as measured with an OSA is shown in Figure 2.10b.

The 1064 nm DFB based SFL was designed as a replacement for the 1310 nm SFL in optical biosensing measurements to further reduce optical absorption loses due to the aqueous sensing environment encountered in those experiments (this is discussed in Chapter 4). This SFL system is capable of producing chirps of up to 200 GHz in 100 μs and has a CW linewidth of approximately 2 MHz. It utilizes an MZI with a delay τ_{MZI} of 5 ns corresponding to an FSR of 200 MHz or a fiber delay of nearly 1 m. The optical spectrum of the 1064 nm DFB SFL is shown in Figure 2.11

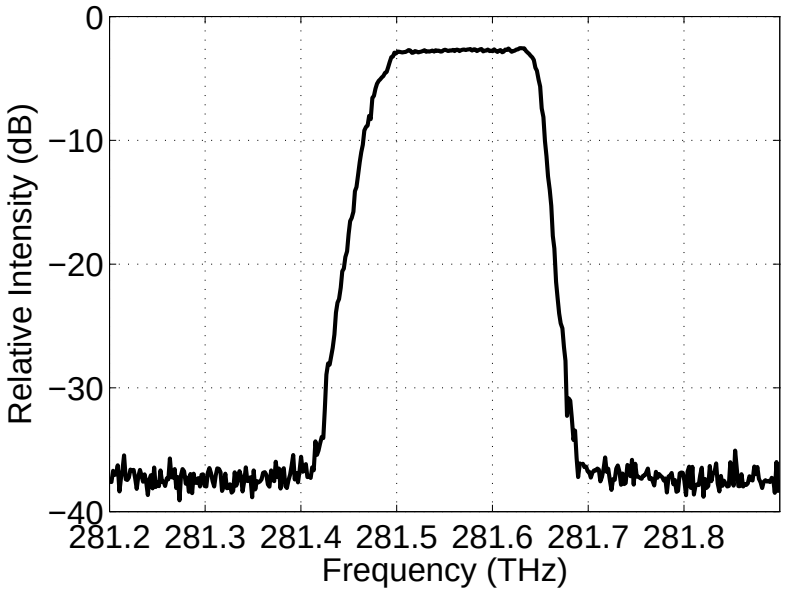

Figure 2.11: The optical spectrum of the output of the 1064 nm DFB swept frequency laser. The sweep rate of the chirp was 1.05×10^{15} Hz/s. The duration was 128 μs.

2.5 Applications of the SFL

A precisely linear optical frequency sweep is a powerful tool that has many scientific applications including imaging, sensing, and spectroscopy. Here, we present some motivation for the use of linear optical chirps in two applications: (1) the range resolution imaging technique of frequency modulated continuous wave laser reflectometry (FMCW), and (2) chemical spectroscopy. Label-free optical biosensing is discussed in subsequent chapters.

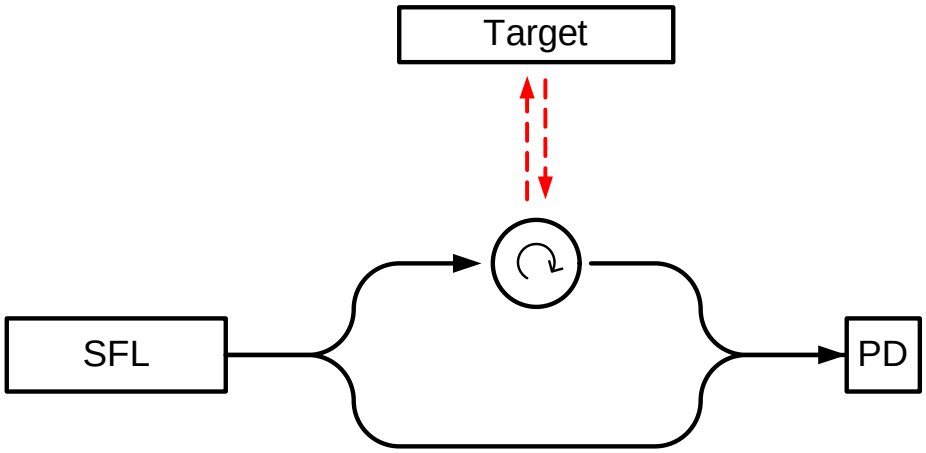

Figure 2.12: A schematic diagram of a basic FMCW laser reflectometry experiment. SFL is an optoelectronic swept frequency laser producing a linear chirp, PD photodiode. The red dashed lines denote free space optical waves to and from the target.

2.5.1 SFL range resolution imaging

FMCW laser reflectometry is a method for rapidly measuring the distance to a target using coherent linearly chirped waves [35]. This technique is based on splitting a linearly chirped coherent optical source into two beams, one of which is reflected off of a target object and the other of which is set aside as a reference. The reflected light is, upon collection, interfered with the reference beam at a photodetector. The delay in the reference arm can be set such that the differential delay between the two arms is within the coherence length of the laser source. A schematic of the basic experiment is shown in Figure 2.12. Our previous analysis showed that the differential delay between the paths of the two arms of the interferometer manifests as a sinusoidal beat signal at the photodetector. The frequency of the beat note is proportional to the chirp rate of the optical wave used in the measurement and to the delay in the interferometer. Therefore distance to a target can be determined by simply taking the FFT of the beat signal. This imaging technique can be used with targets consisting of single, or multiple reflectors and when scanned over an object or scene a full three dimensional image can be constructed.

The axial resolution of any such three-dimensional image, or more generally speaking of any FMCW measurement, is a function of the chirp bandwidth or the total

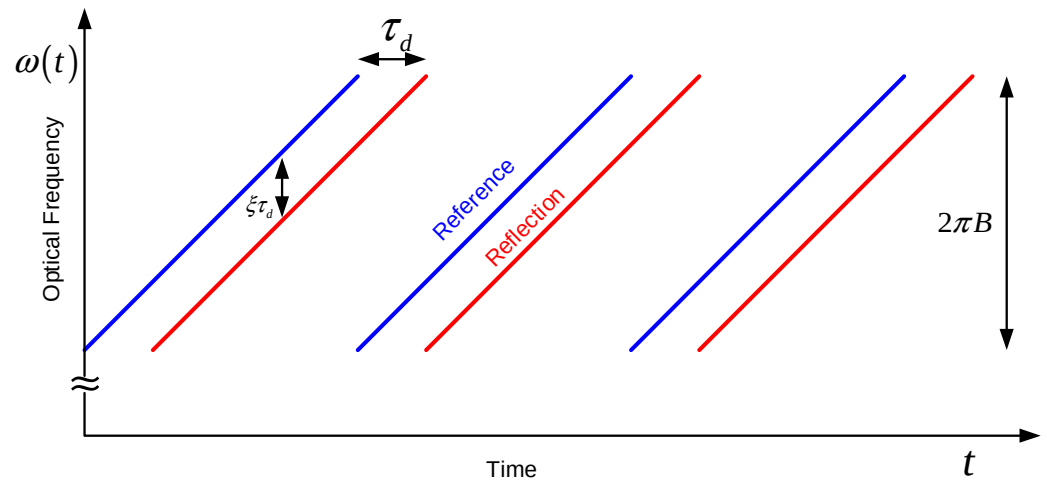

Figure 2.13: An illustration of the FMCW range resolution experiment. ξ is the chirp rate and τ_d is the delay due to the propagation distance to the target. B is the optical bandwidth of the chirp.

optical frequency excursion given by

$$\delta z = \frac{c}{2B}, \tag{2.18}$$

where c is the speed of light and B is the chirp bandwidth [36]. From Equation 2.18 we surmise that in order to discern closely spaced axial targets, large bandwidth optical chirps are needed. More precisely, given the two SFL sources we have previously described (100 GHz chirps at 1310 nm and 500 GHz chirps at 1550 nm) we have range resolutions of approximately 1 mm and 200 μm respectively, depending on the refractive index of the material being measured.

In order to demonstrate the use of an SFL source in making FMCW measurements, we performed the basic FMCW experiment shown in Figure 2.12 to image the front and back interfaces of both a microscope slide, with a nominal thickness of 1 mm, and microscope cover slip, with a nominal thickness of 120 μm. The SFL used was a VCSEL-based 1550 nm source, chirping 528 GHz in 1024 μs corresponding to a sweep rate of 5.12×10^{14} Hz/s. The results are shown in Figures 2.14a and 2.14b. In Figure 2.14a the two faces of the microscope slide are clearly visible as the distance between them is considerably greater than the axial resolution of the SFL source used

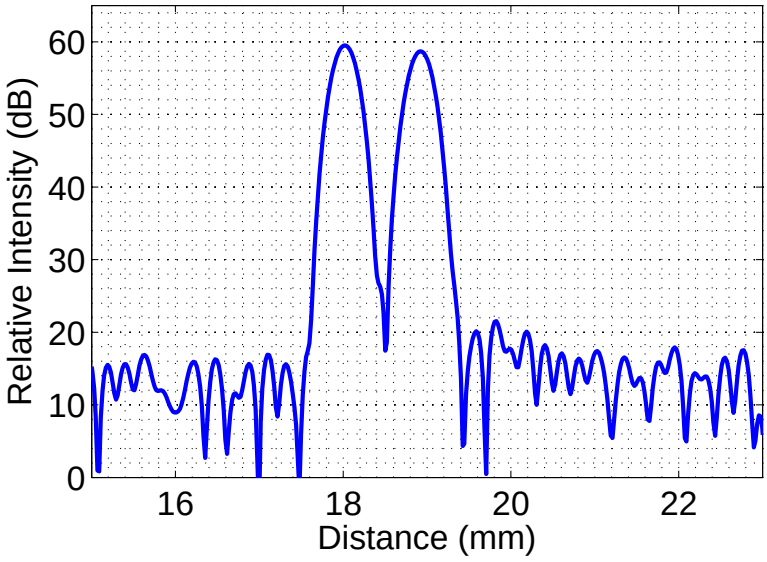

(a)

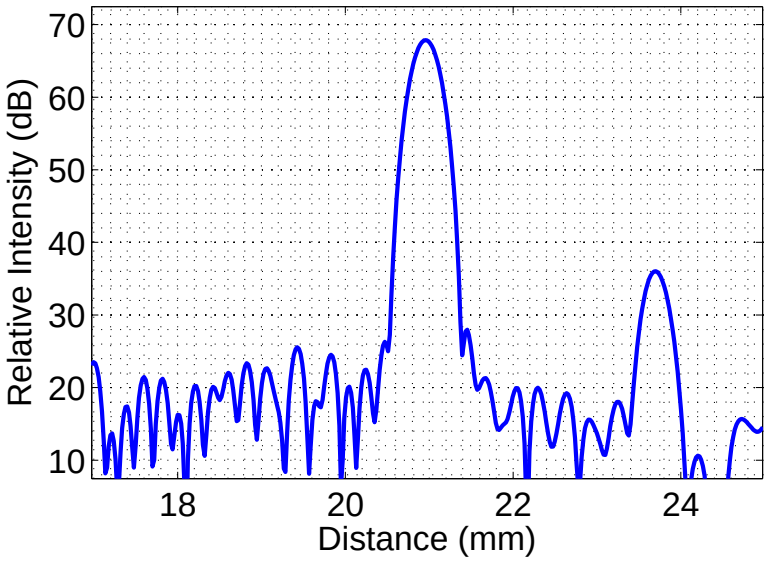

(b)

Figure 2.14: Results from an FMCW experiment performed using a VCSEL based SFL with a nominal wavelength of 1550 nm and a bandwidth of 528 GHz. (a) Shows distance to the front and back interfaces of a glass microscope slide with a nominal thickness of 1 mm, (b) shows the distance to interfaces of a glass microscope cover slip with a nominal thickness of 120 μm.

as determined by Equation 2.18. The thickness of the slide as measured with the FMCW technique is 0.9 mm. By contrast, only one peak is visible for the coverslip. The two interfaces of the coverslip are not visible because their separation is less than the axial resolution of the SFL source.

FMCW imaging of biological samples, also known as swept source optical coherence tomography (SS-OCT) [37] or optical frequency domain imaging (OFDI) [38] requires very high range resolution in order to distinguish various tissue layers and cells within a sample. Given that the desired axial resolution in this case is on the order of 10 to 15 μm, the required chirp bandwidth of an SFL source to achieve this is on the order of 5 to 10 THz. This is beyond the ability of a single SCL based SFL source. Techniques to increase the effective bandwidth of SFL sources have been investigated including multiple source FMCW imaging [39] and chirp multiplication by four wave mixing in a nonlinear medium [40]. The enhancement of chirp bandwidths via nonlinear processes is discussed in Appendix A.

2.5.2 Spectroscopy

The optoelectronic swept frequency laser source provides linear frequency sweeps of both a known duration in time and a precise sweep rate. It is therefore possible to use the SFL directly to characterize spectral features such as absorption lines and resonances that fall within the optical bandwidth of the source. This is in contrast to other laser based optical spectroscopy techniques such as amplitude-modulation (AM) and frequency-modulation (FM) [41] optical spectroscopy where an external amplitude or phase modulator is used to generate and sweep an optical sideband over a resonance, and the in-phase and in-quadrature components of the detected signal are measured using a lock-in amplifier or IQ demodulation technique. It should be noted that it is also possible to employ the SFL in an optical FM spectroscopy system where the laser's linear frequency sweep is used to change the frequency offset of the FM sideband as opposed to the sweeping of the electronic modulation frequency.

As a proof of concept experiment, a DFB based SFL operating with a nominal

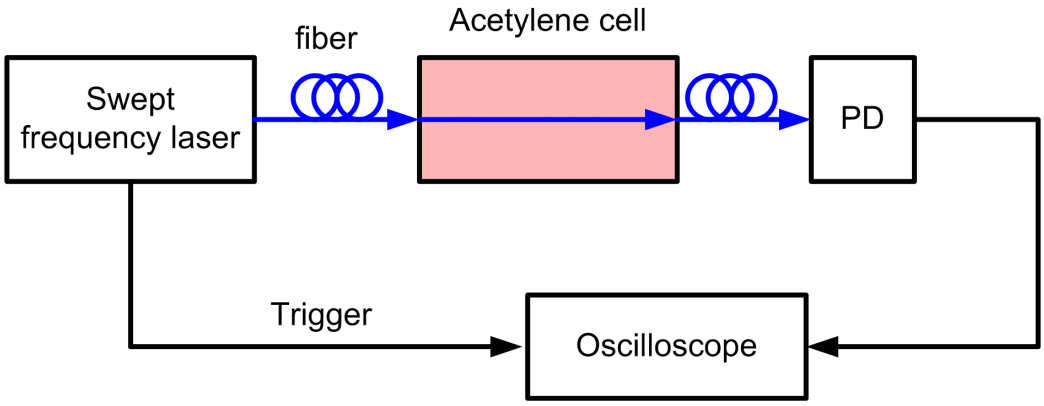

Figure 2.15: A schematic drawing of an absorption spectroscopy experiment employing the SFL. The optical path is shown in blue.

wavelength of 1539 nm was used to interrogate a portion of the absorption spectrum of a fiber-coupled acetylene gas cell. A schematic of this simple experiment is shown in Figure 2.15. The available optical chirp bandwidth from the DFB based SFL is only 100 GHz. However due to the many absorption features of acetylene in the telecom C band, it was possible to observe three acetylene vibrational resonance modes within the bandwidth of a single chirp. The experimentally measured absorption spectrum is shown in Figure 2.16a.

In order to corroborate the absorption spectrum obtained by the SFL, it was also measured with a conventional external cavity tunable laser diode (TLD). A comparison of the SFL measured spectra with that of the conventional TLD allowed the determination of the absolute wavelength of the absorption features as well as the confirmation of the bandwidth of the SFL produced chirp. Excellent agreement between the spectra for the SFL and TLD sweeps is seen in Figures 2.16a and 2.16b.

The conventional TLD measured spectrum consisted of 1000 sample points which required a measurement time on the order of 10 minutes. By contrast, the SFL produces a continuous frequency sweep with a duration of 1 ms and a repetition rate of 500 Hz. The number of sample points in the SFL measurement is limited by the analog-to-digital converter or oscilloscope used to record the data. In this case, the record length was set to 10,000 points. To illustrate the high spectral resolution of the SFL, a detailed view of the left most absorption line was recorded and is displayed

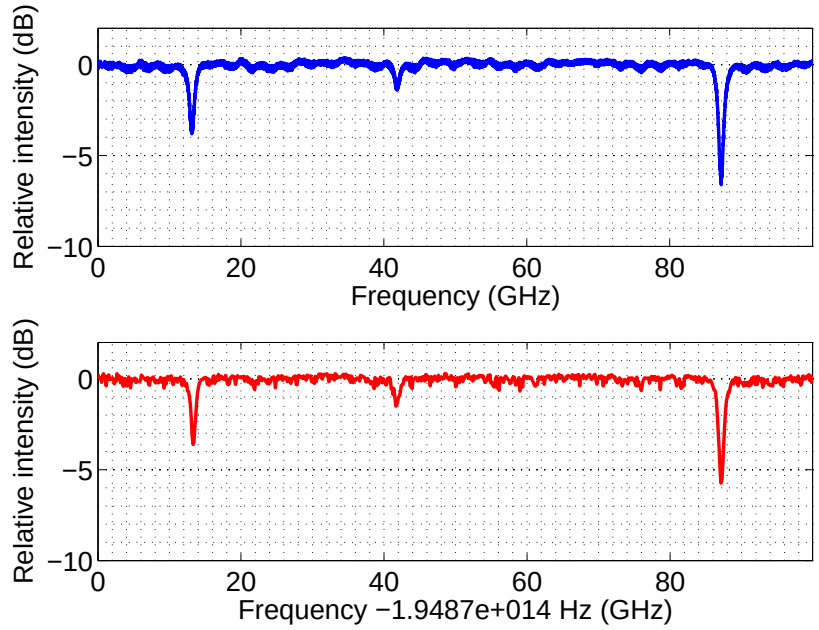

(a)

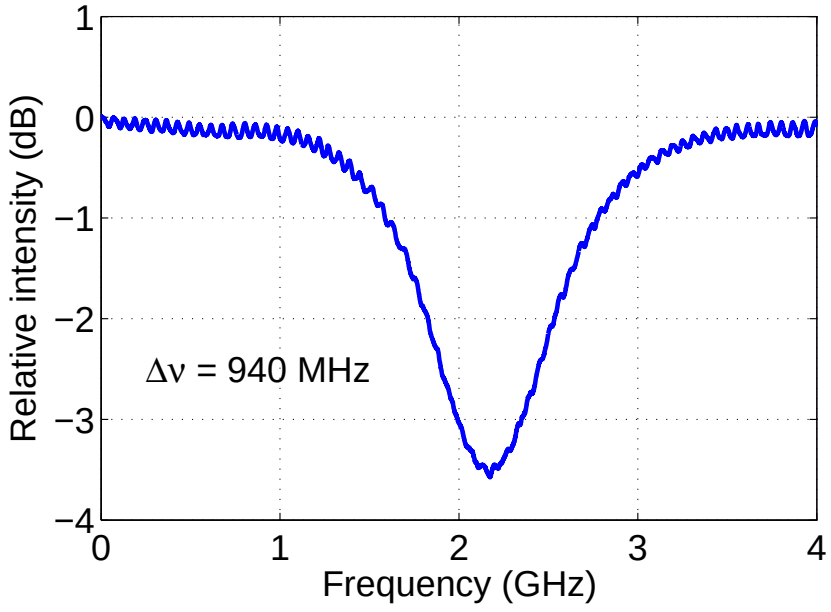

(b)

Figure 2.16: (a) The absorption spectrum of an acetylene gas cell as measured by both the SFL and a conventional external cavity tunable laser (agilent), (b) a detailed view of the left most absorption line in (a) as captured using the SFL source.

in Figure 2.16b. In this detailed view small Fabry-Perot oscillations are visible on top of the main resonance feature most likely due to back reflections from the ends of the gas cell. The ability of the SFL to perform spectroscopic measurements with high speed, at a high rate, and with extreme resolution makes it a valuable tool.

The results from the experimental demonstration of SFL based optical spectroscopy in Figures 2.16a and 2.16b only show the amplitude of the acetylene absorption line. However, it is also possible to measure the phase and therefore the dispersion characteristics of the resonance feature by placing the gas cell within one arm of a Mach-Zhender interferometer and performing IQ demodulation on the detected signal.

Chapter 3

Integrated planar silicon nitride (Si_3N_4) microdisk resonators

3.1 Introduction

Optical micro-resonators, like resonant structures in other branches of physics, are capable of confining and storing wave energy at specific resonant frequencies. They are versatile devices that find applications in many regions of science including: spectroscopy [42], quantum optics [43], cavity quantum electrodynamics [44], and nonlinear optics [45], to name a few. Within optical-electronic engineering, applications of resonators include: lasers, filters, modulators, parametric oscillators, and the subject of this work, label free optical biosensors. Many excellent and thorough treatments of optical resonators — micro and otherwise — exist and the reader is encouraged to consult them for more detail [46–48].

Optical micro-resonators can be designed and fabricated such that they are extremely sensitive to changes in their effective optical path length or equivalently the refractive index of their constituent materials. Careful engineering of the micro-resonator design and fabrication can be used to leverage the device as an effective refractive index transducer for the sensing and measurement of biomolecules in ultra-low, yet biologically relevant, concentrations.

Here, we present some basic resonator concepts before focusing on the design of microdisk optical resonators fabricated from silicon nitride on silica. Simulations of

the nitride are performed and used in conjunction with waveguide mode simulations and a coupled mode perturbation theory formalism to compute coupling coefficients and conditions for the waveguide resonator system in both air and aqueous environments. The thermal characteristics of the microdisk resonant modes including possible designs for athermal operation in the aqueous environment are discussed. Fabrication processes, methods, and experimental measurements of both silica microtoroid and silicon nitride microdisk resonators in both liquid and air environments are presented.

3.2 Traveling wave optical micro-resonators

3.2.1 The resonance condition

In the most basic form, an optical resonator consists of two mirrored surfaces aligned in parallel such that light traveling perpendicular to the mirrors reflects back and forth and is contained within the cavity or space between the mirrors. Assuming that the mirrors are perfect and lossless and imposing the boundary condition that the electric field must vanish at an interface with a perfect electrical conductor we can conceptualize that the number of oscillations in the longitudinal electric field between the mirrors is an integer number of half wavelengths (so that the field may return to a value of zero at each mirror). A cartoon depiction of this scenario is shown in Figure 3.1. The resonant criteria of an integer number of wavelengths fitting into the structure is the basic principle behind many different resonator geometries in which different methods of folding the optical path or constructing the mirrors are employed. Mathematically the resonance condition (in the case of a Fabry-Perot type resonator as shown in Figure 3.1) is given by

$$\lambda m = 2Ln, kL = 2\pi m, \tag{3.1}$$

where λ is the free space wavelength of the resonant optical field, L is the physical length of the resonant cavity, k is the propagation constant of the optical field ($2\pi/\lambda$

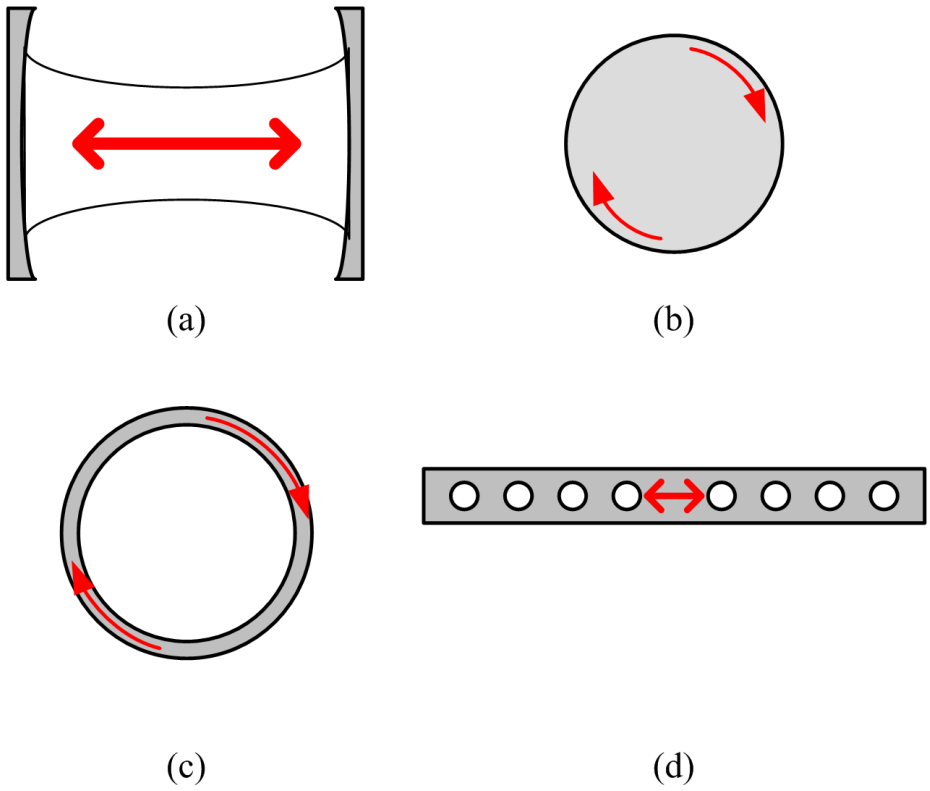

Figure 3.1: Schematic diagrams of various resonator structures including (a) Fabry-Perot etalon, (b) whispering gallery mode disk resonator, (c) ring resonator, and (d) one dimensional defect Bragg resonator. The red arrows indicate the general location and flow of optical energy within the resonator structure.

in free space), n is the refractive index of the material within the resonant cavity and m is an integer. In the case of an axisymmetric resonator such as a microtoroid, microdisk or microring, the resonance condition takes on the form

$$\lambda m = 2\pi R n_{eff}, \tag{3.2}$$

where R is the radius of the path traveled by the mode.

3.2.2 Whispering gallery mode resonances

Resonant structures require some form of closed path for waves to travel allowing for multiple round trips or passes. One such ring-like resonant structure, is known as the whispering galley, named after the famous whispering gallery at Saint Paul's cathedral in London (see Figure 3.2) where one can hear whispers uttered from distant points along the gallery by keeping near to the gallery wall. In the case of acoustic waves, a combination of reflection of sound waves from the curved wall, and the "inertia" of the forward propagating wave, allow them to travel along the wall with little loss and therefore preserve the whispers.

A whispering gallery mode (WGM) optical resonator can be constructed in a similar way such that optical waves propagate around the periphery of a smoothly curved dielectric structure (such as a sphere, torus, or disk), and are guided by total internal reflection at an interface with a lower index dielectric material. A cartoon example of a WGM resonator is shown in Figure 3.1 (b).

The ray optics / total internal reflection picture of waveguiding at the surface of a dielectric disk is helpful to phenomenologcally appreciate why a resonant mode exists. However, this view leaves several important aspects of WGM resonators unexplained, particularly the evanescent field, which is integral to both the radiation loss and input/output coupling of the resonator.

Intuition for some of the subtleties of WGM structures, as well as motivation for a more complete numerical simulation of the WGM modes, can be gained by treating the dielectric disk as a infinite cylinder and utilizing a conformal mapping to solve the

Figure 3.2: A photograph, highlighting the smooth curved cylindrical wall, of the famous whispering gallery at St. Paul's Cathedral in London, England.

wave equation for whispering gallery modes in one dimension. In what follows we will reproduce some of the key concepts from the paper by Heiblum and Harris [49] before moving on to a full numerical FEM based simulation of the microdisk resonators used in this work.

Beginning with the scalar wave equation

$$\nabla_{x,y}^2 E + k^2 (x, y) \psi = 0, \tag{3.3}$$

we can use a conformal transformation by expressing the x, y coordinate plane as the complex plane $z = x + iy$. We can then find solutions in another coordinate system w where $w = u + iv$ and the transformation from z to w is given by

$$w = u + iv = f(z) = f(x + iy), \tag{3.4}$$

where f is an analytic function. Such a transformation from z to w is conformal, i.e. it preserves angles. Under such a transformation

$$\nabla_{x,y}^2 = \nabla^{u,v} \left| \frac{dw}{dz} \right|^2, \tag{3.5}$$

where $|dw/dz|^2 = (\partial u/\partial x)^2 + (\partial v/\partial x)^2$ depends on the particular transformation

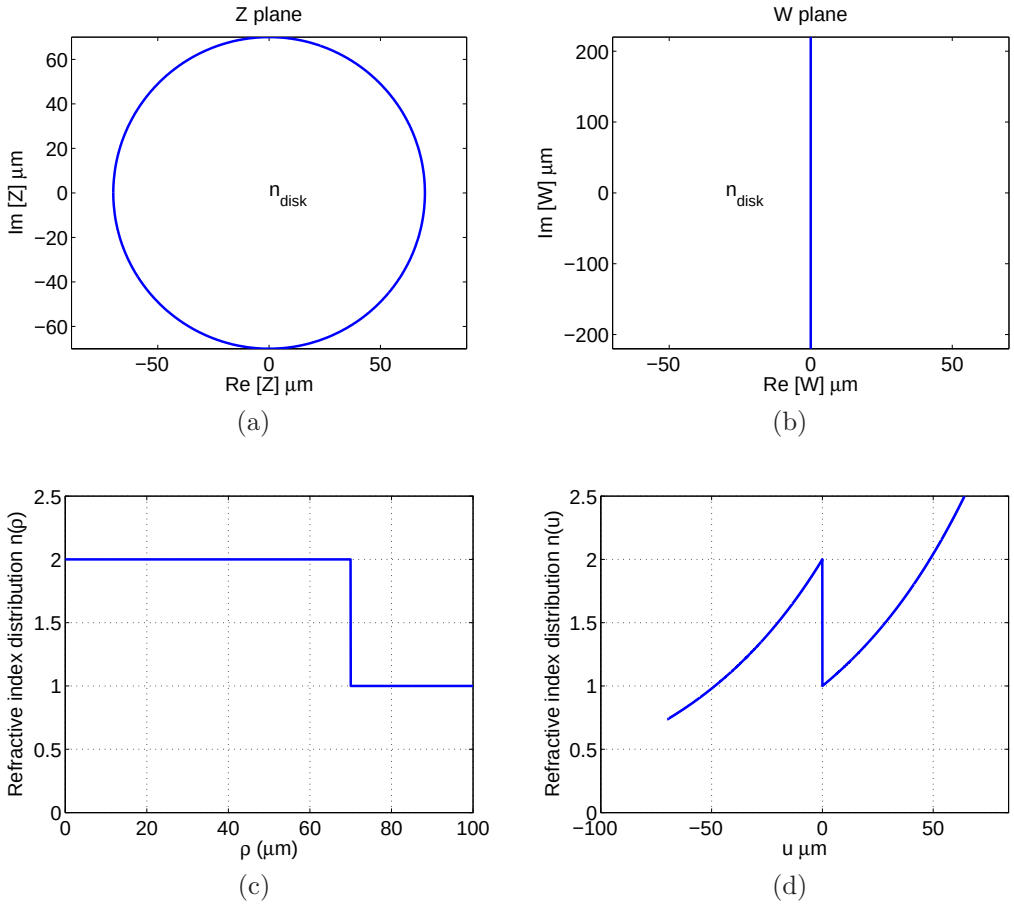

Figure 3.3: (a) A cross section of the infinite disk /cylinder dielectric structure. (b) The cross section of the cylinder structure after conformal transformation. (c) The refractive index profile of the disk. (d) The refractive index profile after conformal transformation.

used. The wave equation is now written as

$$\left[\nabla_{u,v}^2 + \left|\frac{dz}{dw}\right|^2 k^2 \left(x\left(u,v\right)\ y\left(u,v\right)\right)\right]\psi = 0. \tag{3.6}$$

Insight into the existence of the whispering gallery mode can be gained from this equation and its implications alone. The propagation constant term can be decomposed to become

$$\left|\frac{dz}{dw}\right|^2 k^2 \left(x\left(u,v\right), y\left(u,v\right)\right) = \frac{n^2\left(x\left(u,v\right), y\left(u,v\right)\right)\omega^2}{c^2}, \tag{3.7}$$

so that the refractive index n in the w plane is given by

$$n_{u,v} = \left|\frac{dz}{dw}\right| n(x,y). \tag{3.8}$$

Treating the microdisk as an infinite cylinder of refractive index n_{core} with an air cladding we have the refractive index profile shown in Figure 3.3a. We desire to perform a conformal mapping that will unwrap the circular path of the disk into a straight line. To perform this action, we employ the transformation

$$w = R\ ln\left(\frac{z}{R}\right), \tag{3.9}$$

where ln denotes the natural logarithm, and R is the radius of the disk. Figure 3.3b shows the cylindrical geometry of Figure 3.3a transformed under Equation 3.9. The conformal transformation of the refractive index profile is shown in Figures 3.3c and 3.3d. It is from the transformed refractive index profile of the disk structure that the presence of the whispering gallery and mode can be explained. The region of the disk just to the interior of the boundary with the lower index dielectric material presents a local maximum in the refractive index profile that serves to support a leaky guided mode. These solutions to the wave equation are of the form

$$\psi\left(u,v\right) = A\left(u\right)e^{i(\beta+i\alpha)v}, u < R\,ln\left(\frac{n_{disk}}{n_{cladding}}\right), \tag{3.10}$$

where β is the propagation constant, and α is the loss coefficient, and $A(u)$ is the spatial distribution of the mode in w. The losses addressed by α stem from the tunneling of the evanescent field of the guided WGM modes into the high index region outside the disk illustrated in Figure 3.3d. This radiation loss is an important contributor to the intrinsic loss of the WGM mode and allows the coupling of light into and out of the resonant mode. Closed form analytical solutions to the electric field distribution $A(u)$ can be obtained using the WKB approximation as outlined in [49]. Armed with the intuition gained by the conformal mapping of the step index disk structure we move on to full finite element method (FEM) simulations of the WGM microdisk modes using the simulation tool Comsol®.

3.2.3 WGM simulations

Careful design of the planar microdisk resonator and its coupling waveguide are necessary to enable measurement of the transmission spectrum to ensure proper operation of the device in the desired coupling regime in either an air environment, a liquid environment, or both. However, a full three-dimensional finite element simulation for a microdisk structure is too computationally intensive. To reduce the computation time, we exploit the rotational symmetry of the disk structure and solve the wave equation for the resonator modes given a cross-section of the disk.

Beginning with the two Maxwell's curl equations,

$$\nabla \times E = -\frac{1}{\mu}\frac{\partial H}{\partial t}, \tag{3.11}$$

$$\nabla \times H = \epsilon\frac{\partial E}{\partial t}. \tag{3.12}$$

We take advantage of the continuity of the magnetic H field across boundaries due to the uniform magnetic permeability μ. Substituting one equation into the other, we obtain the vector wave equation

$$\nabla \times \left(\frac{1}{\epsilon} \nabla \times H \right) - \alpha \nabla \left(\nabla \cdot H \right) + \frac{1}{c^2} \frac{\partial H}{\partial t} = 0. \tag{3.13}$$

Although the second term on the left hand side containing the divergence of the magnetic field is zero in the absence of magnetic monopoles, it is kept in the equation as a penalty term to suppress spurious numerical solutions. This method for preferentially finding WGM solutions has been used by [50] and [51].

Equation 3.13 can then be re-written in a so called weak form and solved by Comsol using the Galerkin method of weighted residuals [52]. More information on implementing the Galerkin method, specifically in the Comsol partial differential equation solver, can be found in [50].

Solutions of Equation 3.13 are of the form

$$\mathbf{H}\left(\mathbf{r}\right) = e^{iM\phi} \left(H^r, H^\phi, H^z \right), \tag{3.14}$$

where M is the azimuthal mode number and the azimuthal dependence of the field is given by the $\exp\left[\mathrm{iM}\phi\right]$ term.

We performed FEM simulations for the microdisk devices looking for resonant modes in the 1310 nm and 1064 nm wavelength regimes. The dielectric structure simulated including the finite element mesh is shown in Figure 3.4. The structure was divided into three layers, the disk core (silicon nitride), the lower cladding (silica), and the upper cladding (either air or water). The thickness of the core, lower cladding, and upper cladding layers were 250 nm, and 6 μm, and 4 μm respectively. The simulation domain boundaries were treated as perfect electrical conductors. A finer mesh was used in the region of the disk that supports the resonant mode to improve the results of the simulation.

The numerical simulations of the whispering gallery modes presented here serve two purposes. Firstly, they positively indicate that a resonant mode is supported by the geometry and material make up of the given structure and provide estimates of the resonant frequency and mode numbers. Secondly, the information derived from the numerical simulations including the spatial distribution of the electric field,

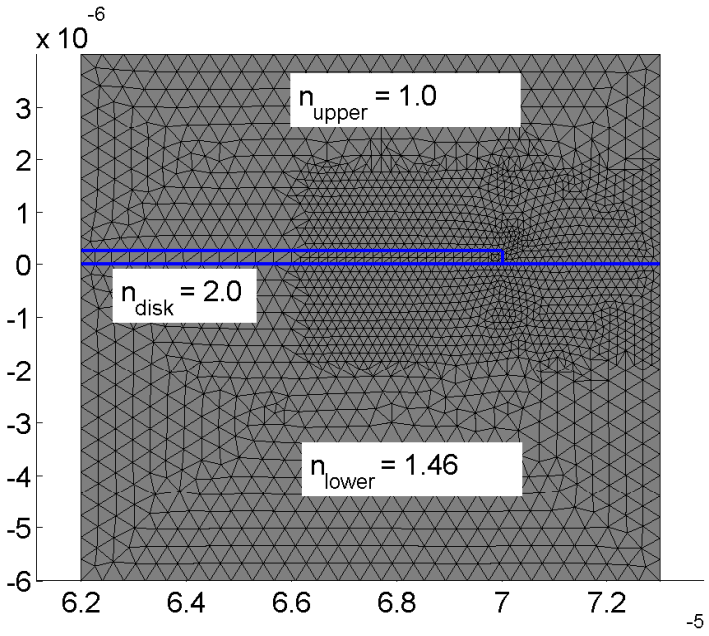

Figure 3.4: A cross section of the dielectric structure and mesh used to simulate WGM modes. Si_3N_4 has a refractive index of 2.0 and serves as the device layer for both the microdisk resonator and the waveguide core. $Si0_2$ is used as the lower cladding layer and has a refractive index of 1.46. A silicon layer, which serves as a substrate for the top two layers, is not included in the simulation.

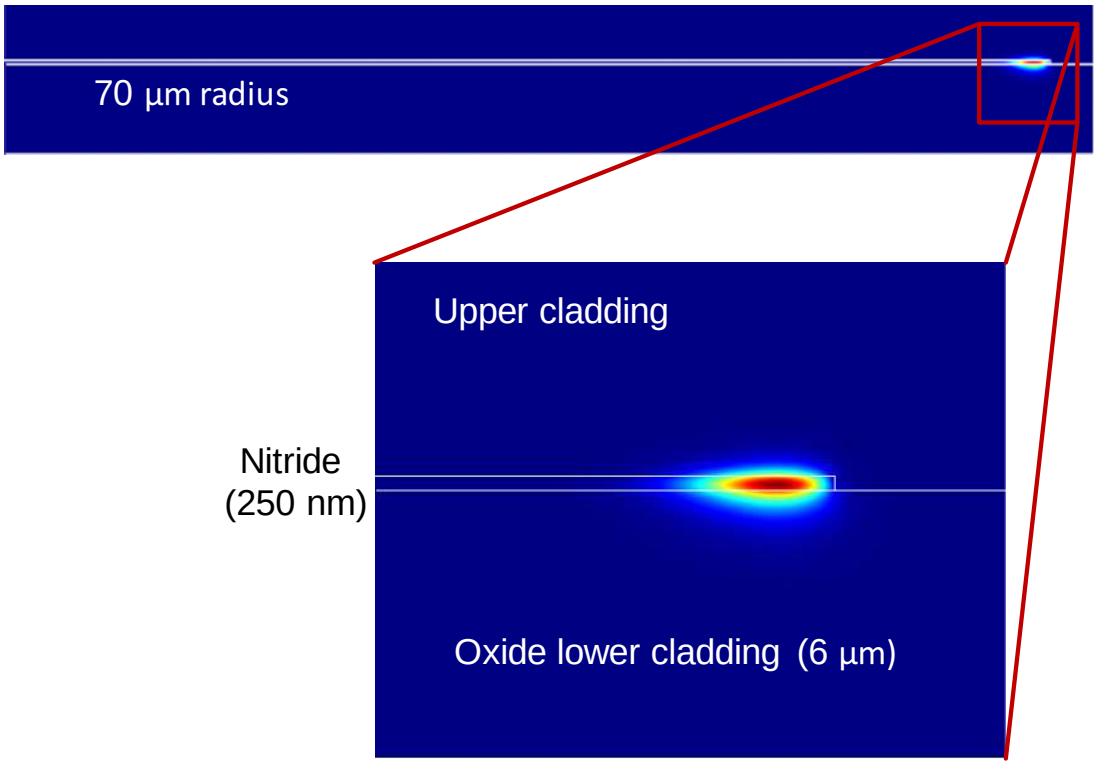

Figure 3.5: A full view of the cross section of the microdisk resonator with an inset showing the intensity of a fundamental radial order mode. The radius of the disk is 70 μm, the thickness of the core layer is 250 nm with a refractive index of $n_{disk} = 2$, and the lower cladding layer is 6 μm thick with a refractive index of $n_{cladding} = 1.46$.

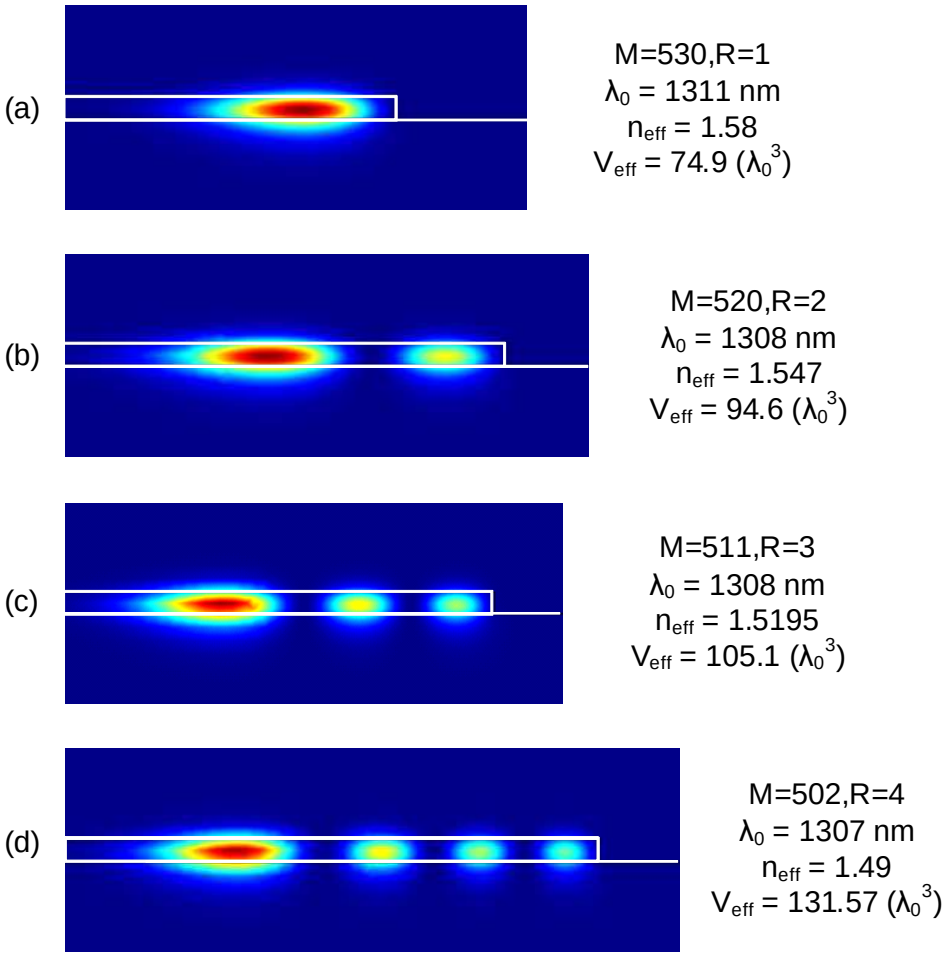

Figure 3.6: Intensity of the radial component of the electric field $|E^r|^2$ of various whispering gallery modes solved using the finite element method in the 1310 nm wavelength regime.(a) R_1 (b) R_2 (c) R_3 (d) R_4 mode.

the eigenfrequency, the effective volume V_{eff}, the effective mode index n_{eff}, and the confinement factors Γ_{disk} and Γ_{cladding} are of use in the design of the waveguide coupling arrangement, and the potential thermal dependence of the resonator / sensor.

3.2.4 Thermal properties of silicon nitride microdisk resonators

The measurements of the transmission spectra of the silicon nitride microdisk resonators in Section 3.4 represent the foundation of the dynamic measurements we wish to perform with the label-free optical biosensing system. Sensing measurements involve the continuous interrogation and monitoring of the transmission spectra of the resonator as its upper cladding is subtly changed thereby altering the effective index of the resonant mode and therefore the resonant wavelength. However, intentional changes to the waveguide cladding are not the sole avenue for perturbing the resonant mode. The refractive index of the materials that comprise the resonator are each a function of temperature. Changes in the ambient temperature affect the very parameter used for sensing bio-molecules and can confound sensing experiments.

Here, we use numerical mode simulations to determine the thermo-optical coefficient (TOC) of the radial order modes of the silicon nitride microdisks. The TOC or $\partial n/\partial T$ of a mode is given by

$$\frac{\partial n}{\partial T_{total}} = \frac{\partial n}{\partial T_{core}}\Gamma_{core} + \frac{\partial n}{\partial T_{lower}}\Gamma_{lower} + \frac{\partial n}{\partial T_{upper}}\Gamma_{upper}, \tag{3.15}$$

where each of the $\partial n/\partial T$ terms is dependent on the material of each disk region and Γ is the confinement factor of mode field within each region. Table 3.1 lists values for the cladding and disk materials that will be used in the microdisk label-free biosensing system. The negative slope of the water temperature index response suggests that

Material	Si_3N_4	SiO_2	Water
$\partial n/\partial T$	3×10^{-5}	1×10^{-5}	-8×10^{-5}

Table 3.1: Values of the thermo-optic coefficient for several materials of interest [2–4].

it may be possible to engineer the resonator geometry to balance the positive and negative $\partial n/\partial T$ components. Such a resonator could be considered athermal over a range of operating temperatures.

Water is one amongst a group of materials with negative thermo-optical effect coefficients. Other work has used polymer upper cladding layers with negative $\partial n/\partial T$ values to achieve athermal operation of integrated ring resoantor filters [53]. Work on label-free optical biosensing using silica microtoroid resonators by Armani et al. also used this analysis to minimize thermal drift of their resonators [12].

FEM simulations of the R_1 through R_4 modes of the microdisk with a water upper cladding were used to determine the confinement factors in each material region. $\partial n/\partial T_{total}$ was then calculated based on the simulated confinement factors and values for the index temperature variation coefficient taken from the literature [54]. The calculated TOC was approximately $1.6 \times^{-5}$ RIU/K for all of the modes considered. This value in conjunction with a temperature controlled device stage with an accuracy of 0.01°C, could reduce ambient thermal refractive index drift to the level of 1×10^{-7} RIU.

We also note that the sign of the TOC is positive. We should therefore expect that when the resonator is immersed in water, increases in the device temperature in generally will result in an increase in the modal index, and therefore a red shift in the resonant frequency.

3.2.5 Resonant field behavior

The spatial profile of the WGM modes determined by FEM simulations are important in determining the behavior of the modes for sensing and coupling purposes. The temporal behavior of the resonant mode is also of critical importance. Here, we investigate the temporal behavior of the mode in order to study the intrinsic and coupling losses of the resonator and their effect on its spectral properties.

Practical resonators experience losses both intrinsic and extrinsic. Intrinsic losses can be due to a variety of phenomena including material absorption, scattering, ra-

diation, coupling to undesired modes, and surface states. Extrinsic loses are due to coupling between the resonator and the outside world via an intensionally imperfect mirror, or in some resonator geometries a fiber taper [55] or integrated waveguide [56, 57].

Following the derivation outlined by H. Haus in [46] we will look at the behavior of a resonant optical field in the time domain. We start by writing the equation of motion for the field $a(t)$ in the case of an uncoupled resonator

$$\frac{da}{dt} = i\omega_0 a - \frac{1}{\tau_0}a, \tag{3.16}$$

where ω_0 is the resonant frequency, and $1/\tau_0$ represents the intrinsic loss rate of the resonator. The intrinsic loss rate can be written as the sum of its constituent loss channels

$$\frac{1}{\tau_0} = \frac{1}{\tau_{rad}} + \frac{1}{\tau_{abs}} + \frac{1}{\tau_{sc}}, \tag{3.17}$$

where τ_{rad}, τ_{abs}, and τ_{sc} represent the loss rates due to radiation, material absorption, and scattering respectively.

From the right hand side of Equation 3.16 we see that the phase of the field within the resonator processes at a rate of ω_0 as expected and will decay exponentially at the rate determined by $1/\tau_0$.

In the case where the resonator is coupled to the outside world, an additional decay term is added to the right hand side to address the presence of the additional loss channel. Equation 3.16 then becomes

$$\begin{aligned}\frac{da}{dt} &= i\omega_0 a - \frac{1}{\tau_0}a - \frac{1}{\tau_e}a \\ &= a\left(i\omega_0 - \left(\frac{1}{\tau_0} + \frac{1}{\tau_e}\right)\right),\end{aligned} \tag{3.18}$$

where $1/\tau_e$ is the decay rate due to coupling of the resonator to the external environment.

It is instructive to look at the rate of change of the energy in the resonator W given by $W = |a|^2$. The temporal behavior of the energy of the resonator, or power flow, can be expressed as

$$\frac{dW}{dt} = \frac{d\,|a|^2}{dt} = a^* \frac{da}{dt} + a\frac{da^*}{dt} \tag{3.19}$$

$$= -2\left(\frac{1}{\tau_0} + \frac{1}{\tau_e}\right) W. \tag{3.20}$$

The power dissipated within the resonator P_d and the power escaping the resonator through external coupling P_e are therefore given by

$$P_d = \frac{2}{\tau_0} W, \tag{3.21}$$

$$P_e = \frac{2}{\tau_e} W. \tag{3.22}$$

To characterize the amount of optical power stored in the resonator, we define the quality factor or Q. It is a dimensionless number that is given as the ratio of the energy stored in the resonator per optical cycle to the energy dissipated by the resonator per cycle:

$$Q = \omega_0 \times \frac{\text{stored energy}}{\text{dissipated power}} = \frac{\omega_0 W}{P}. \tag{3.23}$$

Using both Equations 3.21, 3.22 and the definition of the Q factor Equation 3.23, we can describe both the power dissipated within the resonator due to internal losses and the power dissipated due to external coupling of the resonator with Q factors Q_0 and Q_e respectively. They are referred to as the intrinsic Q and the external or coupling Q and are given by

$$\frac{1}{Q_e} = \frac{P_e}{\omega_0 W} = \frac{2}{\omega_0 \tau_e}, \tag{3.24}$$

$$\frac{1}{Q_0} = \frac{P_d}{\omega_0 W} = \frac{2}{\omega_0 \tau_0}. \tag{3.25}$$

It is instructive to define a loaded quality factor Q_L that encompasses both the intrinsic loss sources and the external coupling loss mechanism:

$$\frac{1}{Q_L} = \frac{1}{Q_e} + \frac{1}{Q_0}. \tag{3.26}$$

The loaded Q is what will be obtained by measuring the transmission spectrum of the resonator waveguide system. From this loaded Q, it is then possible to determine the individual contributions of external coupling loss and intrinsic loss if the nature of the external coupling is known.

Similarly, we can decompose the intrinsic loss channels outlined in Equation 3.17 in terms of a quality factor

$$\frac{1}{Q_0} = \frac{1}{Q_{rad}} + \frac{1}{Q_{abs}} + \frac{1}{Q_{sc}}. \tag{3.27}$$

It is difficult to experimentally determine the values for each of the individual intrinsic Q contributions however some studies have done so by implementing artificial scatterers [58] or by studying the onset of nonlinear effects [59].

3.2.6 Resonator waveguide coupling

Measurement of the coupled resonator requires the addition of power to the system and the measurement of the transmitted power in the waveguide past the resonator. We define the power of the incident wave as $|S_+|^2$ and rewrite the equation of motion of the field within the resonator to reflect the addition of this field as

$$\frac{da}{dt} = a\left(i\omega_0 - \left(\frac{1}{\tau_0} + \frac{1}{\tau_e}\right)\right) + \kappa S_+, \tag{3.28}$$

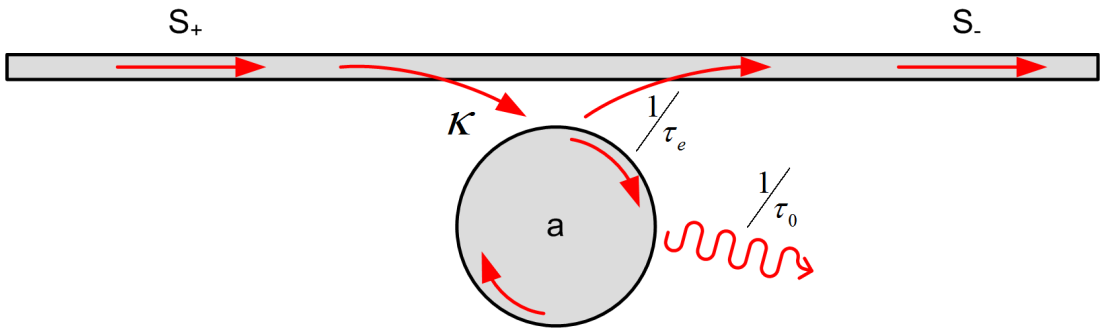

Figure 3.7: A schematic of the microdisk resonator waveguide system showing the input field S_+, the resonant field a, the output field S_- and the loss and coupling rates τ_0 τ_e and κ.

where κ is the rate at which the input field S_+ is coupled into the resonator. Taking the Fourier transform of Equation 3.28 and assuming steady state conditions, we can write the field as

$$a(\omega) = \frac{\kappa S_+}{i(\omega - \omega_0) + \left(\frac{1}{\tau_0} + \frac{1}{\tau_e}\right)}, \tag{3.29}$$

following a time reversal symmetry argument, it can be shown that the incident field coupling coefficient κ is related to the external decay rate τ_e by

$$\kappa = \sqrt{\frac{2}{\tau_e}}. \tag{3.30}$$

The difference in scaling between the two coupling rates shown in Equation 3.30 is due to the difference in normalization between the resonator field and the waveguide field. Recall that the resonator field is normalized such that $|a|^2 = W$, while the waveguide field was normalized such that $|S_+|^2 = P$.

The resonator geometry of interest in this work is that of the microdisk coupled to a waveguide shown in Figures 3.1(b) and 3.7. We are interested in and will be measuring the transmitted power $|S_-|^2$. The transmitted field S_- is a linear combination of the input field S_+ and the resonator field a and can be written

$$S_- = C_1 S_+ + C_2 a, \tag{3.31}$$

where C_1 and C_2 are constant coefficients. The case of no input power into the waveguide can be used to determine $C_2 = \kappa = \sqrt{2/\tau_e}$. Conservation of energy, namely that the difference between the input and transmitted power must be equal to sum of the circulating power and the internally dissipated power, is expressed as

$$|S_+|^2 - |S_-|^2 = \frac{d}{dt}|a|^2 + \frac{2}{\tau_0}|a|^2, \tag{3.32}$$

and leads to $C_1 = -1$.

The main results of this discussion are the following equations

$$\frac{da}{dt} = a\left(i\omega_0 - \left(\frac{1}{\tau_0} + \frac{1}{\tau_e}\right)\right) + \kappa S_+, \tag{3.33}$$

$$S_- = -S_+ + \sqrt{\frac{2}{\tau_e}}a, \tag{3.34}$$

which fully describe the coupled resonator waveguide system. We can now express the normalized amplitude transmission as

$$t(\omega) = \frac{S_-}{S_+} = \frac{1/\tau_e - 1/\tau_0 - i(\omega - \omega_0)}{1/\tau_e + 1/\tau_0 + i(\omega - \omega_0)}, \tag{3.35}$$

and the normalized power transmission as

$$T = |t(\omega)|^2 = \left|\frac{S_-}{S_+}\right|^2 = \left|\frac{1/\tau_e - 1/\tau_0 - i(\omega - \omega_0)}{1/\tau_e + 1/\tau_0 + i(\omega - \omega_0)}\right|^2. \tag{3.36}$$

To analyze the structure of the power transmission spectrum, and gain some intuition for the important parameters in the design of a micro-resonator and its coupling, it is helpful to define

$$K = \tau_e/\tau_0 = Q_0/Q_e. \tag{3.37}$$

Substituting Equation 3.37 into Equation 3.36 and plotting the result vs. normalized frequency detuning we obtain the normalized resonator transmission spectra shown in Figure 3.8. From Equation 3.37 and Figure 3.8 we see that there are clearly three

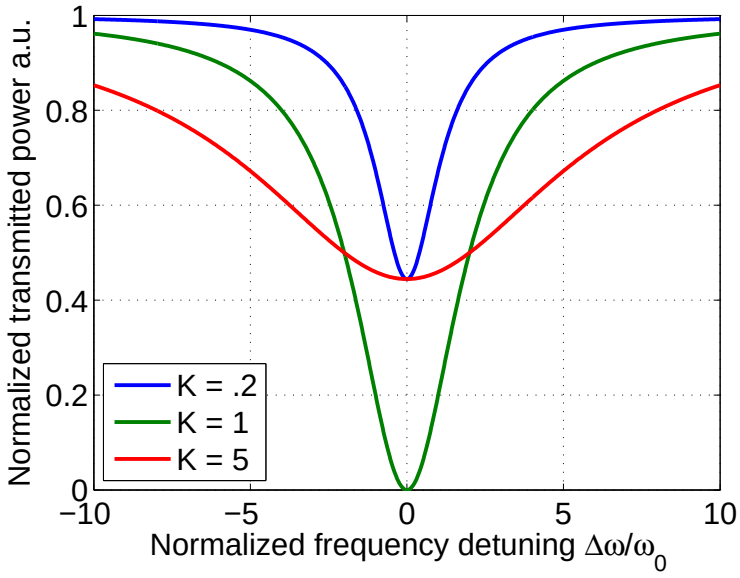

Figure 3.8: A demonstration of the three possible resonator waveguide coupling regimes based on equations 3.36. The blue, green, and red curves correspond to under-coupled, critically-coupled, and over-coupled scenarios respectively. K is the ratio of the internal loss rate to external coupling rate, τ_e/τ_0 or in terms of Q factor, Q_0/Q_e.

domains of resonator coupling:

1. **Under-coupled** — the under-coupled regime occurs where $K < 1$ or equivalently, $\tau_e < \tau_0$ or $Q_0 < Q_e$. Under coupling can be recognized from the transmission spectrum of a resonator waveguide system when the minima of the transmitted power does not reach zero and the full width at half maximum (FWHM) of the spectrum is measured to be less than that of the resonator in either the critically-coupled or over-coupled states. An example of five times under coupling is shown in Figure 3.8. In the under-coupled case, internal losses of the resonator dominate the coupling losses.

2. **Critically-coupled** — the critically-coupled regime occurs where $K = 1$ or equivalently, $\tau_e = \tau_0$ or $Q_0 = Q_e$. Critical coupling [47, 60, 61] is unmistakable and can be recognized easily as the minimum of the transmitted power reaches zero. This implies that critical coupling results in the maximum circulating power within the resonator for a given input power. An example of critical-

coupling is shown in Figure 3.8. In the critically-coupled case, loss due to the waveguide is tuned to exactly match the intrinsic loss. An alternative interpretation is that the light escaping the resonator to the waveguide is precisely 180° out of phase with the light in the waveguide resulting in destructive interference. In practice, it is difficult to achieve true critical coupling though it is possible to come close to it.

3. **Over-coupled** — the over-coupled regime occurs where $K > 1$, or equivalently, $\tau_e > \tau_0$ or $Q_0 > Q_e$. Over coupling can be recognized from the transmission spectrum of a resonator waveguide system when the minimum of the transmitted power does not reach zero and the full width at half maximum (FWHM) of the spectrum is much wider than that of the resonator in either the critically-coupled or under-coupled states. An example of five times over-coupling is shown in Figure 3.8. In the over-coupled case, the waveguide is the dominant source of loss.

3.2.7 Clockwise and counter-clockwise resonant modes

The previous discussion of the time dependent behavior of the resonator mode field assumed that the resonant mode traveled in a single direction. The perfect microdisk resonator waveguide structure shown in Figure 3.7 supports two degenerate whispering gallery modes for each set of mode numbers, a clockwise propagating mode and counter-clockwise propagating mode. In the case of an ideal resonator, these modes are fully degenerate and can be treated identically as in Section 3.2.5. In practical resonators, slight refractive index perturbations due to surface roughness on the sidewall of the resonator serves to couple to two modes and break the degeneracy resulting in resonance splitting or doublet resonance. Doublet resonances are typically seen only for narrow linewidth modes as the splitting must be on the order of the linewidth to be resolved in the transmission spectrum.

Considering both the clockwise and counter-clockwise propagating modes, the equations of motion for the coupled system are written as

$$\frac{da_{cw}}{dt} = a_{cw} i\Delta\omega - \left(\frac{1}{\tau_0} + \frac{1}{\tau_e}\right) a_{cw} + \kappa S_+ + \frac{1}{\gamma_{12}} a_{ccw}, \tag{3.38}$$

$$\frac{da_{ccw}}{dt} = a_{ccw} i\Delta\omega - \left(\frac{1}{\tau_0} + \frac{1}{\tau_e}\right) a_{ccw} + \frac{1}{\gamma_{21}} a_{cw}, \tag{3.39}$$

where a_{cw} and $\mathrm{a_{ccw}}$ are the clockwise and counter-clockwise propagating mode amplitudes respectively, and γ_{12} and γ_{21} are the coupling rates between the modes. $\Delta\omega$ represents the detuned resonant frequency of the modes with respect to ω_0.

In the steady state, the mode amplitudes are given by

$$a_{cw}(\omega) = \frac{\kappa s_+ \left(i\Delta\omega + \left(\frac{1}{\tau_0} + \frac{1}{\tau_e}\right)\right)}{-\Delta\omega^2 + \left(\frac{1}{\tau_0} + \frac{1}{\tau_e}\right)^2 - \gamma^2 + i\Delta\omega + \left(\frac{1}{\tau_0} + \frac{1}{\tau_e}\right)}, \tag{3.40}$$

$$a_{ccw}(\omega) = \frac{\kappa s_+ i2\gamma}{-\Delta\omega^2 + \left(\frac{1}{\tau_0} + \frac{1}{\tau_e}\right)^2 - \gamma^2 + i\Delta\omega + \left(\frac{1}{\tau_0} + \frac{1}{\tau_e}\right)}. \tag{3.41}$$

The power transmission spectrum of the doublet resonance is therefore

$$T = \frac{\left|s_+ - \kappa\left(a_{cw} + a_{ccw}\right)\right|^2}{\left|s_+\right|^2}. \tag{3.42}$$

3.3 Microdisk resonator and waveguide coupling simulations

In Section 3.2.6 the concepts of critical, over, and under coupling were developed and related to the quality factors Q_e and Q_0. In order to design a practical integrated microdisk resonator waveguide system of the type shown in Figure 3.7, the geometric and material parameters of the device must be translated into corresponding values for Q_e. This translation requires the numerical simulation of both the microdisk resonator modes as described in Section 3.2.3 and of the waveguide modes as well as computation of the coupling Q.

3.3.1 A coupled mode approach to resonator waveguide coupling

We will follow a perturbation theory approach similar those formulated in [47] and [46] to arrive at an expression for the coupling coefficient κ or similarly the coupling quality factor Q_c. In this calculation, we assume that the region of interaction between the waveguide and disk is short compared to the curvature of the disk such that disk can be approximated as a waveguide and that an argument similar to that of the coupling of two parallel waveguides can be used. In this case, the electric field of the whispering gallery mode is written as

$$\mathbf{E}_{disk} = \mathbf{E}_{disk\perp}(x,y)\, e^{i(\omega t - M\theta)}, \tag{3.43}$$

with the waveguide mode written as

$$\mathbf{E}_{wg} = \mathbf{E}_{wg\perp}(x,y)\, e^{i(\omega t - \beta_{wg} z)}. \tag{3.44}$$

It can be shown that the coupling coefficient between the waveguide and resonator modes $\kappa_{wg,disk}$ at a given longitudinal location z is

$$\kappa_{wg,disk}(z) = \frac{\omega\epsilon_0}{4}\int_x\int_y E^*_{wg}\Delta\epsilon(x,y)\, E_{disk} dxdy. \tag{3.45}$$

Using a conservation of power argument, the total coupling between the resonator and waveguide mode over the complete length of interaction is

$$\kappa = \frac{-i\omega\epsilon_0}{4}\int_z\int_x\int_y E^*_{wg}\Delta\epsilon(x,y)\, E_{disk} dxdydz, \tag{3.46}$$

where we have dropped the subscript on κ for brevity.

We recall that in Section 3.2.5 we set up the equations of motion for the resonator field $a(t)$ and the waveguide field s_+ such that they were normalized to unit energy and unit power respectively. Those same normalizations are used in the calculation of κ from Equation 3.46. To obtain the normalization factors from the numerical

simulations we express the resonator energy W_{disk} as

$$W_{disk} = \frac{1}{2}\epsilon_0 \epsilon_{disk} E^2_{max,disk} V_{eff}, \tag{3.47}$$

where ϵ_{disk} is the relative dielectric constant of the silicon nitride disk core, $E_{max,disk}$ is the maximum value of the electric field in the disk, and V_{eff} is the effective mode volume of the microdisk mode given by

$$V_{eff} = \frac{\int\int\int \epsilon\,(x\,y\,z)\,|\mathbf{E}_{disk}\,(x\,y\,z)|^2\,dxdydz}{\max\left[\epsilon\,(\mathrm{x,y,z})\,|\mathbf{E}_{\mathrm{disk}}\,(\mathrm{x,y,z})|^2\right]}. \tag{3.48}$$

We express the power flux through the waveguide as

$$P_{wg} = \frac{1}{2}\epsilon_0 \epsilon_{wg} E^2_{max,wg} A_{eff} v_g, \tag{3.49}$$

where A_{eff} is the effective mode area of the waveguide given by

$$A_{eff} = \frac{\left(\int\int |\mathbf{E}_{wg}\,(x,y)|^2\,dxdy\right)^2}{\int\int |\mathbf{E}_{wg}\,(x,y)|^4\,dxdy}, \tag{3.50}$$

and v_g is the group velocity of the mode given by

$$v_g = \frac{\partial\omega}{\partial\beta_{wg}}. \tag{3.51}$$

Equation 3.46 can then be written as

$$\kappa = \frac{-i\omega\epsilon_0}{4}\int_z\int_x\int_y \Delta\epsilon\,(x,y)\,\frac{E^*_{\perp wg}}{\sqrt{P_{wg}}}\frac{E_{\perp disk}}{\sqrt{W_{disk}}}e^{iM\theta}e^{-i\beta_{wg}z}dxdydz. \tag{3.52}$$

Where we have chosen to write the electric field of both the disk and waveguide in the form of Equations 3.43 and 3.44 to explicitly reveal the importance of both the transverse field overlap terms and the phase matching terms. Expanding the expressions for W_{disk} and $\mathrm{P_{wg}}$ in Equation 3.52 can grant us some additional insight

into the role of each parameter in the coupling.

$$\kappa = \frac{-i\omega}{2} \int_z \int_x \int_y \Delta\epsilon\left(x,y\right) \frac{E^*_{\perp wg}}{|E_{wg,max}|} \frac{E_{\perp disk}}{|E_{disk,max}|} \frac{e^{iM\theta} e^{-i\beta_{wg} z}}{\sqrt{\epsilon_{wg}\epsilon_{disk} V_{eff} A_{eff} v_g}} dxdydz, \quad (3.53)$$

or using the expression for the coupling quality factor $Q_c = \omega / |\kappa|^2$,

$$Q_c = \frac{4 V_{eff} A_{eff} v_g n_{wg}^2 n_{disk}^2}{\omega \left| \int_z \int_x \int_y \Delta\epsilon\left(x,y\right) \frac{E^*_{\perp wg}}{|E_{wg,max}|} \frac{E_{\perp disk}}{|E_{disk,max}|} e^{iM\theta} e^{-i\beta_{wg} z} dxdydz \right|^2}. \quad (3.54)$$

From Equation 3.54 we see that while Q_c is proportional to the effective volume of the resonator and therefore is dependent on the radius of the disk, it is the value of the integral that plays the largest role in determining the strength of the coupling between the waveguide and the resonator. The integral has two main components: the overlap of the waveguide and disk modes within the waveguide, and the phase matching between the two modes.

The evanescent field of the disk decreases exponentially away from the outer boundary of the disk, therefore Q_c will have an exponential dependence on the distance between the resonator and the waveguide, also referred to as the coupling gap. The phase matching term $e^{iM\theta} e^{-i\beta_{wg} z}$ greatly impacts the value of the integral. A large phase mismatch between the waveguide and disk modes can result in little or no energy transfer. In the ideal case, the propagation constant of the waveguide mode and the effective propagation constant of the microdisk mode would be equal. In practice this is is extremely difficult to achieve as the propagation constants of the microdisk mode and waveguide mode are very different. The integration volume, or more specifically, the length of the integral over the z, direction also plays a major role in the determination of the value of Q_c. In the case of disk to waveguide coupling where the modes are only interacting over a short distance, we choose the interaction length, and therefore the limits of the integral over z in Equation 3.54, to be such that the angle swept out over the disk is small, i.e., $tan\left(\theta\right) \approx \theta$.

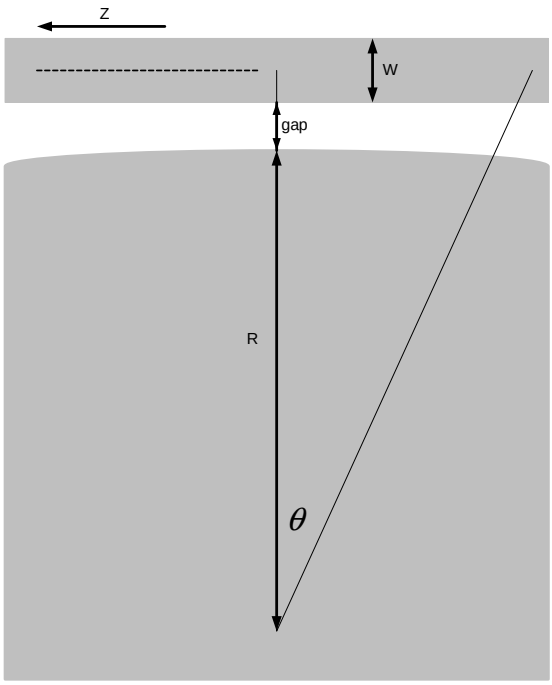

Figure 3.9: A schematic diagram of the coupling region illustrating the relevant dimensions. w is the waveguide width, g is the closest distance between the waveguide and the microdisk, and R is the radius of the microdisk.

In order to integrate over the direction of propagation, it is helpful to write the azimuthal phase dependence of the microdisk as a function of z rather than θ. From Figure 3.9 we can write

$$tan\,(\theta) = \frac{z}{R + g + w/2}. \tag{3.55}$$

In the case where θ is small (an approximation that we are already making), such that $tan\,(\theta) \approx \theta$, we can directly substitute Equation 3.55 into the phase-matching condition such that

$$e^{iM\theta} e^{-i\beta_{wg} z} = e^{iMz/(w/2+g+R)} e^{-i\beta_{wg}}. \tag{3.56}$$

This expression is enough to be able to numerically compute Q_c, however we can again gain insight into the disk / waveguide system by using the resonance condition for the microdisk modes from Equation 3.2 in Equation 3.56 to obtain the phase matching condition

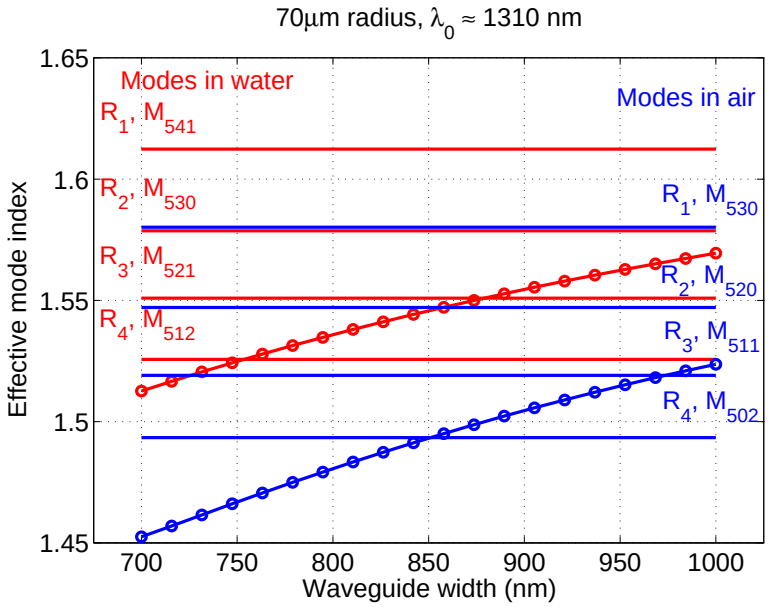

(a)

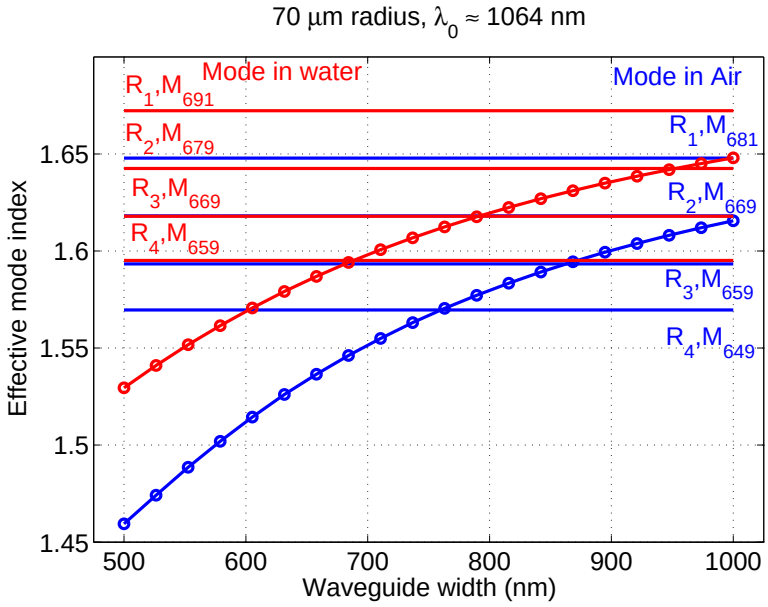

(b)

Figure 3.10: (a) The effective index of the relevant WGM modes of a 70 μm radius 250 nm tall microdisk resonator along with the effective index of the waveguide mode as a function of the waveguide width at 1310 nm with an upper cladding material of water (red) and air (blue). (b) The effective index of the relevant WGM modes of a 70 μm radius 250 nm tall microdisk resonator along with the effective index of the waveguide mode as a function of the waveguide width at 1064 nm with an upper cladding material of water (red) and air (blue).

$$e^{ik_0 z(n_{disk}\eta - n_{wg})}, \tag{3.57}$$

where $\eta = R/(R + w/2 + g)$. From Equation 3.57 it is clear that minimizing the difference between the modified microdisk mode effective index $n_{disk}\eta$ and the effective index of the waveguide mode n_{wg} will result a greater Q_c. In order to get an initial indication of which microdisk modes in the disk would be most accessible from a phase-matching perspective, we compute via numerical simulation the effective index of the various microdisk modes, with different radial and azimuthal mode numbers such that their resonant frequencies fall into our wavelength regime of interest, namely 1310 nm and 1064 nm. We also compute the effective index of the guided mode of a single mode waveguide in the same material system as a function of the width of the waveguide in order to help determine the proper waveguide width from a phase-matching perspective. The results of these calculations are shown in Figures 3.10a and 3.10b.

The height of both the waveguide and microdisk are set by the thickness of the silicon nitride device layer, in this case 250 nm. Therefore, the waveguide width is the only adjustable parameter capable of affecting the propagation constant, and through Equation 3.57 the phase-matching condition of the coupling. TE guided modes of the silicon nitride waveguides were simulated over a range of widths in which they support a single mode, with both an air and a water upper cladding, at both 1310 nm and 1064 nm. These are the conditions in which the waveguides will be required to operate as part of the label-free optical biosensor.

From Figure 3.10a it is clear that at 1310 nm there is a large difference between the effective index of the fundamental radial order microdisk mode and the wavgguide mode over the entire range of widths. This difference is also more pronounced in air than it is in water. In both cases, the disk mode is better confined to the core region than is the waveguide mode. When the waveguide is immersed in water, the index contrast between the nitride core and the upper cladding is lower than in the case of air. The water pulls the mode up into the core region and increases its effective index.

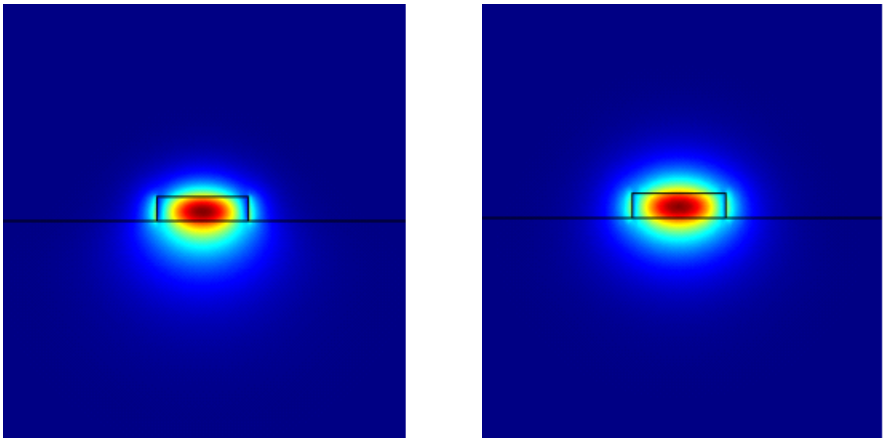

Figure 3.11: The spatial distribution of the transverse electric field Ex of the TE guided mode of a 250 nm × 950 nm silicon nitride waveguide with silica lower cladding and (a) air (n = 1) upper cladding and (b) water (n = 1.33) upper cladding.

Looking at the spatial distribution of the waveguide mode shown in Figure 3.11, it is clear that in case of air cladding (a) the mode has a large component in the silica lower cladding layer, whereas in (b) the amount of the mode confined to silica lower cladding is less. The confinement factor Γ_{upper} was calculated to be $\Gamma_{air} = 0.478$ and $\Gamma_{water} = 0.491$ and the effective indices were $n_{eff,air} = 1.519$ and $n_{eff,water} = 1.567$. Due to the large difference in effective index between the fundamental mode of the disk and the waveguide mode in air at 1310 nm, it is necessary to place the waveguide and disk close together to increase the field overlap and improve coupling. The effective indices are a closer match when the upper cladding is water; this improves the phase matching condition.

We also note that there is a range of waveguide widths which are single mode in both wavelength regimes of interest in both air and water environments. This will enable the same device to work in both wavelength regimes by simply switching SFL sources. This is an advantage of the silicon nitride on silica material system. A device fabricated in a silicon on insulator (SOI) platform would not be able to operate in both wavelength regimes due to optical absorption in silicon at wavelengths below 1100 nm.

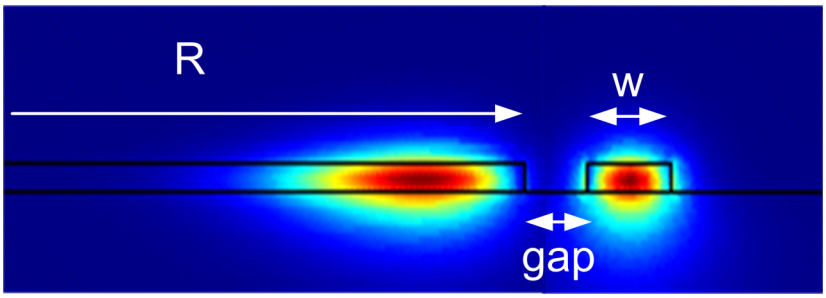

Figure 3.12: A view of the transverse plane in which coupling between the waveguide mode (right side) and the microdisk resonator WGM (left side) takes place. The important geometrical dimensions are labeled.

3.3.2 Numerical coupling simulation results

We now turn our attention to the results of the full simulation and calculation of the coupling coefficient κ and the coupling quality factor Q_c.

The integration of Equation 3.54 was performed using the necessary values calculated in Comsol along with the the spatial distribution of the waveguide and microdisk electric fields as found by FEM simulation in Comsol. The normalized field distributions of the waveguide and resonator fields within the perturbation region as well as the product of the two are shown in Figure 3.13. The exponential decay of the microdisk mode field within the waveguide is clear from the upper panel of the figure. The lower panel shows that most of the field overlap, and therefore exchange of energy between the two modes, takes place in the region of the lower region of the waveguide closest to the the microdisk.

Coupling coefficients were simulated over a variety of coupling gap and waveguide widths while maintaining a microdisk resonator radius of 70 μm and silicon nitride layer thickness of 250 nm. The refractive index of the silicon nitride was taken to be $n_{nitride} = 2.0$ and the refractive index of the silica lower cladding was taken to be $n_{silica} = 1.46$. The refractive index of the upper cladding was taken to be either air with $n_{air} = 1.0$ or water with $n_{water} = 1.33$. Cases of both air and water upper cladding were calculated to determine an appropriate range of designs that would work in both environments. Simulated coupling coefficients for both air and water clad devices in the 1310 nm wavelength regime are shown in Figures 3.14a through

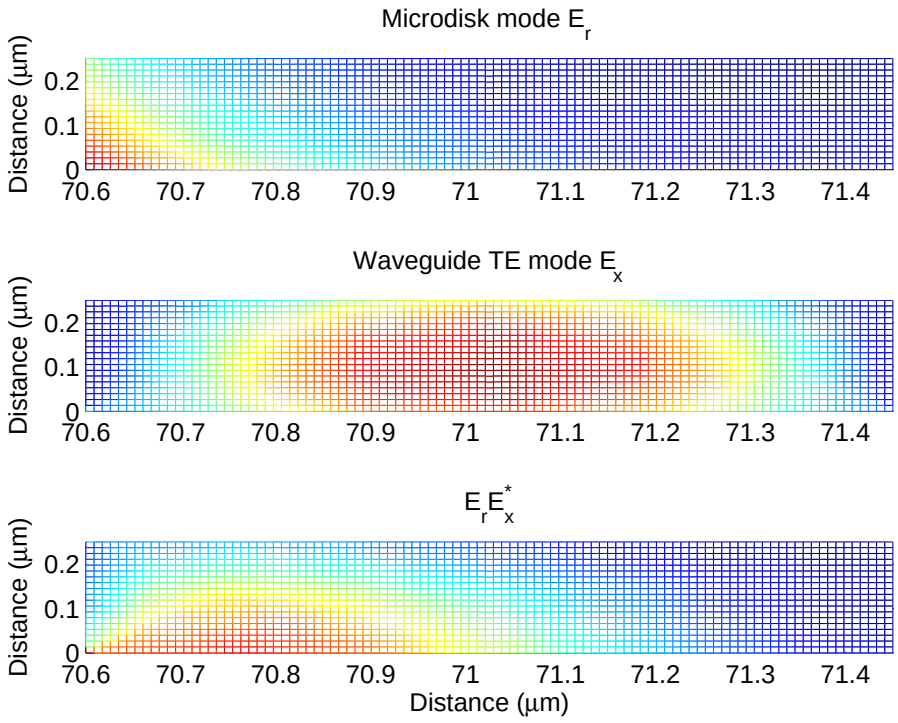

Figure 3.13: Normalized electric field distributions of the microdisk resonator field (top), the waveguide electric field (middle) and the product of the two (bottom) within the waveguide core for a 250 nm $\times$ 950 nm waveguide and the $R = 1, M = 530$ mode of a 70 μm microdisk. The gap between the waveguide and the disk is 600 nm.

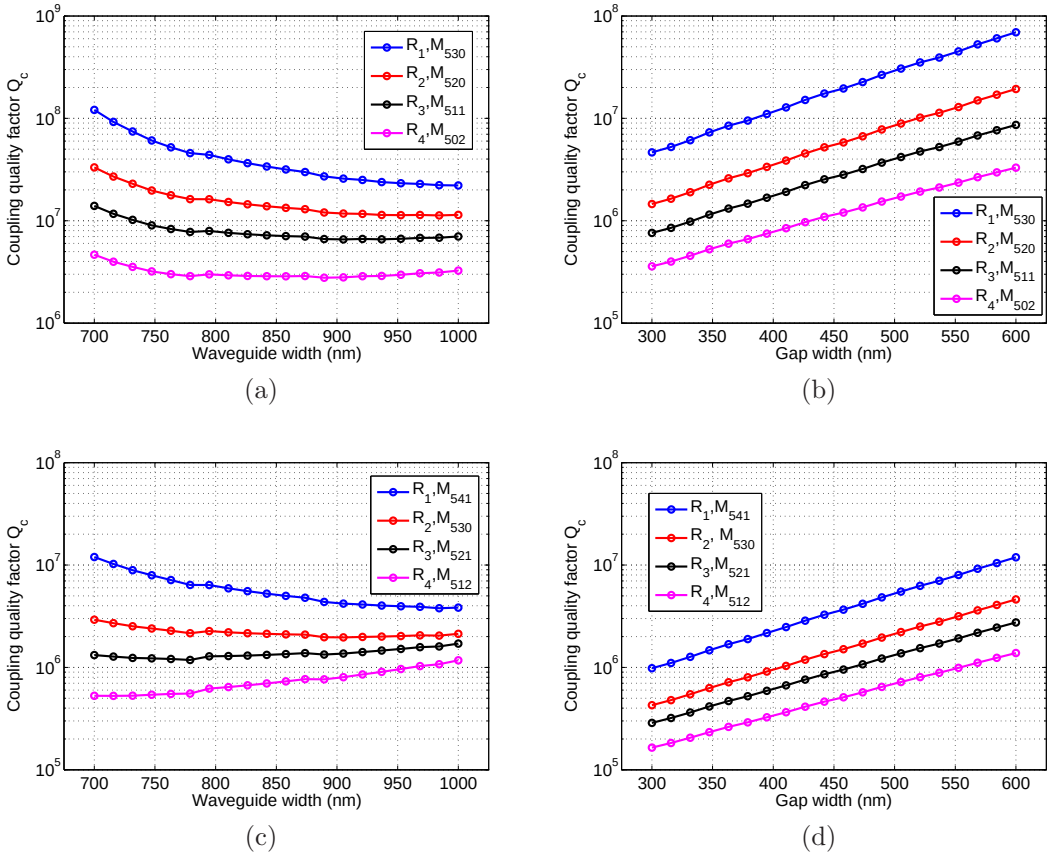

Figure 3.14: (a) The coupling quality factor Q_c for a 70 μm radius silicon nitride microdisk resonator in air as a function of the waveguide width with a fixed gap distance of 500 nm and (b) as a function of the distance between the waveguide and microdisk resonator with a fixed waveguide width of 850 nm. (c) The coupling quality factor Q_c for a 70 μm radius silicon nitride microdisk resonator in water as a function of the waveguide width with a fixed gap distance of 500 nm and (d) as a function of the distance between the waveguide and microdisk resonator with a fixed waveguide width of 850 nm.

3.14d.

The goal of these simulations is to obtain an understanding of how to engineer the resonator waveguide coupling region in order to ensure device operation in the desired coupling regime. They are to serve as a starting point for device designs and to provide a range of values for waveguide width and gap distance in which we can begin to explore the fabrication of actual devices. Of the three coupling regimes: over coupling, under coupling, and critical coupling, we are mostly interested in the under-coupled regime and the case of critical coupling. In the under-coupled regime ($Q_c > Q_0$), the intrinsic loss of the resonator dominates the waveguide coupling loss. This leads the loaded quality factor of the resonator waveguide system, as measured by the FWHM of the resonance transmission dip, to be closer to Q_0. At the critical coupling point $Q_c = Q_0$ and therefore $Q_L = 2Q_0$. In practice it is difficult to match Q_c and Q_0 due to fabrication imperfections and the large effect that small deviations in the length of the coupling gap can have on the field overlap.

Critical coupling is useful in applications such as nonlinear optics where large circulating power within the resonator is desired. Designing a device to operate at or near critical coupling requires a priori knowledge of Q_0 such that the waveguide and gap are chosen to provide a Q_c that is equivalent. A review of the literature can provide a range of realizable experimentally measured Q values as a starting point for initial designs. In the case of on-chip silicon nitride microdisk resonators, both planar and undercut of a variety of sizes, the highest Q factors reported were in the range of several million [62–64]. In interpreting the simulation results from Figures 3.14a through 3.14d it is important to compare the values of Q_c therein with values of Q_0 between 1×10^5 and 1×10^7.

When the upper cladding of the microdisk is air, the calculated coupling quality factor for the R_1 mode approaches values on the order of 1×10^6 to 1×10^7 for gap distances less than 400 nm. For higher order radial modes, the evanescent field extends further beyond the disk boundary resulting in greater coupling (lower values of Q_c) but also resulting in higher internal losses due to radiation (lower Q_{rad}), and scattering (interaction with the disk sidewalls) (lower Q_{sc}) leading to a lower Q_0. From

Figure 3.14b it is clear that for a fixed lithographically defined gap, various coupling regimes will be observed for each of the different radial order modes. Aiming to achieve critical coupling to the R_1 mode, which from Figure 3.6 has the lowest mode volume, highest effective mode index and highest Q_0, will result in the other observed higher order radial modes being in the over-coupled regime.

When the upper cladding of the microdisk is water, or an aqueous buffer solution of similar refractive index, coupling between the disk and waveguide is enhanced and Q_c decreases. Recall that the higher index upper cladding pulls the WGM and waveguide modes up slightly and reduces the decay rate of the evanescent field, thereby increasing the mode overlap in the coupling region. The phase mismatch between the modes is also reduced as the effective index of the waveguide and microdisk modes are closer in value.

The presence of the water cladding not only lowers Q_c through enhanced coupling, but, in the near infrared (NIR) wavelength regime, lowers Q_0 by adding a substantial amount of absorption loss to the resonator mode. Optical absorption in water is a key consideration for the design of a liquid phase label-free biosensing system and is discussed in more detail in Chapter 4. For an operating wavelength near 1310 nm the intrinsic Q of the water clad microdisk is dominated by absorption loss and limited to nearly 5×10^5. According to Figure 3.14d, this upper bound in the value of Q_0 necessitates as coupling gap width of less than 300 nm in order to achieve critical coupling to the R_1 microdisk mode.

These coupling simulations have uncovered a few interesting results and insights for the design and fabrication of the microdisk resonator waveguide coupling region which we will summarize below.

1. The effect of increasing the waveguide width so as to improve the coupling through better phase matching of the modes is negligible once the waveguide is more than 900 nm wide. Tuning the coupling gap width has a much stronger effect on Q_c.

2. In order to achieve critical coupling, we need to have an idea of what values

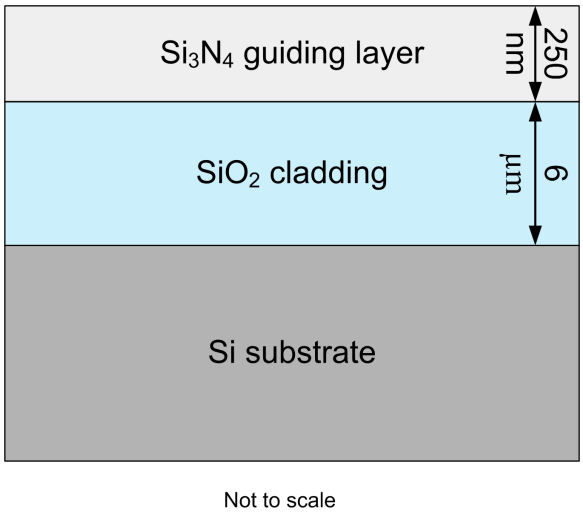

Figure 3.15: A cross section of the dielectric stack structure used to both simulate the WGM modes and fabricate the actual devices. The silicon layer serves only as the substrate to host the top two layers.

of Q_0 we are capable of achieving for a given resonator design and fabrication process.

3. For a given waveguide resonator design at NIR wavelengths, it is possible to achieve similar coupling conditions in both air and water environments due to the reduction in both Q_c and Q_0 resulting from the increase in the real and imaginary part of the upper cladding refractive index.

3.4 Experimental demonstration and results

Planar microdisk resonators with integrated waveguides were fabricated in the silicon nitride on silica platform using a combination of electron beam lithography (EBL) and dry etching. The coupling gap was lithographically tuned over a range of values determined by the simulations of Section 3.3. The transmission spectra of the microdisk resonators were measured using an optoelectronic swept frequency laser with a nominal wavelength of 1310 nm.

3.4.1 Microdisk resonator device fabrication

The wafers used for fabricating devices consisted of a silicon substrate with a thickness of nearly 500 μm with 6 μm of thermally grown oxide followed by 250 nm of low pressure chemical vapor deposition (LPCVD) silicon nitride. The wafers were custom ordered and purchased from Rogue Valley Microdevices of Medford, Oregon. A diagram of the dielectric layer structure is shown in Figure 3.15.

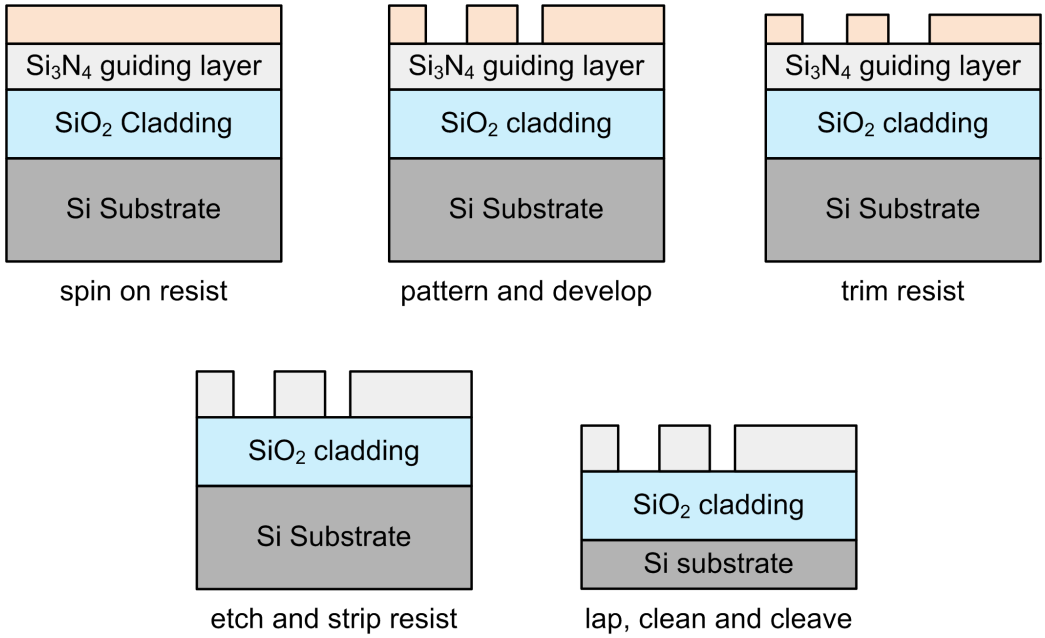

Figure 3.16: An illustration of the fabrication process for the silicon nitride microdisk resonators.

To fabricate the microdisk resonators, a positive tone e-beam resist with good dry etch selectivity, ZEP 520A, was used to write the microdisk/waveguide patterns. E-beam write parameters were optimized to reduce line-edge roughness on the resist sidewalls. An O_2 plasma resist mask trimming step was used to further reduce line-edge roughness. Pattern transfer to the nitride was accomplished via inductively coupled reactive ion etching (ICP-RIE) employing a mixed-mode SF_6/C_4F_8 gas chemistry under low pressure and at room temperature. We found these process conditions to provide highly anisotropic pattern transfer. The gas flow rates as well as RF and ICP power were optimized to suppress mask erosion and yield smooth etched sidewalls. Resist reflow prior to etching was found to have minimal effect on

the experimentally measured resonance quality factors. Etched samples were cleaned thoroughly using solvents and acid. The samples were lapped to a thickness of approximately 150 μm and waveguide facets were cleaved. The fabrication process flow is detailed in Figure 3.16.

A scanning electron microscope (SEM) was used to image the device and measure the width of the waveguides and coupling gaps. Representative SEM images are shown in Figures 3.17a through 3.17d. We found that the waveguides turned out nearly 100 nm narrower than designed and that the gaps were wider than designed by nearly 25 nm. This is most likely due to overexposure of the e-beam resist used due to the e-beam write parameters used. To combat this effect, the waveguide widths in the mask designs were positively biased by 100 nm.

3.4.2 Resonator transmission spectra: experimental results

The experimental setup shown in Figure 3.18 was used to characterize the transmission spectra of the silicon nitride microdisks. Measurement of the transmission spectrum of a high-Q optical micro-resoantor is very similar to the measurement of the transmission spectrum of the acetylene gas cell from Section 2.5.2. Differences in the implementation of the measurement related to need to couple light into and out of the on-chip waveguide. Many different methods are capable of performing this task including vertical grating couplers [65], lensed fiber edge coupling, direct coupling of cleaved fibers via on-chip v grooves [66], and free space coupling using microscope objectives. Of these techniques, free space coupling via microscope objective lenses was chosen due to its robustness to drift and the relative large working distance afforded by the objective lenses over lensed fibers (1 mm as compared to 12μm). Vertical grating couplers, which work quite well in the case of material system with high refractive index contrast, such as silicon on insulator (SOI), are difficult to implement in the silicon nitride structure used here [67].

Early iterations of the devices were fabricated with inverse taper spot size converters on the waveguide ends to improve the coupling efficiency [68]. The taper section of

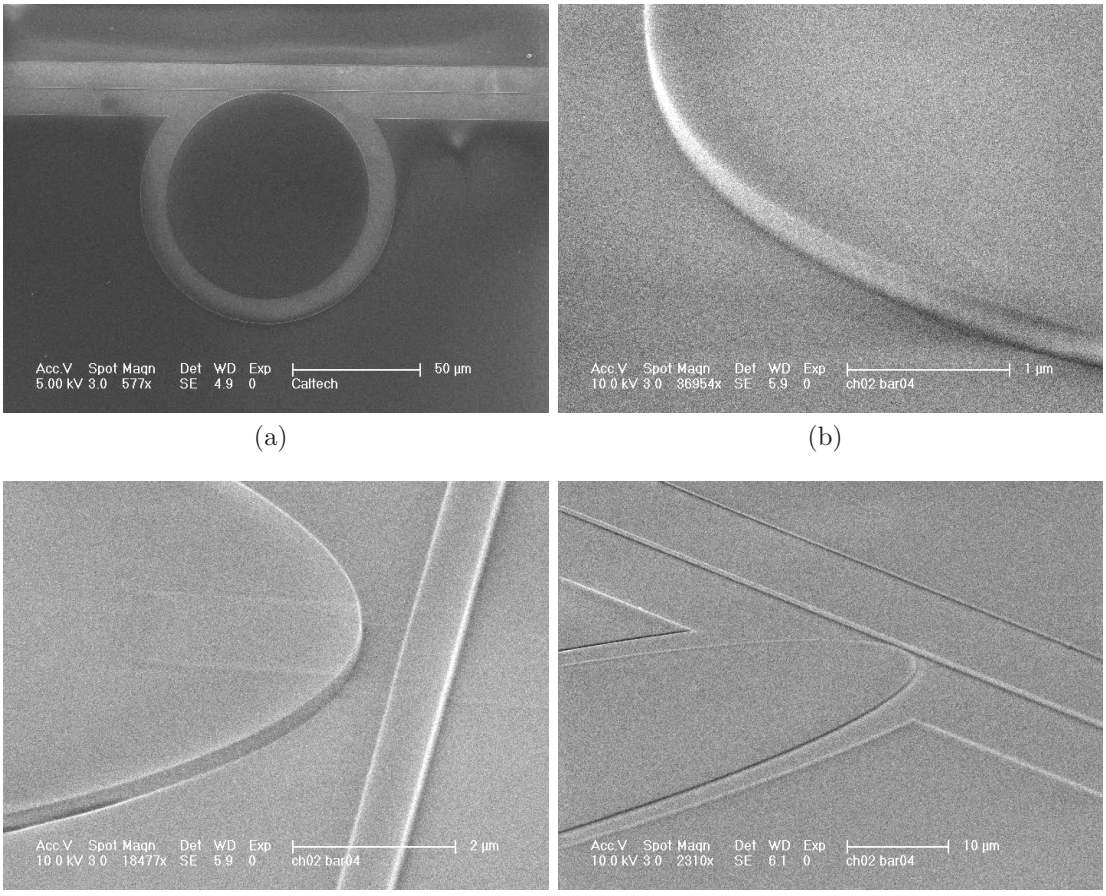

(a) (b)

(c) (d)

Figure 3.17: Scanning electron micrographs of a silicon nitride microdisk resonator. (a) An aerial view of the disk, (b) a closeup of the disk side wall showing minimal line-edge roughness, (c) a view of the coupling region, (d) a broader perspective of the device from an angled vantage point.

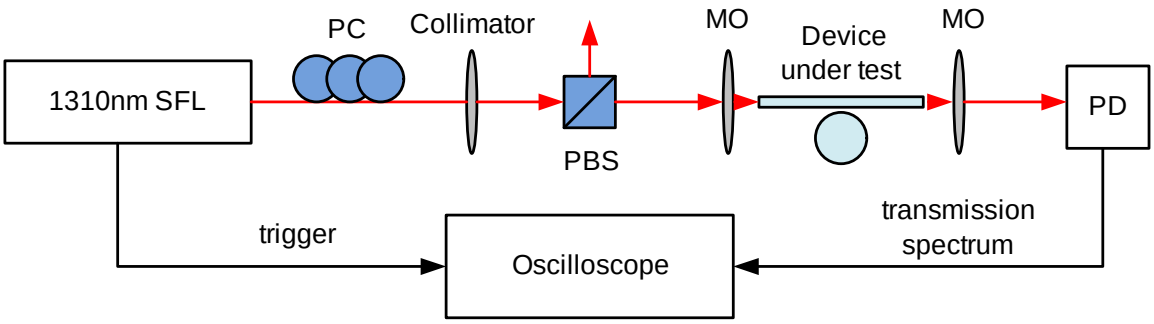

Figure 3.18: A schematic diagram of the experimental setup used to measure the transmission spectrum of a microdisk resonator. SFL, an optoelectronic swept frequency laser from Chapter 2, PC polarization controller, PBS polarizng beam splitter, MO microscope objective, PD photodiode. The optical path is shown in red and is in optical fiber up until the collimator.

the spot size converters was 300 μm long in which the waveguide transitioned from its full width to a width of 180 nm. Devices with inverse tapers underwent an additional deposition of PECVD silica to act as a cladding for the narrow waveguide region. A window in the oxide layer was then etched back such that the disks would operate with an air cladding. Eventually, spot size converters were dropped from microdisk resonator and sensor chip fabrication due to the additional fabrication steps and lack of necessity.

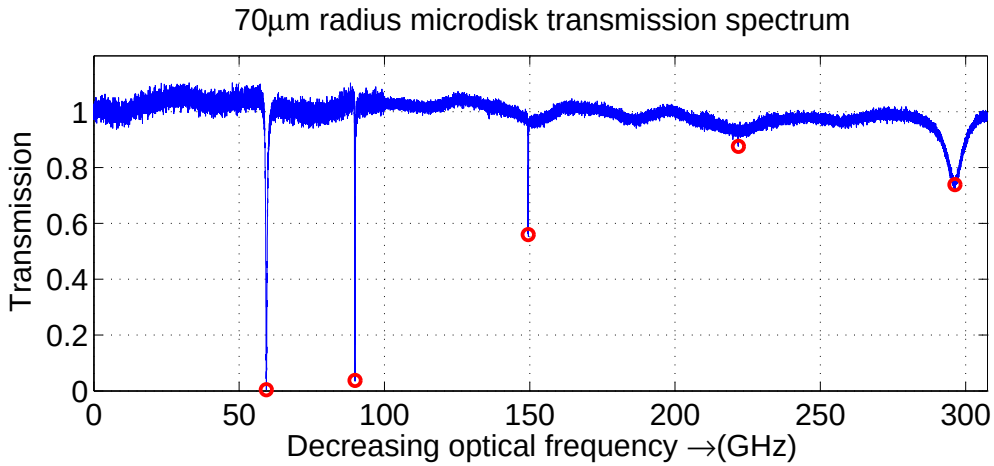

Figure 3.19: The transmission spectrum of a silicon nitride microdisk resonator. Whispering gallery modes with radial mode numbers between 1 and 5 are present in various coupling scenarios.

The 1310 nm SFL detailed in Chapter 2 was used to interrogate the transmission

spectrum of the microdisk resonators. The frequency sweeps used in the measurements had a chirp rate of 1×10^{14} Hz/sec and a duration of 1 ms for a total chirp bandwidth of 100 GHz. A trigger signal generated by the laser control electronics at the beginning of each frequency sweep was used to trigger the oscilloscope to ensure that the measured photodiode signal was captured correctly.

A representative transmission spectrum of a silicon nitride microdisk resonator is shown in Figure 3.19. This spectrum is more than 300 GHz wide and was obtained by changing the temperature set point of the SFL to coarsely tune the absolute wavelength of the sweep. Four overlapping spectral measurements were captured using different temperature set points and were stitched together using the various resonance features as landmarks. The device had a waveguide width of approximately 850 nm and a gap width of nearly 575 nm. The wide coupling gap width was chosen for several reasons. By choosing to operate in the severely undercoupled regime, the measured loaded Q factor is very close to the intrinsic Q therefore high values for the loaded Q can be measured. Operating in the severely undercoupled regime for the R_1 mode also allows for undercoupling to the higher radial order modes. Therefore a determination of the modes can be made more easily based on the measured loaded Q and the extinction ratio. In Figure 3.19 the radial order of the modes shown from left to right are R_4, R_3, R_2, R_1, and R_5.

To better characterize the transmission spectra of the microdisk whispering gallery modes, detailed views of the transmission spectra of the modes were also captured. Performing detailed or zoomed-in measurements of fine spectral features is extremely simple using the SFL setup. The resolution of the horizontal (time / frequency) axis of the oscilloscope is simply increased, or alternatively, the number of points captured from the oscilloscopes memory can be increased. The sweep repetition rate of the SFL is 500 Hz so such changes are observed seemingly instantaneously. The measured transmission was normalized to the baseline (off resonance value) and a Lorentzian function was fit to the experimental data based on the theoretical transmission spectrum of a traveling wave resonator given by Equation 3.36. Transmission spectra for individual resonances are shown in Figures 3.20a through 3.20d. These

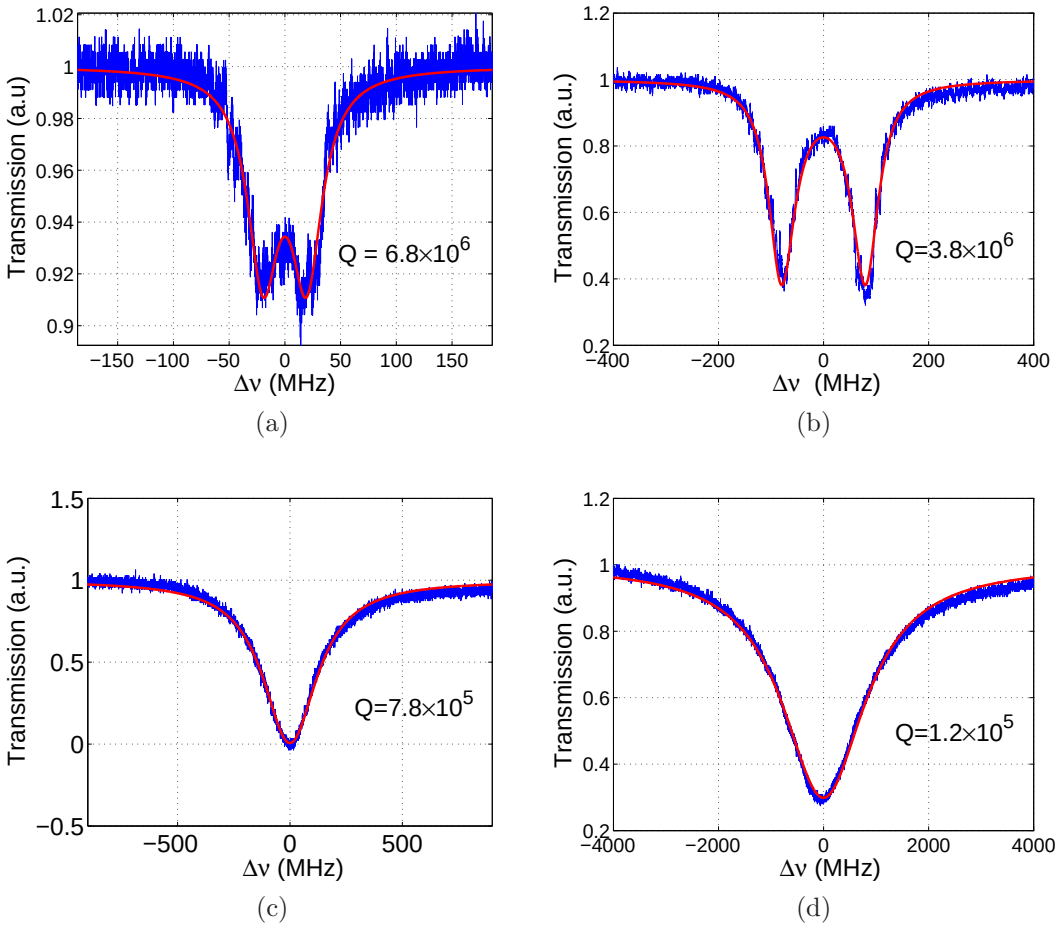

Figure 3.20: Experimentally measured transmission spectra from a representative silicon nitride microdisk resonator. (a) R_1 mode under-coupled, (b)R_2 mode under-coupled, (c) R_3 mode near critical coupling, and (d)R_4 mode over-coupled. Blue traces are experimental data. Red traces are lorentzian or doublet lorentzian curve fits.

spectral measurements were performed at low optical input power to avoid thermal nonlinear effects within the disk, which can corrupt the measurement [59, 69]. For increasing frequency sweeps at high power, thermal nonlinearities can artificially narrow the measured resonance linewidth [70, 71]. Similarly, for decreasing frequency sweeps at high input power, the measured resonance linewidth is broadened and takes on the familiar bistable "shark fin" shape [59, 72]. All transmission spectral measurements were performed using decreasing frequency sweeps at power levels such that no thermal nonlinearity was observed.

The transmission spectra in Figures 3.20a and 3.20b clearly show splitting of the degeneracy between the clockwise and counter-clockwise propagating modes for the ultra high-Q R_1 and R_2 modes of the microdisk resonator. To our knowledge the Q factors measured here are the highest reported Q factors, loaded or intrinsic, for integrated planar silicon nitride microdisk resonators of this size. Other ultra high Q ($\approx 10^7$) silicon nitride /oxide ring resonators have been reported with radii on the order of several millimeters [73].

Chapter 4

Liquid phase sensing with silicon nitride (Si_3N_4) microdisk resonators

Label-free optical biosensing attempts to address the need for systems capable of detecting and analyzing the interactions of biomolecules at ultra low concentrations. The large refractive index sensitivity and narrow linewidth of high-Q optical resonators make them an attractive transducer for such a label-free sensing system. A multitude of high-Q optical resonators with various geometries, materials, Q factors, and other attributes have been used for refractive index sensing as part of label-free sensing systems. Much of the work in this area has been focused on two parallel tracks: extreme performance, or robust systems of lower sensitivity. The performance oriented approach to label-free sensing has fixated on single molecule detection with free standing WGM resonators with Qs in the $10^7 - 10^8$ range. The coupling of light into and out of these resonators is a delicate affair typically involving fragile tapered optical fibers. The more practical camp has leveraged the relative maturity of silicon photonics to fabricate integrated planar ring or disk resonators on SOI with modest Q factors in the mid 10^4 range. Silicon has proved to be wonderful material for integrated optics, however its absorption spectrum places a constraint on the wavelength of any potential biosensing system that runs counter to the wavelength constraint of water, the host medium for biomolecules.

In this chapter, we explore the development of a label-free biosensing system that is built around the high-Q planar integrated silicon nitride microdisk resonators

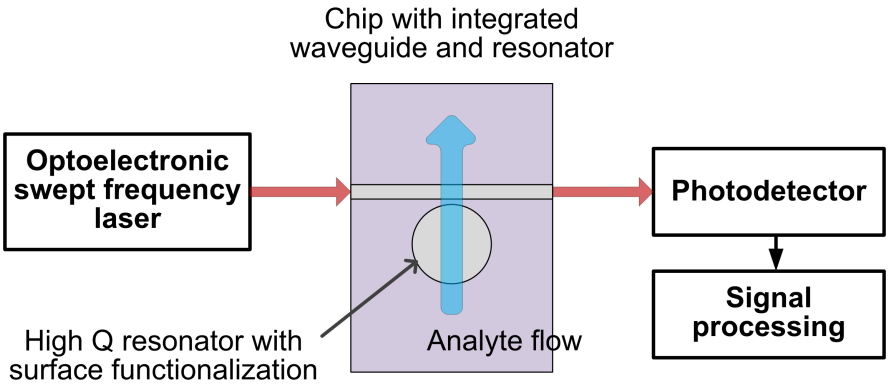

Figure 4.1: A schematic diagram of the microdisk resonator-based sensing system. The resonant frequency of the microdisk is measured repeatedly while an analyte solution is flown over its surface.

presented in Chapter 3 and the optoelectronic swept frequency laser presented in Chapter 2. The integration of planar high-Q optical resonators on chip, and the development of reliable and relatively low cost laser measurement systems are important advances in the realization of practical label-free biosensing systems.

We present theoretical foundations of optical resonator based refractive index sensing and numerical simulations of the bulk refractive index response of the silicon nitride microdisk resonator. We discuss the importance of the wavelength of operation for the sensing system, highlighting the advantages of silicon nitride for short wavelength operation. Details of the design, fabrication, and integration of microfluidic channels for the precise and controlled delivery of analyte solutions are given. We experimentally demonstrate the bulk refractive index response of several microdisk modes and determine the sensitivity of the disk as a transducer. Finally, we experimentally demonstrate the use of the microdisk sensor to measure both the non-specific and specific adsorption of biomolecules.

4.1 Refractive index sensing

Chapter 3 discussed in detail the physics of the microdisk resonator. In that discussion, emphasis was placed on engineering the resonator waveguide coupling and on the fabrication and experimental demonstration of ultra-high quality factor resonators

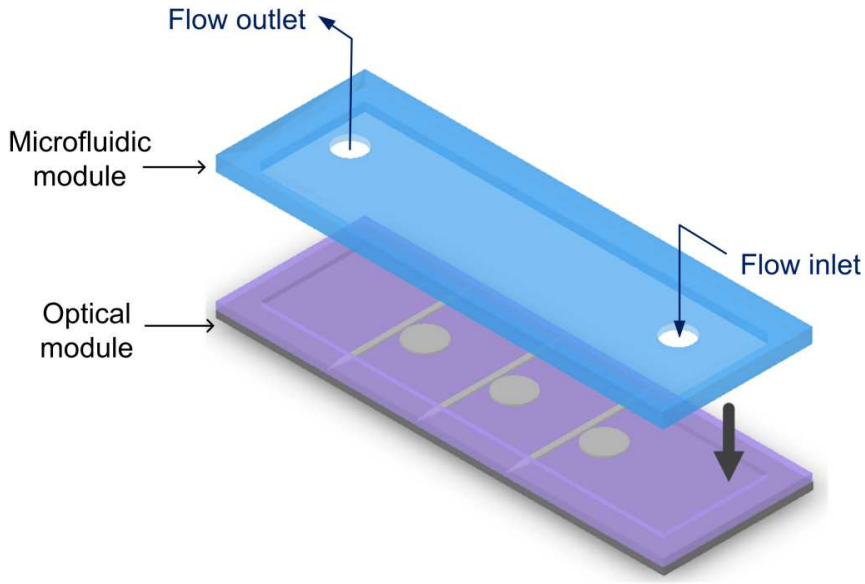

(a)

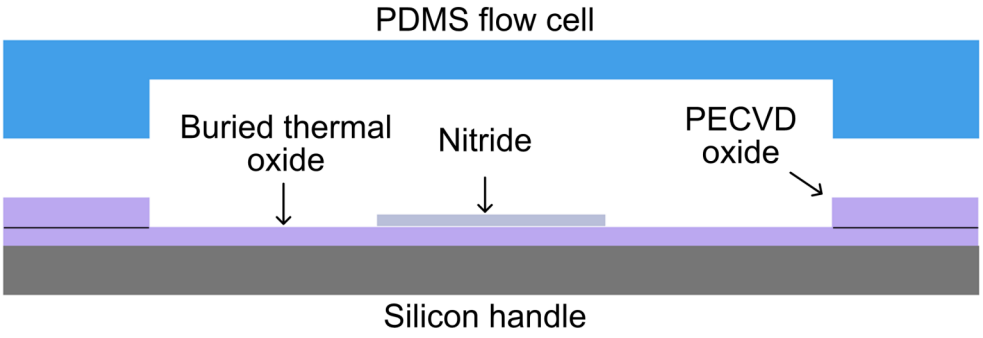

(b)

Figure 4.2: (a) A mock up of the label-free sensing device showing both the PDMS microfluidic module and the optical module with multiple microdisk resonators. (b) A cross sectional view of the sensing device from (a) denoting the various layers in the device structure. The depictions are not to scale.

in the silicon nitride on silica material platform. Here, we build on those concepts and results, employing the planar integrated silicon nitride microdisk resonator as a refractive index transducer to make sensitive measurements of the refractive index of the upper cladding material of the resonator.

4.1.1 Refractive index sensing theory

Light confined to the whispering gallery modes of a microdisk resonator must satisfy the self consistent periodic resonance condition. That is, the frequency of the propagating wave must complete an integer number of cycles in one complete circumnavigation of the disk.

$$2\pi R n_{eff} = m\frac{c}{f_{res}} = m\lambda_{res}, \tag{4.1}$$

where R is the radius of the microdisk, n_{eff} is the effective refractive index of the resonant optical mode, f_{res} is the resonant frequency, c is the speed of light, and m is the azimuthal mode number. The sensing action can be understood by looking at small changes in the effective index of the mode Δn_{eff} and the corresponding change in the resonant frequency or wavelength Δf or $\Delta\lambda$. The effective index of the resonant mode is a function of the refractive indicies of its constituent materials , i.e., $n_{eff} = n_{eff}\left(n_{core}, n_{upper}, n_{lower}\right)$ and the resonator geometry. In the case of a change in the bulk refractive index of the upper cladding of the resonator we can write

$$\frac{\partial\lambda_{res}}{\partial n_{upper}} = \frac{2\pi R}{m}\left(\frac{\partial n_{eff}}{\partial n_{upper}}\right). \tag{4.2}$$

For a given change in the bulk upper cladding index Δn_{upper}, the resulting change in the resonant wavelength is given by

$$\Delta\lambda_{res} = \frac{2\pi R}{m}\left(\frac{\partial n_{eff}}{\partial n_{upper}}\right)\Delta n_{upper}. \tag{4.3}$$

Some reports on high-Q resonator sensing in the literature [5, 6] take

$$\frac{\partial n_{eff}}{\partial n_{upper}} = \Gamma_{upper}. \tag{4.4}$$

This yields

$$\Delta\lambda_{res} = \frac{2\pi R}{m}\Gamma_{upper}\Delta n_{upper}. \tag{4.5}$$

Strictly speaking, the effective index of the mode is defined as $n_{eff} = \beta_{res}\lambda_0/(2\pi)$ where the propagation constant β_{res} is determined by solving the eigenvalue equation for a specific dielectric resonator structure. Therefore, we choose to leave the bulk refractive index response in the form of Equation 4.3.

The driving element of bulk refractive index sensing, and of sensing in general, is the interaction of particles or molecules, representing a Δn, with the evanescent field of the microdisk mode. The evanescent field decays exponentially away from the disk meaning that the most sensitive portion of the active sensing area is that closest to the disk surface. In light of this, others [5, 6] have defined another confinement factor Γ_{sense} to cover the fraction of the mode field in this area and a similar version of Equation 4.5 can be written for the the sensing area. This interpretation can be used to describe the deposition of thin films onto the surface of the resonator and thereby determine the mass response in Hz/gram.

4.1.2 Bulk refractive index sensing simulations

A rigorous calculation of the bulk refractive index response of the resonator can be determined from FEM simulations of the whispering gallery modes. Modeling the same silicon nitride microdisk resonator as in Chapter 3, we solved for the eigenfrequency of resonant modes with a nominal wavelength of 1310 nm as the upper cladding refractive index was varied from 1.33 to 1.335. The results are shown in Figures 4.3a, 4.3b, and 4.3c. The values of $\Delta\lambda/\Delta n$ taken from a linear fit to the slope are 94.83nm/RIU, 95.05nm/RIU, and 95.57nm/RIU for the R_1, R_2, and R_3 modes respectively. This corresponds to a frequency responsivity of -16.9 THz/RIU. For

the R_1, M_{541} mode, the approximate bulk responsivity calculated from Equation 4.5 is found to be 77 nm/RIU which is not in very good agreement with the value calculated from the numerical simulations. The difference is due to the approximations made to obtain Equation 4.5.

4.1.3 Wavelength of operation

The wavelength of operation for a resonator based sensor in a aqueous environment is of critical importance to the achievement of high optical quality factors. High-Q narrow linewidth resonances allow for the resolution of smaller changes in the resonant frequency. Recall from Chapter 3 that the intrinsic quality factor of the resonator mode is composed of many parallel loss channels and can be written as

$$\frac{1}{Q_0} = \frac{1}{Q_{rad}} + \frac{1}{Q_{sc}} + \frac{1}{Q_{abs,core}} + \frac{1}{Q_{abs,clad}}, \tag{4.6}$$

where Q_{rad} describes the power dissipated in the resonator due to radiation losses, Q_{sc} describes the power lost in the resonator due to surface scattering losses, $Q_{abs,core}$ describes the power lost in the resonator due to material absorption in the core region, and $Q_{abs,clad}$ describes the dissipated power due to material absorption in the cladding region. The parallel addition of Q factors carries the implication that the overall intrinsic Q_0 of the resonator is dominated by the largest loss mechanism for the system. In the case of the air clad resonators demonstrated in Chapter 3, the dominant loss mechanisms are scattering losses due to surface roughness of the resonator and absorption losses of the silicon nitride core material. For a microdisk resonator with a water or aqueous buffer upper cladding, material absorption losses play a large role in the determination of Q_0 and strongly depend on the wavelength of the mode under consideration.

The optical properties of liquid water have been well documented and sources for the values of the complex refractive index water at 25°C are available in the literature [1]. Values for the extinction coefficient k of water at various wavelengths of interest for biosensing are listed in Table 4.1. The full absorption spectrum of water

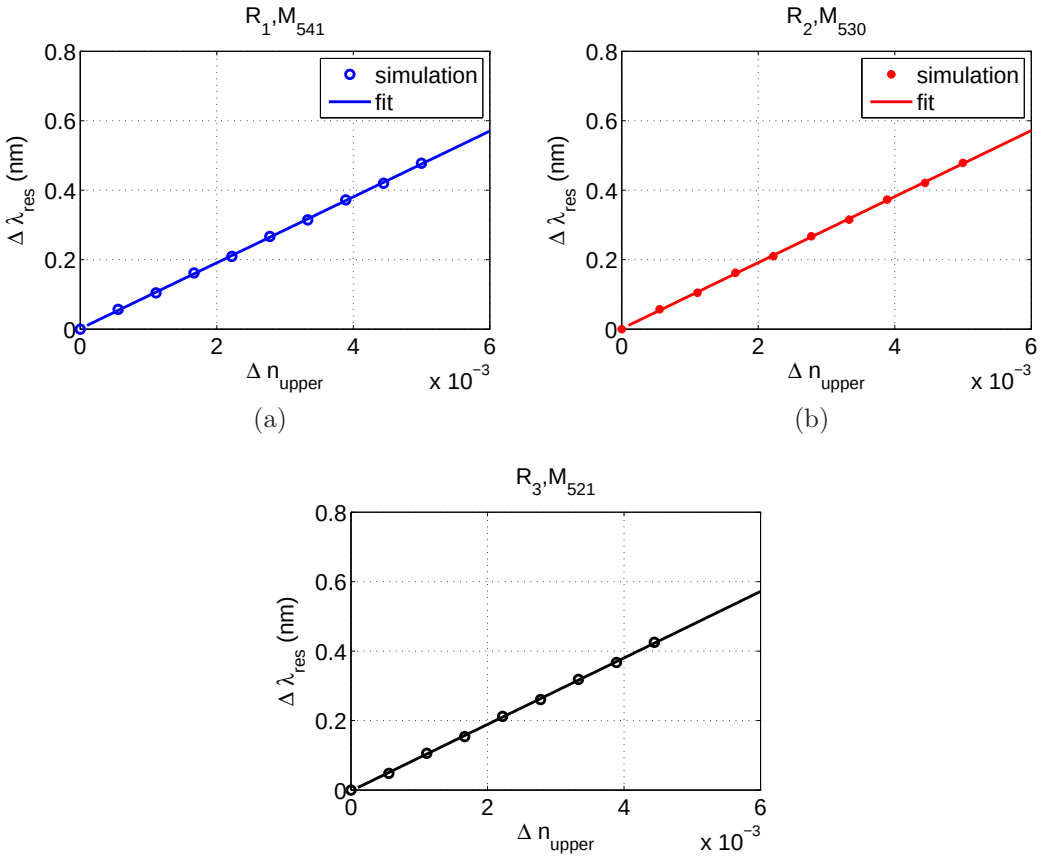

Figure 4.3: The results of FEM simulations of 70 μm radius silicon nitride microdisk resonators. The bulk refractive index of the upper cladding material is varied from 1.33 to 1.335 and plotted against the resulting resonant wavelength found from simulation. (a) The R_1, M_{541} mode, (b) the R_2, M_{530} mode, (c) the R_3, M_{521} mode. Lines are linear fits to the simulation results to determine the bulk refractive index responsivity in nm/RIU.

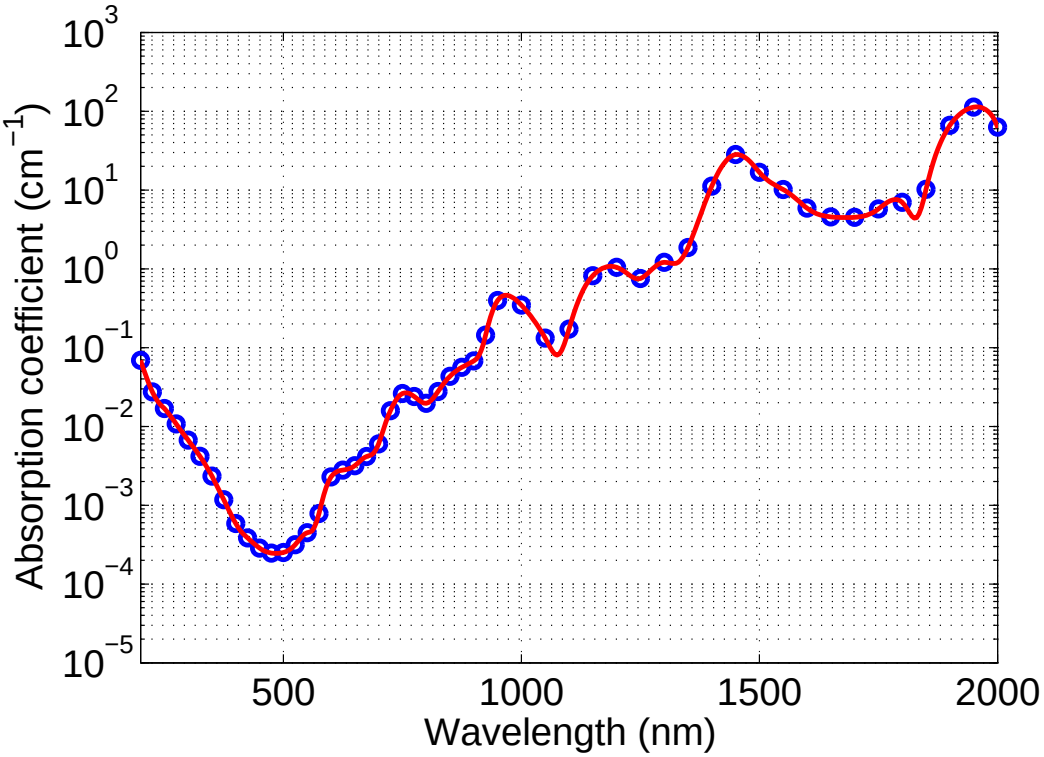

Figure 4.4: The absorption coefficient per unit length in cm^{-1} of liquid water at 25°C over the 200 nm to 2μm wavelength region from [1]. Values from the paper are blue circles. Red line is a cubic spline interpolation of the data.

is shown in Figure 4.4. The visible portion of the spectrum occupies the large dip in absorption values between 400 nm and 700 nm. The linear absorption coefficient α is derived from k using the well known relationship [47]

$$\alpha = \frac{4\pi k\,(\lambda)}{\lambda}. \tag{4.7}$$

To determine the $Q_{abs,clad}$ we use the relationship

$$\frac{1}{Q_{abs}} = \frac{2\alpha_{r,m}}{\beta_{r,m}}, \tag{4.8}$$

which follows from the definition of the Q factor in that it represents the energy lost per optical cycle due to absorption. However, as the majority of the resonant mode does not overlap with the lossy upper cladding material, it is necessary to modify Equation 4.8 to include only the portion of the energy that does. The appropriate modification is given by the confinement factor of the mode in the upper cladding Γ_{upper} [74]. We therefore have the expression for $Q_{abs,clad}$

$$\frac{1}{Q_{abs,clad}} = \frac{2\alpha_{r,m}}{\beta_{r,m}}\Gamma_{upper}. \tag{4.9}$$

Calculations of $Q_{abs,clad}$ were performed using values of the extinction coefficient from [1] and values of Γ_{upper} as determined from FEM simulations of the appropriate microdisk resonant modes. The results are given in Table 4.1. The confinement of the mode in the upper cladding, (water), is low. At 850 nm, 1060 nm, and 1310 nm Γ_{upper}

λ (nm)	Extinction k	Absorption α cm^{-1}	Q_{abs}
625	1.39×10^{-8}	0.0028	5×10^{8}
850	2.93×10^{-7}	0.0433	4.65×10^{7}
1060	1.1×10^{-6}	0.1304	8.77×10^{6}
1310	1.25×10^{-5}	1.199	5.6×10^{5}
1550	1.25×10^{-4}	10.13	5.8×10^{4}

Table 4.1: Values of the extinction coefficient, absorption coefficient, and corresponding Q_{abs} for liquid water at 25°C at several wavelengths of interest.

was found to be 0.0488, 0.0689, and 0.0948 respectively. Though small, this fractional overlap of the mode with water dramatically impacts $Q_{abs,clad}$ at longer wavelengths. In these cases water absorption loss becomes the limiting factor in determining Q_0 for the resonator. From these calculations, it is clear that in order to construct a high-Q optical resonator-based label-free biosensing system that operates in an aqueous environment, shorter wavelength light should be used in the measurement. It is precisely this rationale that drove the decision to develop optoelectronic swept frequency laser sources at 1310 nm, 1064 nm, and 850 nm.

The desire to use shorter optical wavelengths in turn impacted the decision to use the silicon nitride on silica material system to construct the resonators. Much attention in the field of label-free optical biosensing has been placed on the use of silicon on insulator (SOI) devices due to the maturity of the material and its processing techniques. Unfortunately, silicon exhibits strong absorption at wavelengths below 1100 nm — due to its relatively low bandgap energy (1.12 eV) — and is unsuitable for the fabrication of high Q resonators at shorter wavelengths. Both silicon nitride and silica exhibit good optical transparency over all wavelengths of interest. Additionally, silicon nitride has a relatively high refractive index of two, allowing for small device footprints and good field confinement in both wave guiding and resonant structures.

Knowledge of the water absorption quality factor aids in designing the coupling between the microdisk resonator and bus waveguide. In order to achieve critical or under coupling, we require $Q_0 = Q_c$. At the wavelengths of 1310 nm or 1550 nm, where the intrinsic Q of the resonator is dominated by water absorption losses such that $Q_0 \approx Q_{abs,clad}$, we can use the values of Q_{abs} from Table 4.1 to inform the design of the coupling region.

4.2 Microfluidic integration

The realization of a small form factor, low cost, robust high-Q optical biosensing system requires careful integration of the resonator and the analyte delivery system. The microscale dimensions of the planar waveguide and resonator pair are a natural

match with microfluidic flow delivery.

For the high-Q microresonator device to become an effective analytical tool, it must consume as little analyte as possible in the course of making a measurement. Additionally, its use in biomolecular assays or affinity measurements requires that it be made from hydrophilic and bio-inert materials. We fabricated microfluidic devices made from polydimerhylsiloxane (PDMS), a two stage curable elastomer, to deliver fluids to the surface of the silicon nitride microdisk resonators.

The aim of the microfluidic devices used here is only simple fluid delivery. The design of the microfluidic channels used requires only a single mold and a single layer PDMS structure.

An image of the photomask used for creating the molds of the microdluidic devices is shown in Figure 4.5. Early microfluidic modules consisted of a single channel oriented perpendicularly to the waveguides as depicted in Figure 4.2a. During flow experiments all of the microdisk resonators on a chip would be exposed to the analyte solution simultaneously. The current experimental setup shown in Figure 4.1 is only capable of measuring the transmission spectrum of a single resonator at a time. In the interest of conserving a precious resource, the high-Q resonators, the microfluidic device design was updated to have an individual flow channel for each resonator with flow parallel to the waveguide as shown in figure 4.5.

Using standard photolithographic techniques, we fabricated molds for the microfluidic devices from SU-8 2010 negative tone photoresist on bare 3 inch silicon

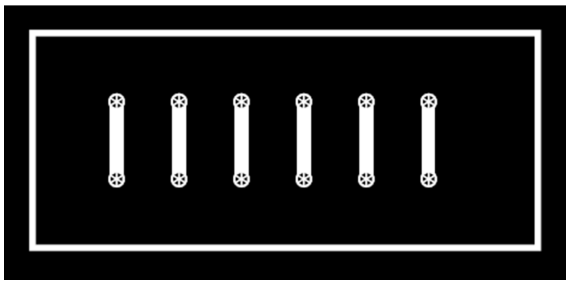

Figure 4.5: An image of the mask pattern used in fabricating the PDMS microfluidic device molds. The dimensions of the microfluidic module were approximately 5 mm $\times$ 9 mm. The image shown is not actual size.

wafers. The following procedure was used:

1. Clean 3 inch Si wafer with solvent and blow dry.
2. Spin coat wafer with Su-8 2010 for 1.5 minutes at 3500 rpm to achieve 10 μm film thickness.
3. Soft bake resist coated wafers at 95°C for 3 minutes.
4. Expose to UV radiation with mask aligner for 95 seconds.
5. Bake for 2.5 minutes at 95°C.
6. Develop in Su-8 developer for 3 min with agitation.
7. Hard bake for 6 minutes at 150°C to cure mold and fix imperfections.

PDMS microfluidic devices were then cast using the Su-8 molds. The following procedure was used:

1. Vapor deposit clorotrimethylsilane (CTMS) onto silicon mold to prevent permanent adhesion of PDMS to wafer.
2. Prepare Sylgard 184 (Dow Corning) PDMS two part solution in teflon mixing container in 10:1 ratio of part A : B. Mix using mixer / degasser at 1 min : 5 min mixing to degassing time.
3. Pour mixed PDMS over mold in plastic petri dish.
4. Place mold with PDMS in vacuum chamber and degass until no bubbles are visible .
5. Bake at 80°C overnight.

Fresh PDMS contains uncrosslinked polymer chains that may migrate within the bulk material and can diffuse into microfluidic channels causing contamination of resonator devices. To avoid this, finished PDMS devices were immersed in toluene

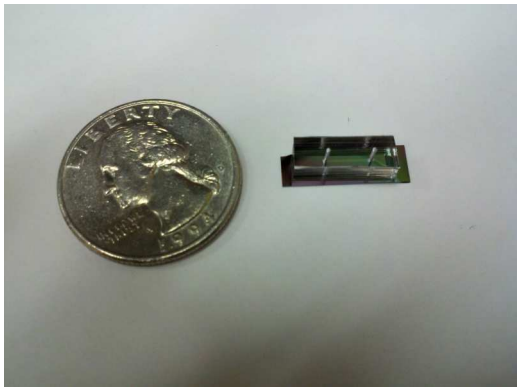

Figure 4.6: A photograph of a finished high Q silicon nitride microdisk resonator sensor with PDMS microfluidic channel for analyte delivery.

for 1 day followed by acetone for 1 day and water for 1 day. These solvent immersions swell the PDMS and allow the uncrosslinked oligomers to diffuse out. The resulting PDMS is cleaner and easier to permanently bond to the optical module [75].

Permanent bonding of the PDMS microfluidic devices to resonator chips was accomplished by treating both modules with oxygen plasma. Prior to the plasma treatment, the PDMS devices were sonicated in isopropanol for 5 minutes to remove particles and surface contaminants that may have accumulated during storage. The resonator chips were solvent cleaned and blown dry with dry nitrogen in a clean room environment. The resonator chips were treated with a 50 W oxygen plasma for 2 minutes alone and then together with the microfluidic devices for an additional minute. The resonators and microfluidic channels were then aligned using a custom setup and pressed into contact. The finished devices were baked overnight at 80°C. A photograph of a representative high-Q resonator sensing device is shown in Figure 4.6.

Fabrication of early devices included a 2μm thick PECVD oxide layer deposited over the resonator chip to serve as both an upper cladding for inverse taper spot size converters and as an adhesion layer for the permanent bonding of the PDMS microfluidic channels. A trench in the PECVD oxide layer was then etched back to expose the resonator surfaces. It was later determined that the PECVD oxide layer was neither necessary for PDMS bonding nor were spot size converters necessary for input/output coupling. These additional fabrication steps were dropped and the

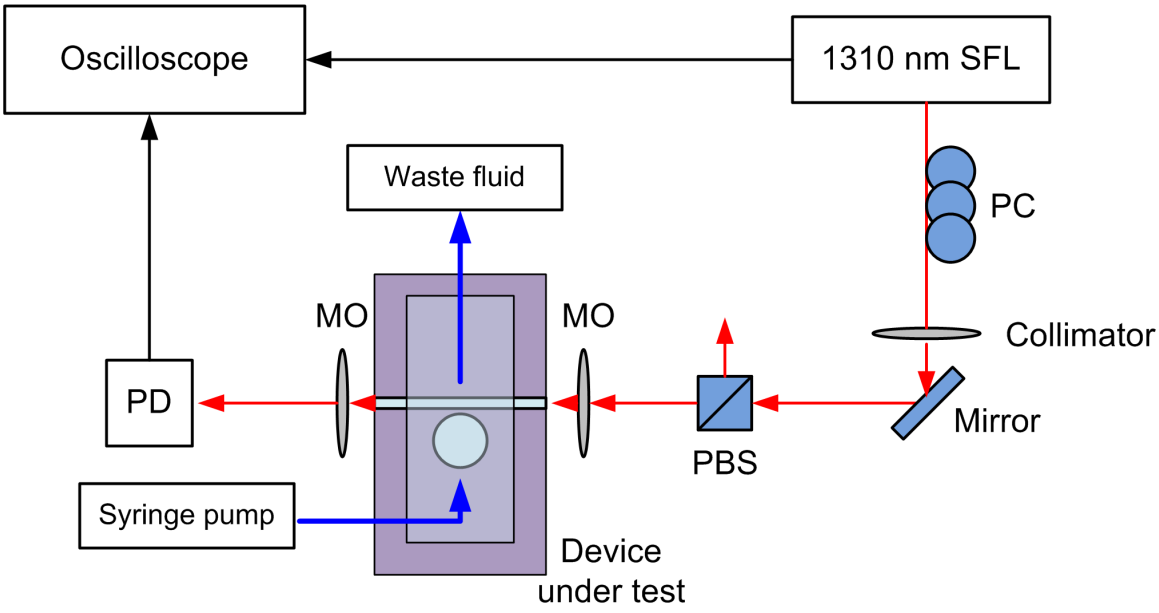

Figure 4.7: A schematic diagram of the experimental setup used to measure the transmission spectra of integrated silicon nitride microdisk resonators subjected to fluid flow via the bonded microfluidic channel.

microfluidic devices were bonded directly to the silicon nitride chip surface.

4.3 Experimental results

We now present the results of experimental measurements on the silicon nitride resonators operating in a liquid environment. We demonstrate a reduction of the loaded quality factor of the resonances from the air clad values as predicted in Section 4.1.3. We also perform dynamic sensing measurements to determine the bulk refractive index response of the resonators. Nonspecific adsorption of the protein bovine serum albumin (BSA) is reported. Finally we demonstrate specific sensing of streptavadin with biotin using microdisk resonators.

4.3.1 Microdisk resonators in water

The measurement system shown in Figure 4.7 was used to observe the transmission spectrum of the resonator during water immersion. The use of the syringe pump enabled precise control of the flow rate, duration, and volume of fluid introduced to

the resonator. The impact of the water cladding on the measured Q factors of the microdisk resonator devices was nearly immediate.

Figures 4.8a through 4.8d show detailed transmission spectra for each of the four resonant modes in the aqueous environment. The resonator used in these measurements is the same as was used in the air upper cladding measurements from Figures 3.20a through 3.20d. The effect of increased optical absorption losses on the loaded Q of the resonator due to the water cladding is readily apparent. As expected, in the aqueous environment, optical absorption is the dominant loss channel. The loaded quality factors obtained from the measurements are all in the mid 10^5 regime. We note good agreement between these values and the water absorption limited quality factor $Q_{abs,upper}$ at a wavelength of 1310 nm, as given in Table 4.1, of 5.6×10^5.

To further illustrate the importance of shorter optical wavelengths in maximizing the loaded wet Q of a WGM resonator, we measured the transmission spectra of a silica microtoroid resonator in water with a swept frequency laser operating at 1539 nm and at 1310 nm. Silica microtoroid resonators can easily be fabricated with ultra high quality factors owing to their very smooth side walls [12, 43]. They were used in exploratory measurements investigating the use of SFLs for optical biosensing at the outset of this work. The results are shown in Figures 4.9a, 4.9b, and 4.9c. The quality factors as extracted from Lorentzian fits to the data are 2.2×10^4 in water at 1539 nm, and 3.5×10^5 in water at 1310 nm. These values should be compared with the dry loaded Q for the device measured of 3×10^7. These values for the wet Q are in good agreement with the expected values for these wavelengths from Table 4.1. It should be noted that the silicon nitride microdisk resonators and waveguides do not support guided modes at 1539 nm and therefore could not be used for these measurements.

4.3.2 Bulk refractive index sensing

We investigated the response of the silicon nitride microdisk resonators to changes in the bulk refractive index of the aqueous upper cladding. Measurements were per-

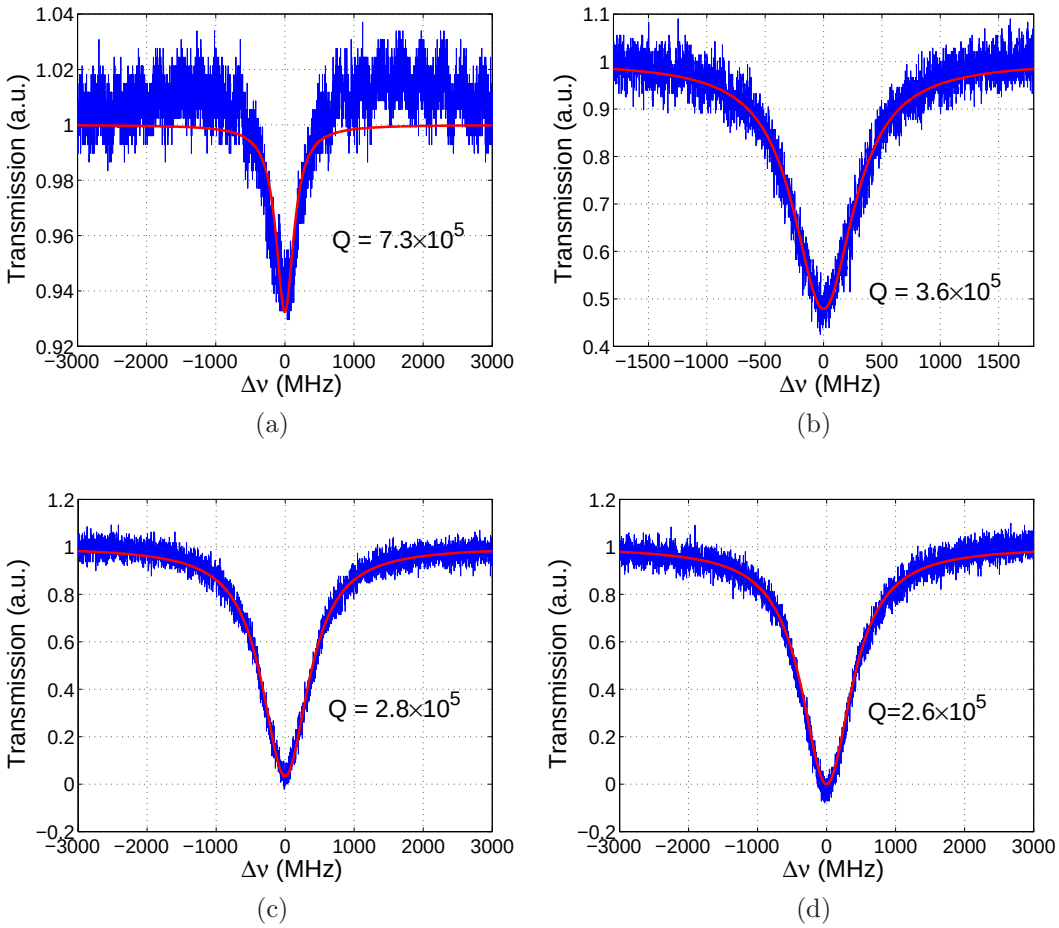

Figure 4.8: Experimentally measured transmission spectra of selected modes of a silicon nitride microdisk resonator with a water upper cladding. Blue curves are the measured data, red curves are Lorentzian fits. The loaded quality factors extracted from the Lorentzian fits are noted in each case. (a) R_1 mode (b) R_2 mode (c) R_3 mode (d) R_4 mode.

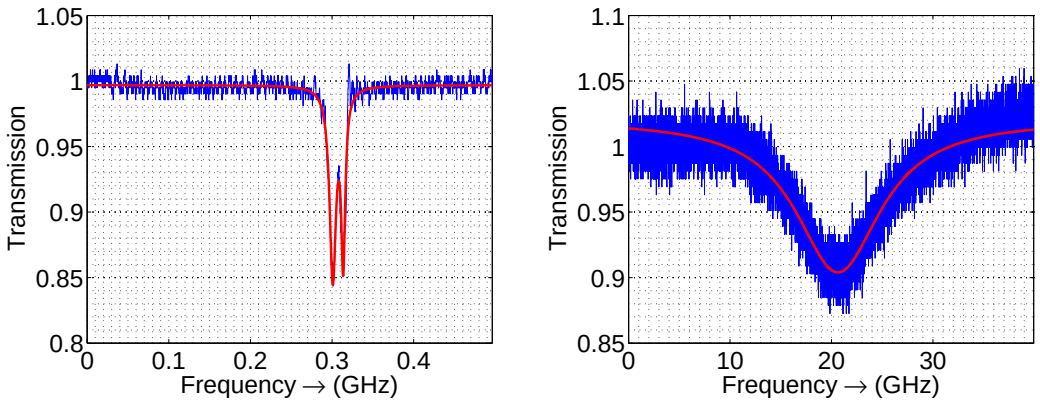

(a)

(b)

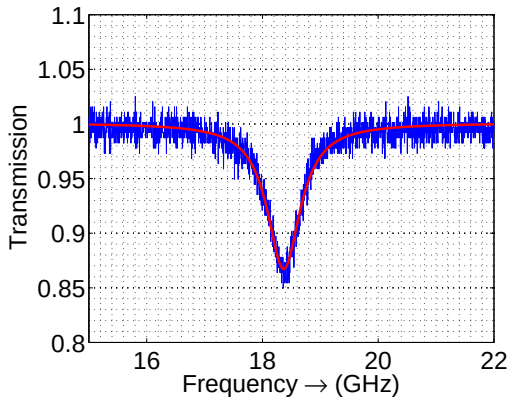

(c)

Figure 4.9: Experimentally measured transmission spectra of a resonant mode of a silica microtoroid in (a) air at 1539 nm, (b) water at 1539 nm, and (c) water at 1310 nm. The blue traces are the measured data, red traces are Lorentzian fits.

formed in three steps for a given bulk refractive index change.

1. DI water was flown through the microfluidic channel over the microdisk resonator to obtain a baseline position for the resonant frequency of the mode under observation.

2. The solution under flow was changed from water to a NaCl solution with a known concentration of salt. Flow and measurements continued until the resonance shift saturated.

3. The solution under flow was changed back to the baseline DI water solution and continued until the resonance had returned to its initial position.

Solutions consisting of various concentrations of NaCl dissolved in deionized water were used to vary the refractive index of the bulk upper cladding of the resonators. The refractive index of saline solution as a function of salinity, temperature, and wavelength is well known and excellent empirical models exist [76]. We used solutions with 1/32%, 1/16%, 1/8%, 1/4%, 1/2%, and 1% NaCl by weight prepared by sequential dilution from a stock 1% solution. A control experiment in which the saline soultion flow step was replaced by DI water was also performed in order to judge system characteristics. A slightly modified version of the experimental setup shown in Figure 4.7 was used to perform bulk refractive index sensing experiments on the silicon nitride microdisk resonators. A three way solenoid valve controlled via computer was used to select the solutions flowing into the microfluidic channel. A bank of computer controlled syringe pumps was used to drive fluid flow.

Dynamic response curves showing the real time response of the R_2 mode resonant frequency are shown in Figure 4.10. These dynamic curves correspond to the flow experiment steps as outlined in Section 4.3.2. The flow rate for all solutions was 100 μL/min. Additional bulk refractive index response experiments were conducted with the R_3 and R_4 modes of the same microdisk. The results of all three experiments are shown in Figure 4.11.

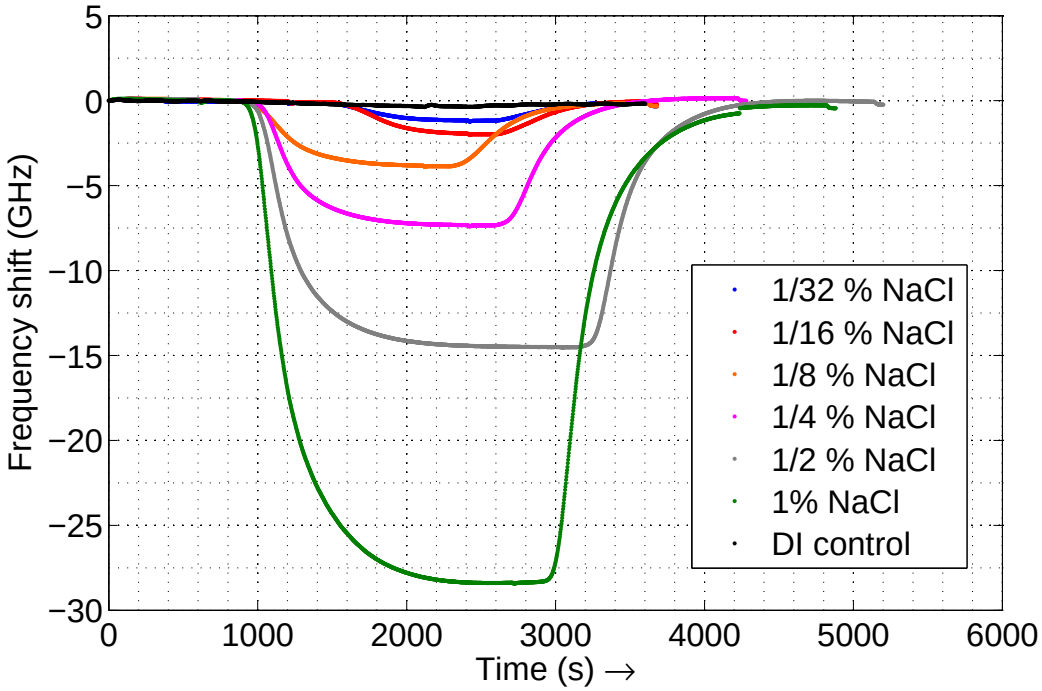

Figure 4.10: The dynamic frequency response of the R_2 mode of the silicon nitride microdisk resonator to the flow of saline solutions of varying salinity.

4.3.2.1 Sensitivity

A linear fit of the data in Figure 4.11 was used to extract the value of the first order correction to the resonance frequency caused by the change in the bulk refractive index of the microdisk upper cladding. The experimentally obtained values for the bulk refractive index sensitivity of the WGM modes were 93.4 nm/RIU 95.25 nm/RIU and 96.8 nm/RIU for the R_2, R_3, and R_4 modes respectively. These values are in good agreement with those obtained from the simulations in Section 4.1.2. The differences between the sensitivities of the different radial order modes are negligible. In the case where the Q — and therefore the limit of detection — for a given mode is limited by water absorption (as is the case at 1310 nm) any mode can be used in sensing experiments without the loss of performance.

The bulk refractive index response measured for the silicon nitride microdisk resonators here is on par with those of other TE mode microdisk resonators [5]. Other traveling wave resonator geometries including silicon and silicon nitride microrings [6],

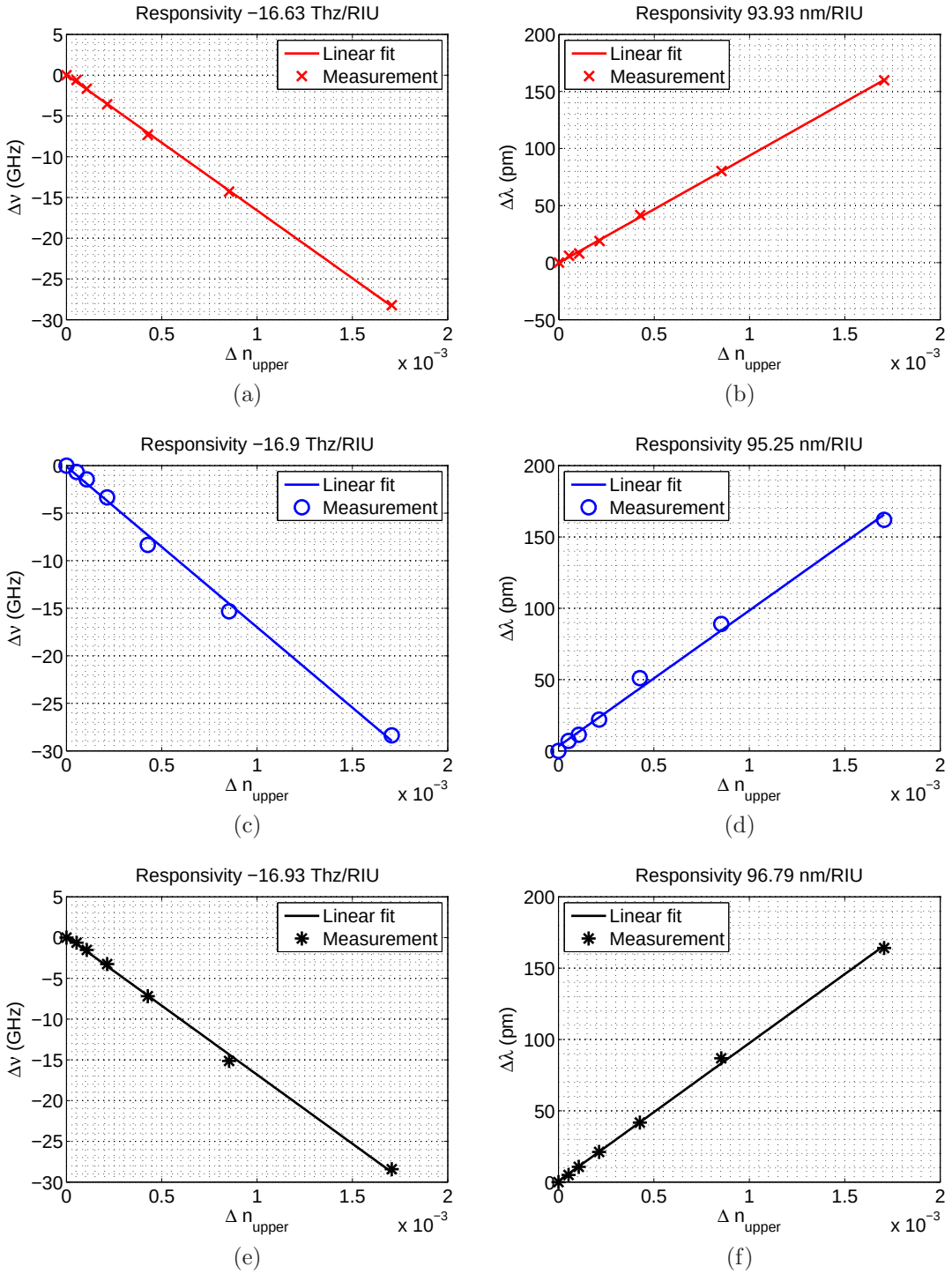

Figure 4.11: Bulk refractive index sensitivity of the R_2 (a) and (b), R_3 (c) and (d), and R_4 (e) and (f) modes of the silicon nitride microdisk resonator.

TM mode microdisks [7], and slot waveguide based microrings [8, 77] have been reported with higher bulk index responses due to a larger overlap of the resonant field with the bulk upper cladding. By the same token, at longer infrared wavelengths, the wet Q of these resonator structures suffers leading to reduced limit of detection. Table 4.2 summarizes the bulk sensitivity of the aforementioned resonator sensors along with their wet Q factors and extrapolated bulk Δn detection limits.

4.3.2.2 Limit of detection

The limit of detection, defined as the smallest resolvable refractive index change, is the major figure of merit of a refractive index based label-free biosensing system. This number is typically arrived at by dividing the minimum detectable resonant frequency shift $\Delta\lambda_{min}$ by the sensitivity $\Delta\lambda/\Delta n$. The minimum detectable resonance shift is influenced by many factors including the resonator wet loaded Q, resonator drift, laser drift, detector electrical noise, and data processing techniques. Some authors [13] claim that the resonance shifts on the order of $\Delta f/100$ — where Δf is the resonator linewidth — are achievable. Others [7] hold that the minimum resolvable shift should only be $\Delta f/2$ thereby creating a more level playing field where the resonator's characteristics, and not the sophistication of the measurement scheme, are at the fore. The values of Δn min reported in Table 4.2 are those given in the literature. As for this work, given the measured sensitivity of 96 (nm/RIU) and wet Q of 3.6×10^5, the extrapolated theoretical limit of detection of detection is 3.9×10^{-7}

Type	Material	λ_0 (nm)	$\frac{\Delta\lambda}{\Delta n}$ (nm/RIU)	Q	Δn min
disk	Si_3N_4	970	91	7.5×10^4	1.4×10^{-6}
disk	Si_3N_4	1310	95	4×10^5	3.8×10^{-7}
disk	Si (TM mode)	1550	142	1.6×10^4	6.8×10^{-4}
ring	Si	1550	160	4.3×10^4	7.6×10^{-7}
slot ring	Si_3N_4	1310	240	2×10^4	8.8×10^{-6}

Table 4.2: Values of the bulk refractive index sensitivity, wet-loaded Q factor and limit of detection for various traveling wave resonator sensors as reported in [5–8] and from this work (shaded).

using $\Delta f/100$ criteria, or 1.9×10^{-5} using the $\Delta f/2$ criteria. Both of these values should be considered to be the theoretical limit of detection for the system. The experimentally determined limit of detection can be gathered from the results of the control experiment shown in figure 4.10 in which the maximum observed frequency shift was nearly 400 MHz over the course of one hour due to the flow of DI water. Taking this value as the minimum detectable frequency change of the system — a conservative estimate — the experimentally determined limit of detection is calculated to be $\Delta n = 2.36 \times 10^{-5}$.

4.3.3 Bulk refractive index response at 1064 nm

We repeated the bulk refractive index response experiments using a swept frequency laser with a nominal wavelength of 1064 nm. All of the experimental procedures were identical to those of the same experiment conducted at 1310 nm. The dynamic resonance response is shown in figure 4.12. The bulk refractive index sensitivity of the device at 1064 nm was determined by a linear fit to the saturated resonance shifts measured in figure 4.12. The results are shown in figure 4.13. The red curve and circles correspond to measured data. The blue curve and circles correspond to simulation results for the R_2 mode. The radial order of the experimentally measured mode is not known because of the large number of modes present in the transmission spectrum.

The measured value for the bulk RI sensitivity of the device at 1064 nm was -13.61 THz/RIU or equivalently 51.7 nm/RIU. There is good agreement between the measured sensitivity and the simulated value of 55.79 nm/RIU. Of the various radial order modes simulated, the simulated values for the responsivity were all near 55 nm/RIU. The sensitivity of the disk to bulk refractive index changes at 1064 nm is only 60% of what it is at 1310 nm. This is due to the lesser penetration of the optical mode into the upper cladding material at 1064 nm than at 1310 nm. The sensitivity could be improved by using a thinner silicon nitride layer as the core thereby delocalizing the the optical mode.

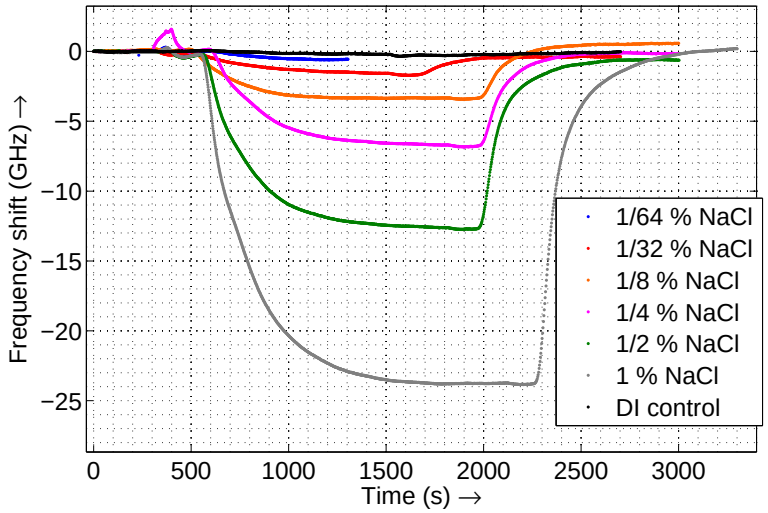

Figure 4.12: The dynamic resonance response of the silicon nitride microdisk resonator to bulk refractive index changes.

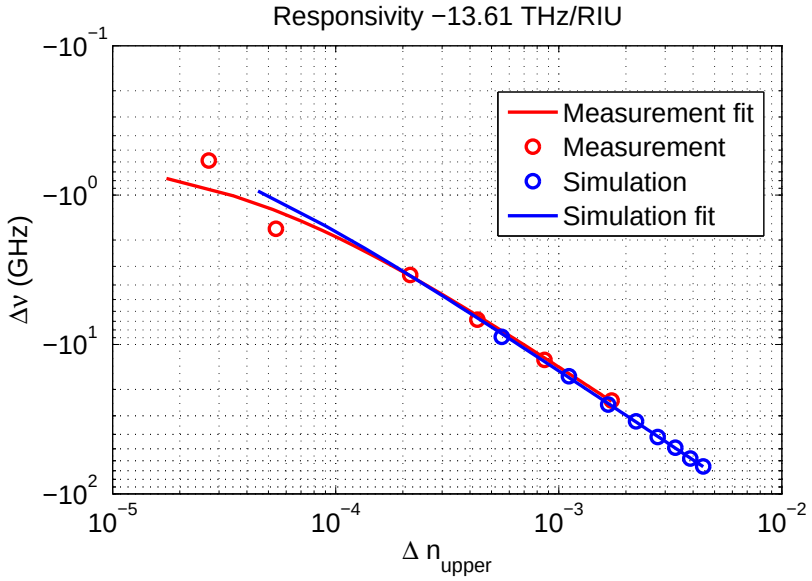

Figure 4.13: The bulk refractive index sensitivity of the silicon nitride microdisk resonator.

The control experiment had a maximum frequency excursion of 200 MHz during the 20 minute target flow step. This control response along with the measured sensitivity of -13.61 THz/RIU leads to an experimental limit of detection of $\Delta n = 1.46 \times 10{-}5$.

4.3.4 Adsorption of proteins

The bulk refractive index response of the microdisk resonator is a key characteristic of any label-free biosensing system. However, the main goal of label-free biosensing is to detect resonant frequency shifts associated with the binding of proteins to the resonator surface or other proteins immobilized thereon. Biomolecules typically have a refractive index $n_{mol} \approx 1.45$. Consequently, when a protein binds to the surface of a resonator displacing water ($n \approx 1.33$), the effective index of the resonant mode increases and induces a red shift in the resonant frequency. Here we present the results of protein binding experiments performed using the silicon nitride microdisk resonators and 1310 nm SFL. These experiments were focused on either nonspecific adsorption of protein or specific adsorption of protein via non-covalent surface functionalization chemistry. The measurement setup used is shown in Figure 4.7.

4.3.4.1 Non-specific adsorption of proteins

To obtain an initial impression of the capabilities of the system for detecting simple protein adsorption events, we investigated the nonspecific adsorption of bovine serum albumin (BSA), a model and well understood protein, to the surface of the silicon nitride microdisks. Nonspecific adsorption is mediated by electrostatic attraction between the protein and a surface and is pH dependent. The pH of the buffer was 7.4, in which BSA is positively charged. Non-specific binding is basically indiscriminate, i.e., BSA should bind to all surfaces including the sensing region of the microdisk. However, as the adsorption is electrostatic and non-covalent, the binding is not permanent and molecules will desorb from surfaces as well. It should also be possible to remove bound BSA using a surfactant or low pH buffer.

Experiments to characterize the response of the resonator to nonspecific adsorption were similar in structure to the saline solution bulk refractive index experiments. Solutions consisting of BSA in phosphate buffered saline (PBS) were made from a stock solution purchased from Thermo Scientific. Concentrations ranging from 100 fM (1×10^{-13} mol/L) to 1 μM in steps of 10$\times$ were prepared by sequential dilution. The

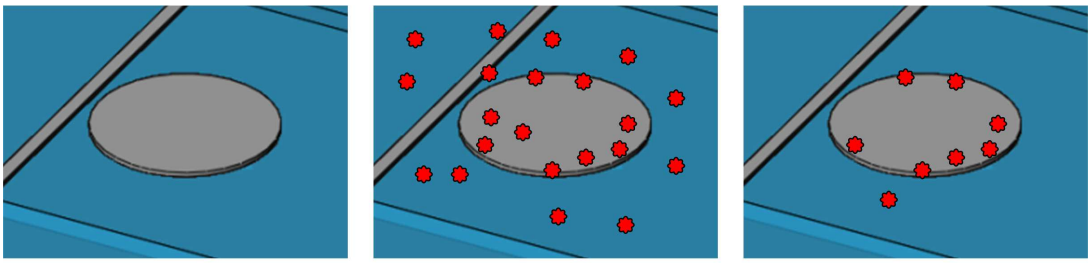

Figure 4.14: (a) The microdisk prior to flow of BSA solution, (b) microdisk surrounded by BSA solution, (c) microdisk post PBS flush showing nonspecifically adsorbed BSA.

following procedure was used to introduce BSA solutions to the microdisk surface:

1. Flow PBS for several minutes to obtain baseline response and resonant frequency.

2. Flow BSA solution and observe resonant frequency shift.

3. Flow PBS to flush microfluidic channel, removing excess BSA solution and unbound BSA.

4. Flow sodium dodecyl sulfate (SDS) solution, a surfactant, to remove all BSA from all surfaces in preparation for the next experiment.

5. Flow PBS to return the sensor to baseline operation.

Experimental results from selected experiments are shown in Figure 4.15. The flow rate for all solutions was 50 μL/min. The BSA concentrations for experiments shown in Figure 4.15 and are rather large and were from the upper range of concentrations used in experiments. A control experiment consisting of a PBS buffer flow was also performed to serve as a reference. In general, the nonspecific adsorption experiments were not very reliable and it was difficult to reproduce results on demand. We believe this is due to the pH sensitivity of the electrostatic interaction between BSA and silicon nitride. For a given set of non-specific adsorption experiments comprising a flight of BSA concentrations from 100 fM to 1 pM, all concentrations provoked

an obvious resonance shift from the resonator. However, there lacked a clear trend between increasing concentration of BSA and increased magnitude of the resonant frequency shift. Such a relationship is necessary for the label-free biosensing system to be realized as a tool for quantitative measurement.

4.3.4.2 Specific adsorption of protiens

Using the silicon nitride microdisk resonator platform, we performed proof-of-principle specific sensing experiments with the proteins biotin and streptavadin. The streptavadin/biotin interaction is well understood [78, 79] and the specific binding of these proteins has been used to characterize several label-free biosensing systems [6, 80]. We used the covalent surface functionalization method discussed in Chapter 6. This technique covalently tethers biotin molecules to the resonator surface at the end of a short polyethylene glycol (PEG) chain (tens of nanometers in length). The biotin molecules are then available for streptavadin molecules to bind onto as they pass though the microfluidic channel.

The functionalized resonator was first exposed to a buffer solution consisting of PBS with 0.1% BSA. The BSA in the buffer solution serves to occupy and bock all of the non-specific adsorption sites on the resonator. This ensures that any resonant frequency shift seen is due to the specific binding of streptavadin and biotin and not to the non-specific adsorption of streptavadin onto the disk surface. Streptavadin analyte solutions were also prepared by disolving streptavadin into the same PBS-BSA buffer solution. Analyte solutions with concentrations of streptavadin ranging from 100 fM to 100 nM were flown over the resonator surface. A control experiment, in which the analyte solution was also the PBS-BSA buffer, was also performed.

The results of the experiment are shown in Figure 4.16. Only the results from the control and 100 nM streptavadin solution are shown. The 100 nM solution exhibited a clear and large resonance shift of nearly 35 GHz during the twenty minute flow period. The resonance shift continued and then saturated during the buffer flush step. The saturation of the resonance during this step is evidence that the resonance shift observed is due solely to the binding of streptavadin and biotin and therefore an

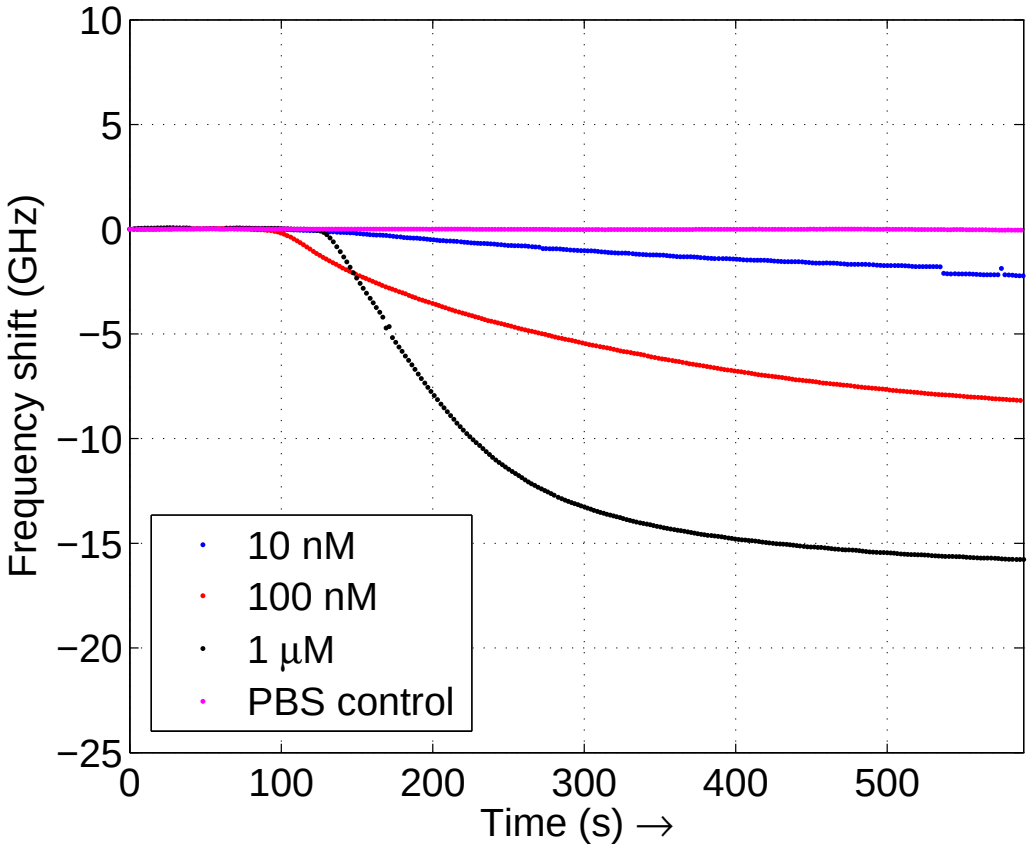

Figure 4.15: The dynamic response of the R_2 mode of the silicon nitride microdisk resonator to the flow BSA solutions of various concentration. The nominal wavelength was 1307 nm. Note that steps 3 through 5 are not shown.

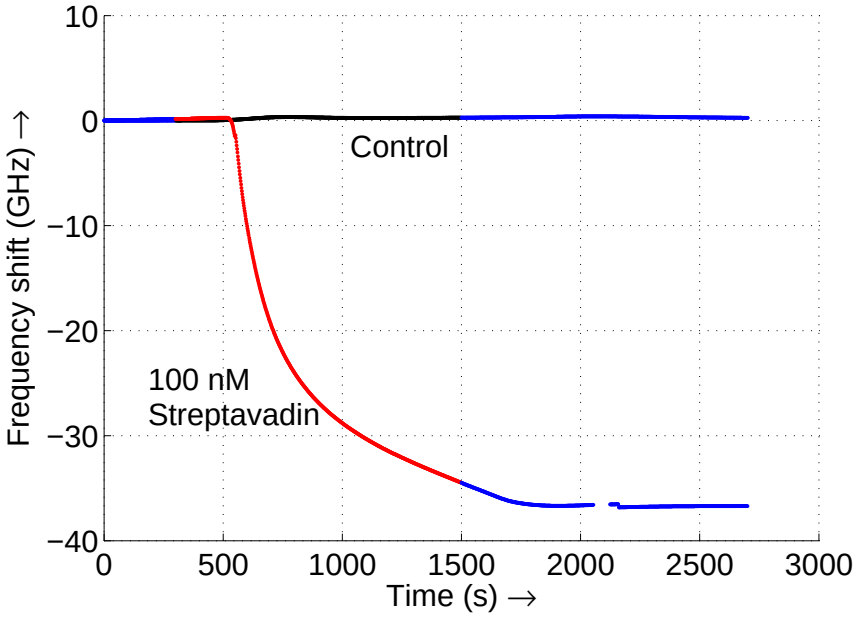

Figure 4.16: Dynamic resonance response of a silicon nitride microdisk resonator covalently functionalized with biotin to a 100 nM streptavadin solution and to a control buffer solution.

alteration of the resonator surface. The responses from the other analyte solutions were not distinguishable from the control on this scale. The flow rate of all of the solutions was 50 μL/min. At this flow rate, it is possible that there is not enough time for diffusion to transport streptavadin molecules through the flow boundary layers to resonator surface at low concentrations. This can be improved by reducing the flow rate to allow for increased diffusion time.

Chapter 5

Differential sensing with dual silicon nitride (Si_3N_4) microdisk resonators

5.1 Introduction

The extreme sensitivity of high-Q optical resonators to refractive index perturbations makes them fantastic sensors for the detection of biomolecule interactions in label-free biosensing experiments. Unfortunately, analyte binding events are not the only thing that can affect the effective index of the resonant mode and cause a shift in the resonant frequency. Changes in environmental temperature and pressure, flow effects, and drift in the laser sweep starting frequency can all result in spurious frequency shifts that obscure the resonator response signal due to analyte binding.

Here, we implement a differential sensing technique to remove these environmental factors from the measurement. This is accomplished by utilizing two high-Q silicon nitride microdisk resonators coupled to the same waveguide. The dual disk approach provides an on-chip reference which can be interrogated concurrently with the resonator under test without the need for additional optical inputs and outputs, or supporting hardware.

In this chapter, we discuss the observed drift in resonant frequency of the microdisk resonators both in the air environment and under flow during sensing measurements. A solution to the resonance drift issues in the form of dual microdisk resonators

in a dual laminar flow microfluidic channel is proposed. Theoretical analysis and numerical simulations of the dual flow microfluidic channel are presented along with a qualitative experimental demonstration. Finally, we show a reduction of resonance drift in measurements of bulk refractive change and non-specific adsorption of BSA using the dual resonator dual flow differential sensing technique.

5.2 Resonant frequency drift

Changes in the resonant frequency of the whispering gallery mode not associated with adsorption of the target analyte are undesired. Resonance drift, regardless of physical origin, diminishes the limit of detection of the measurement system, negating the resolution ($\Delta\lambda_{min}$) advantage of having a high-Q resonator. Spurious drifts can also corrupt analyte binding signals making a quantitative assay inaccurate or impossible.

Measurements of the relative position of the resonant frequency over time frequency can be corrupted by drift from two sources,**(1)** unintended perturbations to the resonator's environment, and **(2)** variations in the starting frequency of the linear chirp produced by the SFL.

5.2.1 Environmental resonance drift

5.2.1.1 Flow induced drift

We observed resonant frequency drift at various rates when microdisks were subject to flow through the integrated microfluidic channel. Examples of two such cases are shown in Figure 5.1. The measurement for the red curve was taken directly after that of the curve in blue. Two syringes, each with DI water, were connected to the microfluidic flow delivery system via a manually actuated valve. The driving flow was alternated between these two sources every 10 minutes corresponding to the periodic short lived transients in the figures. Recall from the simulation and analysis of the resonator thermo-optical characteristics in Chapter 3 that the microdisk mode with a water upper cladding has an overall negative thermo-optical coefficient dn/dT. This

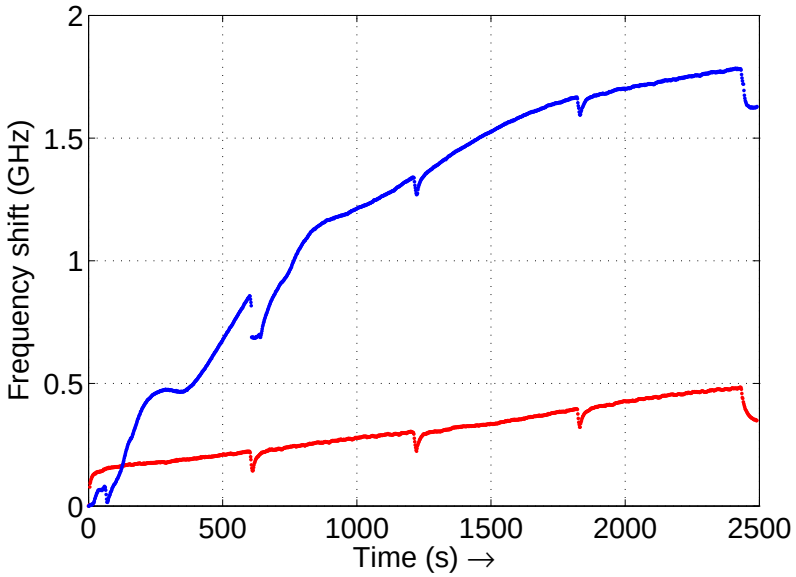

Figure 5.1: Dynamic response of the microdisk resonator to flow of deionized water at 100 μL/min

implies that increases in the mode temperature should result in a decrease of the mode effective index and therefore an increase in the resonant frequency (decrease in wavelength). Similarly, decreases in the resonator temperature should result in a decrease in the resonant frequency (increase in wavelength). Both flow experiments exhibit a blue shift in the resonant frequency which we attribute to warming of the resonator and the solution immediately surrounding it by optical absorption. This explanation also helps to explain the decrease in drift rate during the initial flow and the more constant drift rate in the second experiment in terms of the system reaching a thermal equilibrium.

5.2.1.2 Laser drift

Measurements of relative frequency shifts require some reference frequency from which to judge changes. In the case of a single microdisk resonator interrogated by an SFL this reference frequency is the starting frequency of the linear optical chirp. The laser frequency output is given by Equation 2.1. The steady state analysis of the SFL control loop resulted in Equation 2.12 which relates the starting frequency of

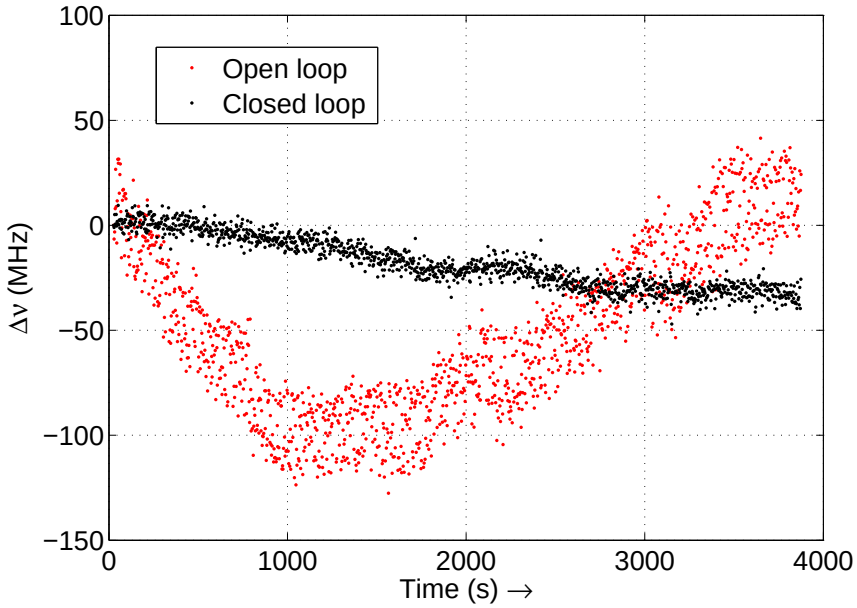

Figure 5.2: Resonant frequency drift as a function of time over an hour, measured with a high-Q mode of a silicon nitride microdisk with an air upper cladding.

the sweep to the phase of the reference oscillator and the delay of the interferometer. Small changes in the length of the delay due to variations in the temperature or length of the interferometer — known as fiber breathing — result in drift of the starting frequency of the SFL. Drift in the free running starting frequency of the laser may also manifest as drift in the closed loop starting frequency of the laser. However, the free running frequency difference is more likely the cause of discrete jumps in the starting frequency equal to the FSR of the MZI as indicated by the $2\pi m/\tau$ term in Equation 2.12. These FSR frequency jumps are easily recognized and corrected for during measurements.

Experiments to determine the starting frequency drift of the laser were performed with the SFL in both open loop and closed loop configurations. Using the sensing system shown in Figure 4.1, transmission spectra of a Si_3N_4 microdisk resonator mode with a loaded Q factor of 2.1×10^6 were captured at 3 second intervals for one hour. The resonator chip was covered by a PDMS microfluidic channel permanently bonded to its surface (the channel was free of liquid during these measurements), and the measurement was performed in an enclosure to minimize exposure to thermal

variations and air currents in the laboratory. The total temperature change in the measurement enclosure during the measurements was less than 0.01°C as measured by a thermistor located near the device. Lorentzian lineshape functions were fit to each spectral measurement and the drift in resonant frequency over the duration of one hour was calculated. The results are shown in Fig. 5.2. In the open loop case, where neither the starting frequency of the sweep nor the sweep rate are locked to the electronic reference, the mean and variance of the frequency drift were calculated to be -50 MHz and 1.6×10^{15} Hz^2 respectively. The maximum frequency excursion was -120MHz over 1 hour. In the closed loop case, the mean and variance of the frequency drift were calculated to be -17 MHz and 1.5×10^{14} Hz^2 respectively. The maximum frequency excursion was -37 MHz over one hour.

Operating the SFL in the closed loop configuration provides nearly an eight fold improvement in mean wavelength drift and nearly a 19 fold improvement in the variance of the frequency drift. The open loop case performed better than expected due to the use of the predistorted open loop driving current. The starting frequency drift of the SFL in the closed loop case is ultimately limited by the stability of the fiber MZI in the feedback loop. Great care was taken to isolate the MZI from both thermal and vibrational instabilities. The measured frequency drift of 37 MHz over one hour corresponds to a thermal drift in the fiber MZI of approximately 0.008°C. Slightly better thermal stability may possibly be achieved by immersing the MZI in an ice bath to stabilize its temperature to 0.001°C as in [14].

The previous measurement of long term laser drift relied on the assumption that the resonant frequency was stable through out the experiment. Strictly speaking, the drift measured was that of the entire system. The drift solely due to starting frequency variation can be isolated using the SFL to observe a molecular vibrational transition such as a gas absorption line. HF gas has absorption lines at both 1304 nm and 1312 nm and could be used for this purpose. However, we did not perform this measurement.

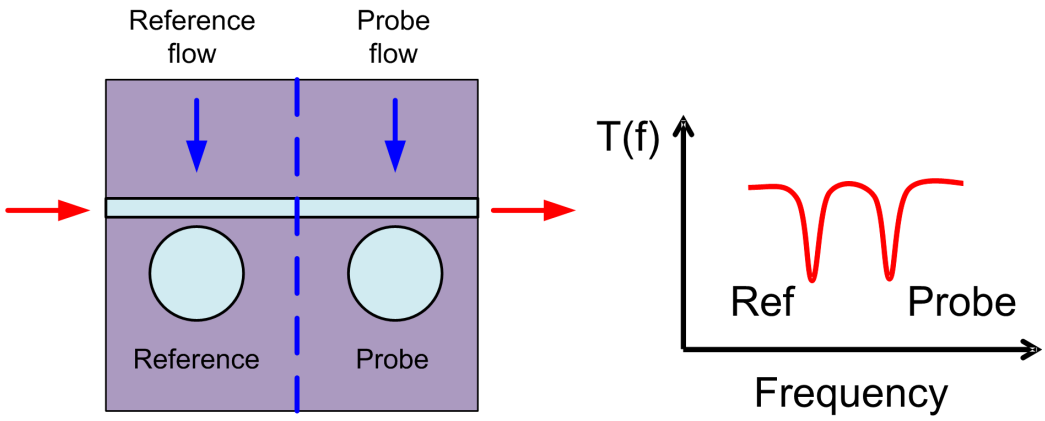

Figure 5.3: A conceptual diagram of the concept of dual microdisk resonator differential label-free biosensing. Red arrows are the optical signal. Two blue arrows signify two distinct laminar flows. The mock transmission spectrum shows the independent resonances of the two disks simultaneously.

5.3 Dual microdisk resonators

Undesired resonance drift is an unavoidable fact of refractive index based label-free optical biosensing. These complications, whether environmental or systemic in origin, are difficult to separate and understand. The solution to these issues is to employ a differential measurement to reject the spurious signals introduced by these noise sources.

5.3.1 Dual disk proposal, design, and idea

A differential measurement seeks to reject unwanted environmental fluctuations as common mode noise by subtracting two signals, a reference and a probe, that are both exposed the the same noise sources. The design of a differential measurement scheme for the label-free optical biosensing system must consider all sources of system noise to be rejected and ensure that both the probe and reference resonators are exposed to them.

A schematic of the chosen differential measurement architecture is shown in Figure 5.3. Two silicon nitride microdisk resonators are coupled to the same bus waveguide. The composite transmission spectrum of the waveguide should therefore contain

Lorentizian shaped dips corresponding to the modes of both resonators. Slight imperfections in the fabrication of both resonators will ensure that the resonant modes of the two disks will be close in frequency, allowing them to be easily monitored simultaneously, but not overlapping. Alternatively, the radius of the disks could be chosen to differ slightly, imposing a frequency offset. A dual flow microfluidic channel is used to flow independent solutions over the probe and reference disk simultaneously. The laminar flow that occurs within a microfluidic channel allows for side-by-side propagation of two distinct liquids without mixing. Aiming to take advantage of this effect, we flow a reference buffer solution over the reference disk and the analyte solution over the probe disk simultaneously. This side-by-side flow structure creates nearly identical environmental conditions, i.e., pressure, temperature, and flow rate, for both the probe and reference disk.

The use of a dual disk differential sensing scheme relaxes requirements on the SFL used in the measurement. The long term stability of the starting frequency of the optical chirp is no longer necessary. A precisely linear chirp is still required.

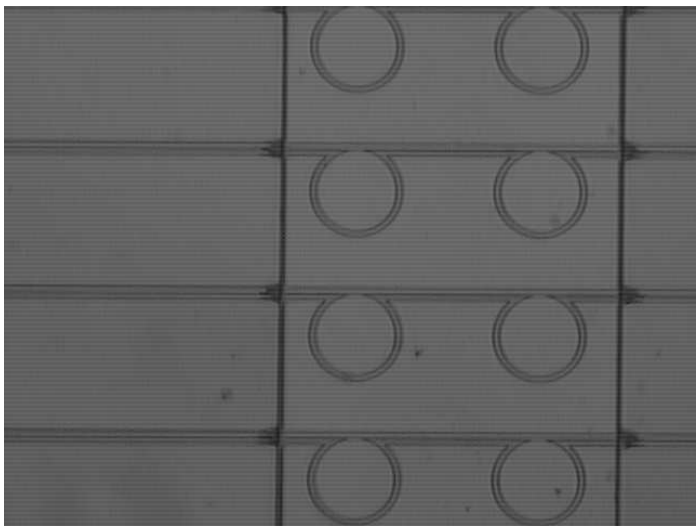

Figure 5.4: An overhead image of the dual disk resonators within a dual flow microfluidic channel

5.3.2 Experimental demonstration

To investigate the potential of the dual disk differential sensing technique we fabricated devices using the same fabrication procedure as described in Section 3.4.1. An optical micrograph of the dual disk resonators lying within a dual flow microfluidic channel is shown in in Figure 5.4.

We measured the transmission spectra of the dual disk resonator devices using the measurement system shown in Figure 4.1. The SFL had a nominal wavelength of 1310 nm and produced optical frequency sweeps with a duration of 1 ms and a frequency bandwidth of 100 GHz. The transmission spectrum of a representative dual disk resonator device is shown in Figure 5.5.

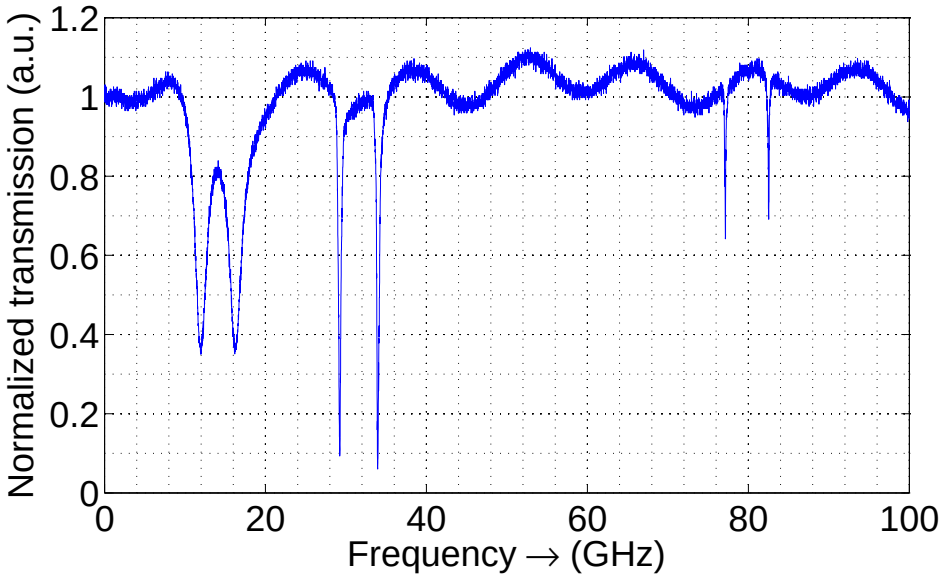

Figure 5.5: The normalized transmission spectrum of a dual disk resonator device. Three different radial order modes are seen for each disk.

As a proof-of-concept experimental demonstration of differential sensing with a dual microdisk resonator device, we tracked the resonant frequency of the device measured by the SFL as it warmed up. The warm up period of the SFL is typically several hours during which the SCL and fiber MZI settle to their respective steady state temperatures. The results from the measurement are shown in Figure 5.6. The pair of resonances used in the experiment were both R_2 modes. The quality factors

of each mode were 1.7×10^6 and 1.5×10^6 for the left and right mode respectively. A representative transmission spectrum captured during the measurement is shown in Figure 5.7. The mean and variance of the frequency drift of the differential signal were -1.7 MHz and 3.2×10^{13} Hz^2 corresponding to a mean and variance of the wavelength drift of .09 pm and .0001 pm^2. This uncertainty in the resonance position yields a limit of detection of $\Delta n = 3.6 \times 10^{-7}$ for measurements taking place on the time scale of an hour.

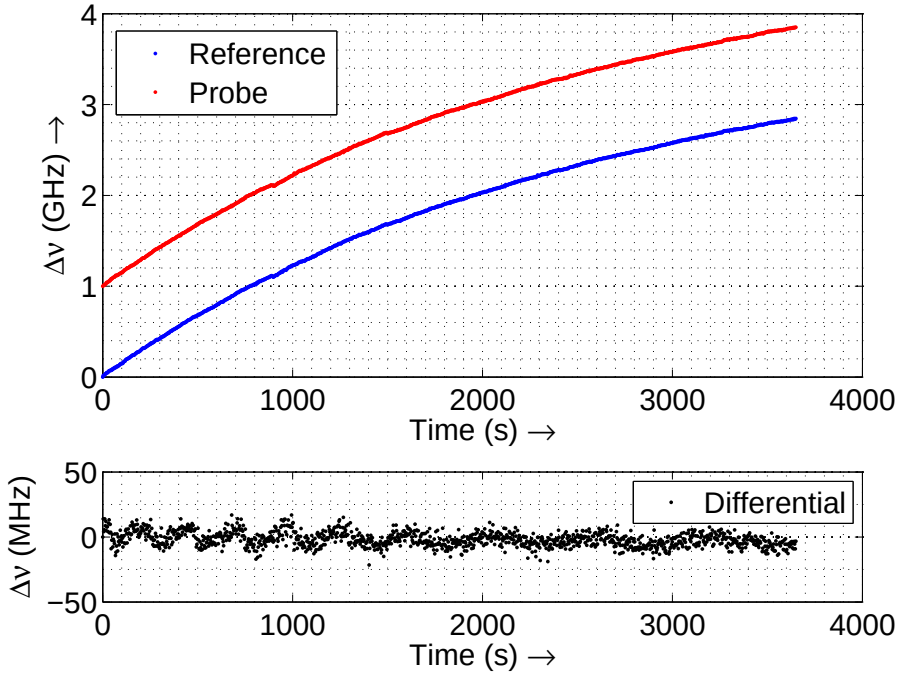

Figure 5.6: Dynamic resonance shift over 1 hour during SFL warm up. The individual resonance positions are shown in the upper panel. The differential signal is shown in the lower panel. A 1 GHz offset is applied between the reference and probe curves on the upper panel in order to distinguish them.

The results are a direct confirmation of the idea behind differential measurement and the implementation of this idea using dual resonators coupled to the same waveguide. The individual resonances drift by 2.85 GHz during the hour long measurement. The differential signal drifts by only 6.2 MHz in that same time. This represents a 460 fold improvement. In comparison with the hour long drift results obtained with a single microdisk (with the starting frequency of the sweep as the reference) from

Figure 5.2, of 37 MHz, differential sensing produces a nearly six fold improvement. Another important implication of this result is that the SFL warm up period is no longer a time that is unsuitable for conducting measurements with the system.

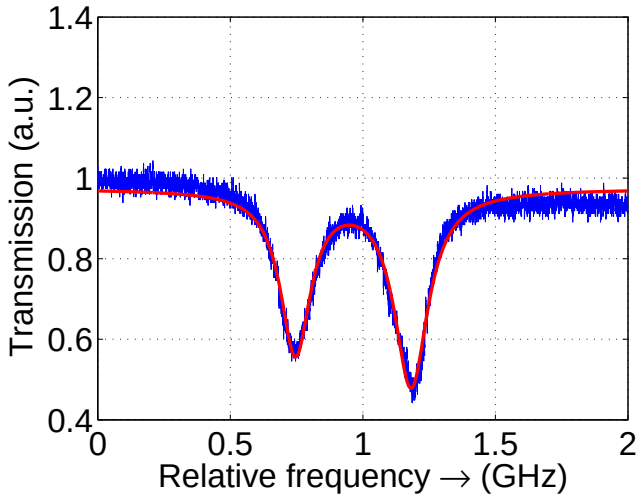

Figure 5.7: A detailed view of the transmission spectrum of a single pair of R_2 mode resonances from a dual disk device. The blue curve is the measured data, the red curve is a double Lorentzian fit. The loaded Q of left and right modes were 1.7×10^6 and 1.5×10^6 respectively.

5.4 Dual flow microfluidic channels

It is well known that fluids traveling within small channels in which the Reynolds number Re is low, i.e., $Re \approx 1$, experience laminar flow [81]. Transport of dilute particles within laminar flows is mediated by diffusion, making mixing of laminar flows very difficult [82]. The lack of mixing in side-by-side laminar flows is an advantage in the design of the dual flow microfluidic channel envisioned in Figure 5.3. Here, we use both analytical and theoretical fluid flow models in the design of the dual flow channel microfluidic device. Careful design of the channel width and the diffusive mixing region are necessary to maintain separation of flows over the microdisk resonators and to avoid diffusion of analyte from the probe flow into the reference flow.

5.4.1 Confluence of laminar flows

In order to gain an understanding of the characteristics of the dual laminar flow channel we use a simple model shown in Figure 5.8a where the analyte flow is on the left side and the reference flow (that does not contain any analyte) is on the right side. Starting with the continuity equation for an incompressible flow we have

$$\frac{\partial c_N}{\partial t} + \left(v_x \frac{\partial c_N}{\partial x} + v_y \frac{\partial c_N}{\partial y} + v_z \frac{\partial c_N}{\partial z} \right) = D_N \left(\frac{\partial^2 c_N}{\partial x^2} + \frac{\partial^2 c_N}{\partial y^2} + \frac{\partial^2 c_N}{\partial x^2} \right), \tag{5.1}$$

where c_N is the concentration of analyte species N, v is the velocity, and D_N is the diffusion coefficient of N. Under steady state laminar flow, we take $\partial c_N/\partial t = 0$ and $v_x = v_y = 0$. We neglect axial diffusion so that $(\partial^2 c_N/\partial z^2 = 0)$. Equation 5.1 therefore becomes

$$v_z \frac{\partial c_N}{\partial z} = D_N \left(\frac{\partial^2 c_N}{\partial x^2} + \frac{\partial^2 c_N}{\partial y^2} \right). \tag{5.2}$$

The primary concern in the design of the dual flow microfluidic channel is the limiting lateral diffusion of the analyte species from the probe channel into the reference channel. Dropping the vertical diffusion term from Equation 5.2 and choosing to look at a particular cross section of the channel at a moment in time we obtain the well known one dimensional diffusion equation

$$\frac{\partial c_N}{\partial t} = D_N \frac{\partial^2 c_N}{\partial x^2}, \tag{5.3}$$

where we used

$$v_z \frac{\partial c_N}{\partial z} = \frac{dz}{dt} \frac{\partial c_N}{\partial z} = \frac{\partial c_N}{\partial t}, \tag{5.4}$$

Equation 5.3 has well known solutions of the form

$$c\,(x,t) = c\,(0,0)\,\mathrm{erfc}\left(\frac{\mathrm{x}}{2\sqrt{\mathrm{D_N t}}} \right), \tag{5.5}$$

where erfc is the complementary error function. Plots of Equation 5.5 for several

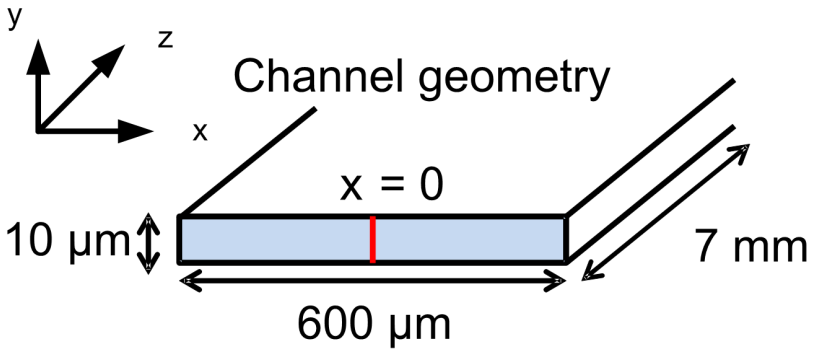

(a)

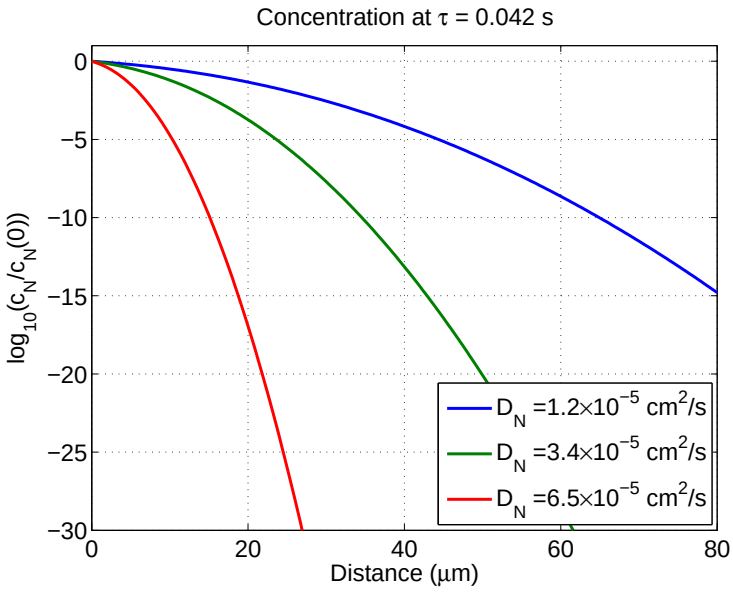

(b)

Figure 5.8: (a) A schematic diagram of the dual flow microfluidic channel for constructing the simple one-dimensional diffusion model. (b) The concentration profile of the analyte species within the reference flow path after side-by-side flow for .042 seconds. The diffusion coefficient is a parameter.

analyte species of interest are shown in Figure 5.8b. These analytes, along with their molecular weight and diffusion coefficients, are given in Table 5.1. The channel under consideration has dimensions 10 μm $\times$ 600 μm$\times$7000 μm as shown in Figure 5.8a. The cross-sectional area is therefore 6000 μm^2. For a volumetric flow rate of 60 μL/min through this cross section we obtain an average flow velocity of 1×10^7 μm/min. For a channel length of 7000 μm the transit time is 0.042 s. This transit time was used as the time for the diffusion calculations of Figure 5.8b.

From the results of the calculations in Figure 5.8b, we see that even for the most diffusive species, the concentration of analyte in the reference flow is nearly five orders of magnitude lower than in the the probe flow at lateral displacement of 40 μm. For a analyte species more akin to those measured in Chapter 4 the concentration is 15 orders of magnitude lower at a lateral displacement of 40 μm. We note that a safe design is nearly guaranteed by placing the resonators more than 80 μm from the flow interface.

5.4.2 Numerical simulations of dual flow

To improve upon the simple one-dimensional diffusion analysis of the previous section and to simulate the full microfluidic channel design in more detail, we performed two-dimensional laminar flow simulations in Comsol using both the fluid flow and the dilute species transport physics models.

In these simulations, the microfluidic channel geometry from figure 5.8a was used to solve for the channel velocity profile throughout. The Reynolds number was found to be less than one, allowing for the Stokes flow approximation [81]. With the velocity

Molecule	calcium	fluorescent biotin	BSA
MW (daltons)	40	831	66,000
D_N (cm^2/s)	1.2×10^{-5}	3.4×10^{-6}	6.5×10^{-7}

Table 5.1: The molecular weight and diffusivity of analyte molecules of interest used in the one-dimensional diffusion model for side-by-side laminar flows. MW is molecular weight.

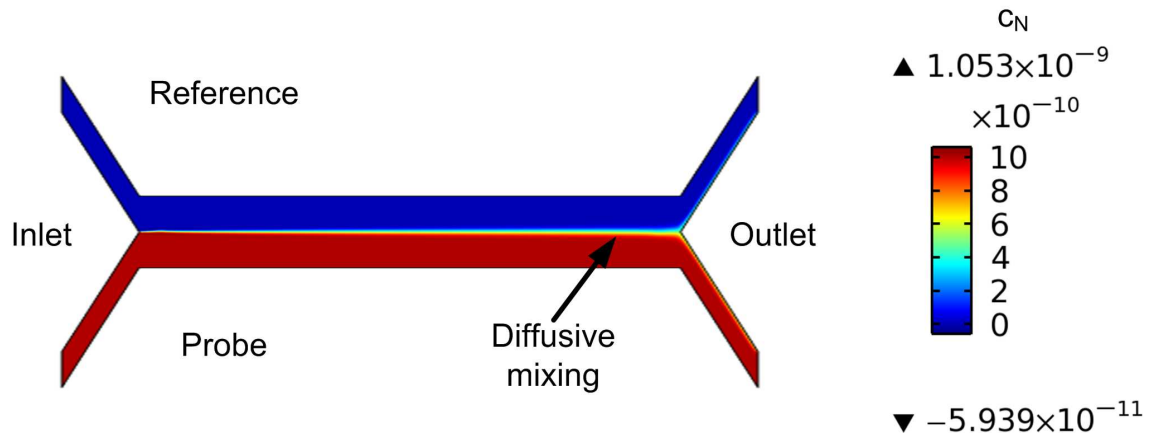

Figure 5.9: The concentration profile of a dilute species under steady pressure-driven flow in a dual flow microfluidic channel. For this simulation $D_N = 6.5 \times 10^{-7}$ cm^2/s and the volumetric flow rate was 60 μL/min. The dimensions of the main channel were 10 μm $\times$ 600 μm $\times$ 7000 μm.

profile in hand, the concentration profile of the dilute species introduced to the channel via the probe inlet was calculated by numerically solving Equation 5.2. The results are shown in Figure 5.9.

For a given microfluidic channel width, the main design parameter is the distance from the channel center to the edge of the resonators. We desire the resonators to be sufficiently far from the channel center that there is no overlap of the reference resonator with the region of diffusive mixing that forms at the flow interface. From Figure 5.9 it is clear that two laminar flows stay separated and that there is very little diffusive mixing. In the simulation, the pressure difference between the inlets and outlets was 25 kPa leading to a maximum flow velocity of 1.6 cm/s; this is close to the experimental flow velocities. The diffusion coefficient of the analyte was $D_N = 6.5 \times 10^{-7}$ cm^2/s corresponding to that of the protein BSA. The concentration and velocity profiles along a cut line transverse to the direction of flow and 1 mm from the end of the channel are shown in Figures 5.10a and 5.10b respectively.

The velocity profile of the flow depicts nearly uniform velocity across the channel. The zero velocity at the channel boundaries are a result of the non-slip condition [81]. Typical laminar flow in a pipe exhibits a parabolic velocity profile, however the very high aspect ratio of the microfluidic channel, in this case 60 : 1, leads to the very

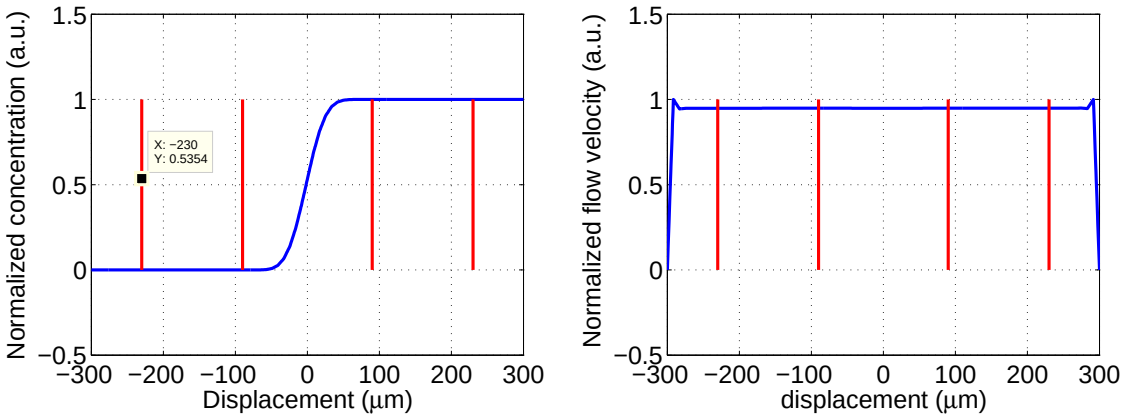

(a) (b)

Figure 5.10: (a) The concentration profile of the dual flow channel simulation, (b) the velocity profile of the dual channel flow simulation. The red vertical lines mark the positions of the microdisk resonators.

uniform velocity profile. The concentration profile clearly shows the region of diffusive mixing. We see that at 50 μm displacement from the center of the channel, the concentration of analyte in the reference flow is negligible. The red vertical lines in both figures denote the extents of the microdisk resonators. It is clear from the simulations that placing the disks 160 μm apart edgewise will ensure equal velocity flow over each disk while keeping both in their respective flows. This choice of resonator spacing coincides with the size of one main field of the e-beam lithography system. Using a single main field for each disk and one for the space between the devices is important to avoid stitching errors that may arise from writing a mask pattern across two exposure areas. Stitching errors result in increased scattering and therefore lower Q resonances.

We fabricated the dual channel microfluidic devices from PDMS using the same fabrication procedure as outlined in Chapter 4. The channel geometry was identical to that of the simulation shown in Figure 5.9. The main flow section had dimensions of 10 μm $\times$ 600 μm $\times$ 7000 μm. The inlet and outlet tributaries had dimensions of 10 μm $\times$ 300 μm $\times$ 1000 μm and were set at an angle of 45 degrees to the main channel.

As a qualitative proof-of-concept, we bonded a dual flow device to an unpatterned

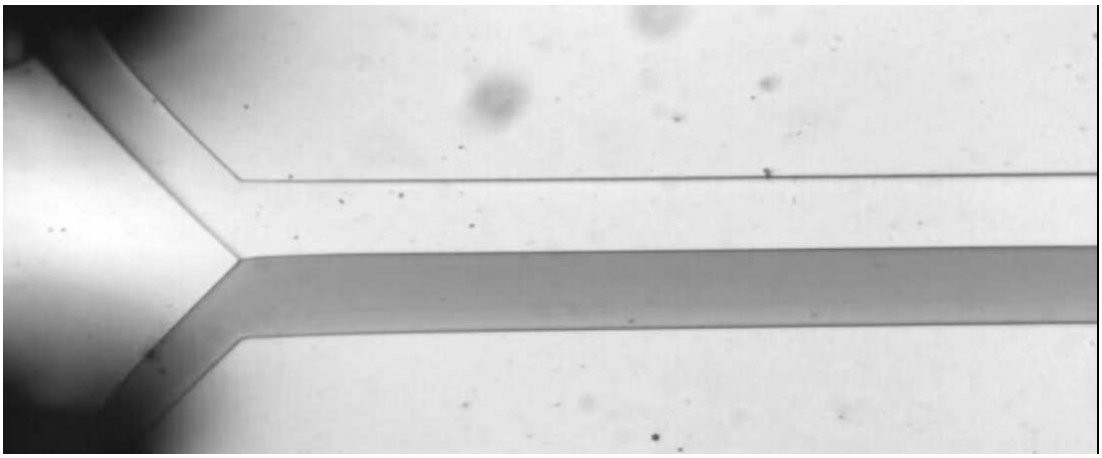

Figure 5.11: An optical micrograph of the dual laminar flow channel with water and dilute blue ink solution flowing side by side at 10 μL/min.

silicon nitride dummy chip using the oxygen plasma treatment described in Chapter 4. We then used a syringe pump to inject both DI water and a dilute blue ink solution into the channel. A frame capture from a video of this experimental demonstration is shown in Figure 5.11. The separation of flows is readily apparent. Flow rates from 3 μL/min to 300 μL/min were used, no qualitative difference in the flow separation was seen.

5.5 Experimental demonstration

Having prepared the foundation for the dual microdisk resonator differential sensing technique in the previous sections, we move on to experimental demonstrations. Here, we combine the optical and microfluidic modules to demonstrate differential sensing of bulk refractive index changes as well as non-specific adsorption of BSA at a concentration of 100 fM.

5.5.1 Bulk refractive index experiments

An experimental setup similar to that of Figure 4.7, with the addition of a second syringe pump to feed the reference flow channel, was used to perform bulk refractive index response measurements. Transmission spectra of the dual resonator device were

captured once per second. Individual Lorentzian lineshape functions were fit to each of the probe and reference resonances. The individual resonance positions as well as the difference between them, taken to be $\Delta\nu_R - \Delta\nu_P$, were then plotted as a function of time. The procedure for the experiment was the following:

1. Initialize flow of deionized (DI) water over both reference and probe resonators at the same flow rate.

2. Switch probe resonator flow to saline solution via computer actuated solenoid valve. Reference flow remains DI water.

3. Switch probe flow back to DI water. Reference flow remains DI water.

An example of a dynamic resonance response curve is shown in Figure 5.12. The observed resonant frequency shift is in response to the flow of 1/256% by weight NaCl solution corresponding to a bulk refractive index change $\Delta n = 6.4 \times 10^{-6}$ according to [76]. The flow rate of the both the reference and probe solutions was 100 μL/min. The flow steps were of 5 minutes, 15 minutes, and 15 minutes duration respectively. A control experiment consisting of the continuous flow of DI water in both channels was also performed and is shown in Figure 5.12. The control experiment resulted in a resonance shift of approximately 65 MHz which can be used with the measured bulk refractive index response to determine the experimental limit of detection.

Both the individual probe and differential curves clearly display the resonance shift due to the introduction of saline. However, there is a small amount of resonance drift that can be seen from the reference resonance that is not present in the difference signal. Additionally, a periodic modulation of the resonance frequency is seen in both the reference and probe signals but is removed in the difference signal. The differential technique clearly cleans up both measurement noise and unwanted resonance drift in bulk refractive index response measurement. Note that we see no resonance shift in the reference signal after the introduction of saline. This is evidence that reference and probe flows are indeed separated and that there is no contamination of the reference

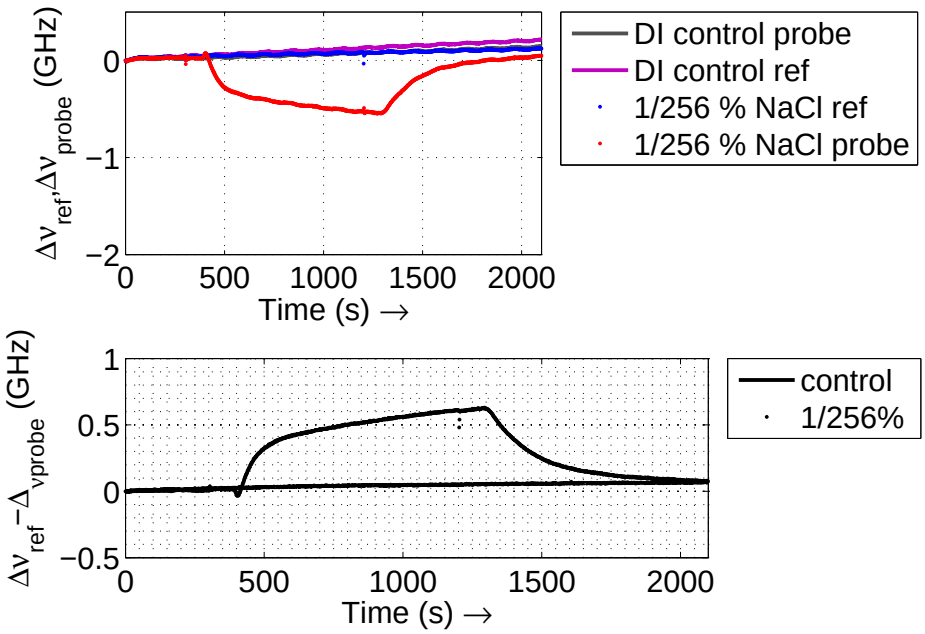

Figure 5.12: The dynamic resonance response of a dual resonator device. The upper panel shows the resonance shift of both the reference and probe resonators. The lower panel shows the differential signal.

channel by diffusive transport. Simply put, the dual flow microfluidic device performs as intended.

The previous experimental demonstration of the bulk refractive index response of the differential sensor to 1/256% saline solution was done in the context of a flight of saline solution concentrations. The goal of these experiments was to show the noise and drift reduction accomplished by the differential measurement over a large range of bulk refractive index differences. As in the single resonator experiments, saline solutions were prepared by sequential dilution from a stock 1% NaCl by weight solution. The differential signal from the dynamic resonance responses are shown in Figure 5.13a. The maximum or saturated frequency shift observed during each flow experiment is plotted vs. Δn in Figure 5.13b. A linear fit to the bulk refractive index response yeilds a slope of 18.2 THz/RIU and is in good agreement with the trend of salinities $1/64\% - 1/4\%$. However the responses from the two lower concentration saline solutions were slightly larger than would be predicted by the simple linear

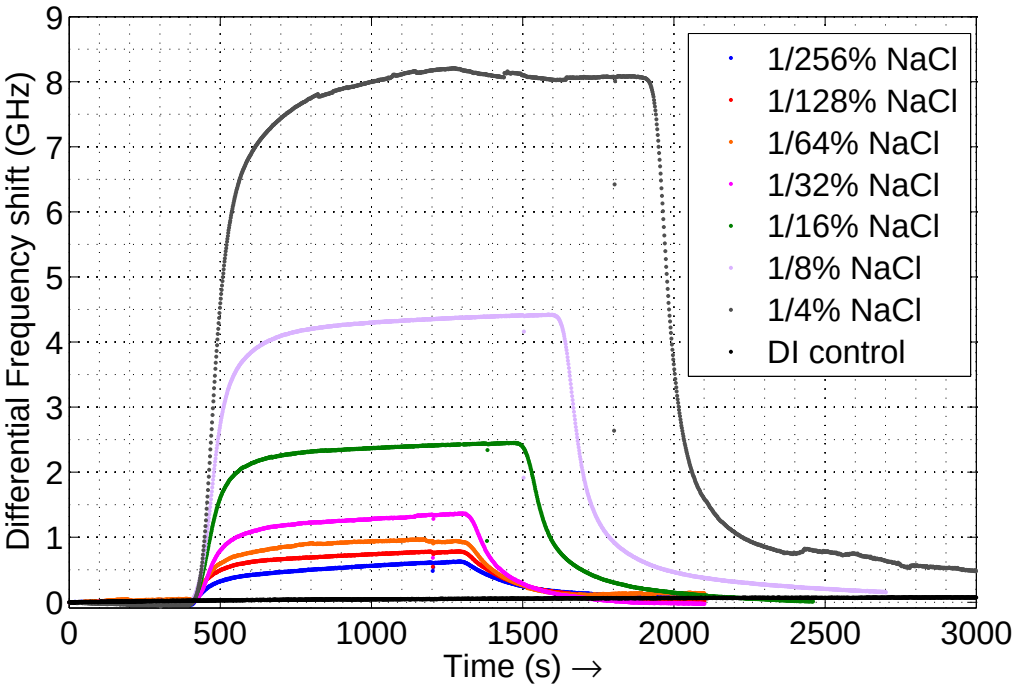

(a)

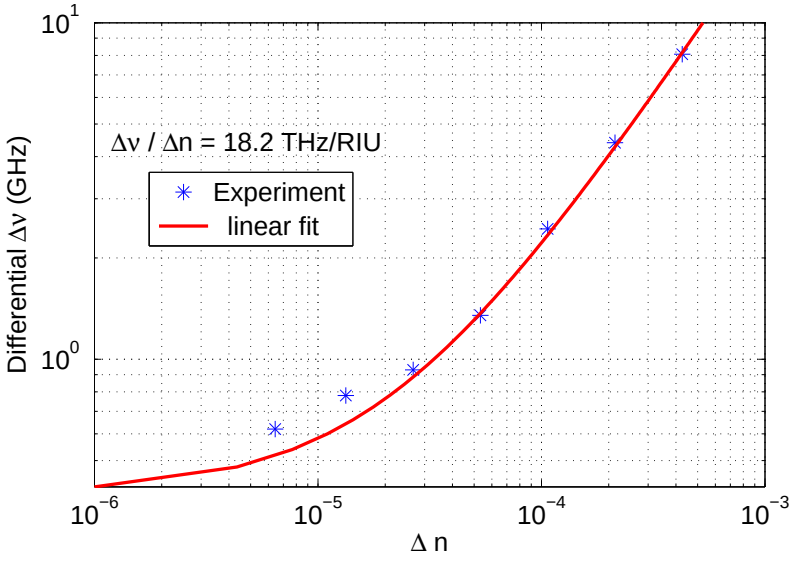

(b)

Figure 5.13: (a) Differential dynamic resonance response for bulk refractive index flow experiments. (b) The bulk refractive index response as determined from the experimental data in (a).

model. This is most likely due to second order corrections to the resonant frequency caused by bulk refractive index perturbations. We note that resonator sensitivity derived from the slope is 7.7% greater than that measured for the single disk sensor and predicted by numerical simulations. The cause of this discrepancy is not currently understood.

Using the experimentally determined bulk refractive index sensitivity of 18.2 THz/RIU and the control experiment resonance drift of 65 MHz, yields an experimentally determined limit of detection of $\Delta n = 3.57 \times 10^{-6}$. This represents nearly an order of magnitude improvement over the experimental limit of detection of the single disk device.

5.5.2 Non-specific adsorption of BSA

We also experimentally demonstrated the sensing of nonspecific adsorption of the protein BSA at ultra low concentrations using the dual resonator differential measurement. The silicon nitride resonator surface was functionalized with (3-Aminopropyl) triethoxysilane (APTES) by flowing a solution of 2% APTES in ethanol. This silane molecule covalently binds to Si atoms on the resonator surface and presents positively charged amine (NH_2) groups that aid the nonspecific adsorption and retention of BSA molecules. Both reference and probe resonators were exposed to the APTES solutions in order to maintain close spacing of the resonances. The microfluidic device was flushed with PBS before commencing the BSA flow experiments.

The reference flow was PBS. The probe flow was BSA diluted in PBS to a concentration of 100 fM. The dynamic resonance response of both the probe and reference channels as well as the difference signal are shown in Figure 5.14. The familiar resonance frequency blue shift is clearly seen in both the probe and reference responses. A periodic modulation, most likely related to the syringe pumps, is also plainly visible. Neither of these spurious resonance shifts appears in the differential signal. The frequency shift due to to the adsorption of BSA was 250 MHz after 12 minutes of exposure. It is difficult to attribute this frequency shift to a quantity of adsorbed

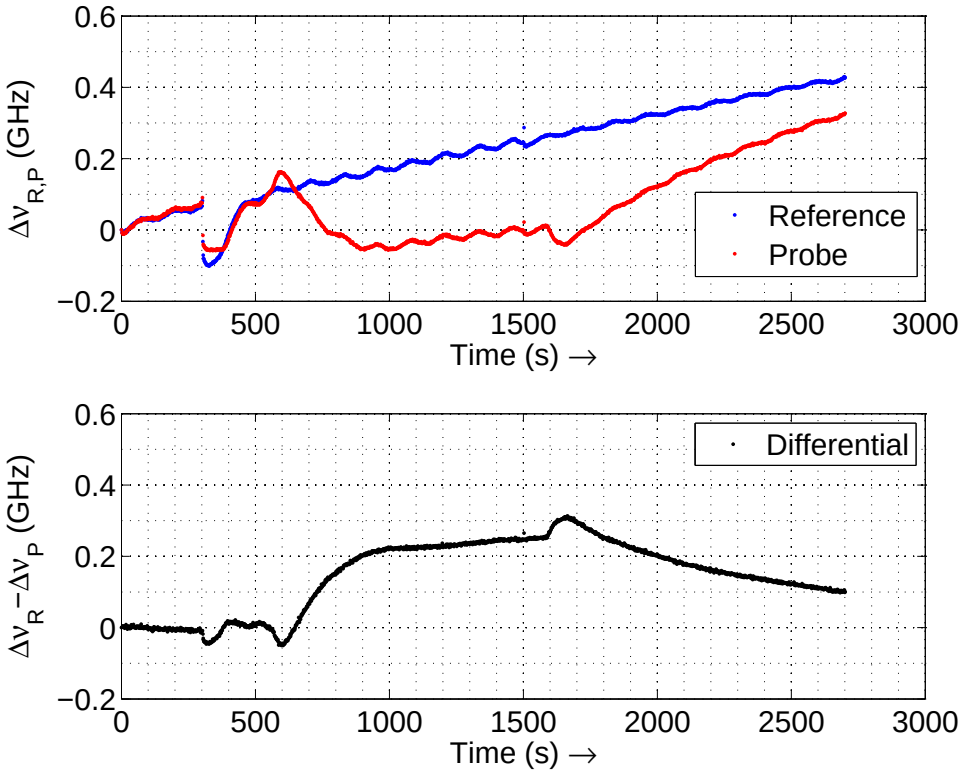

Figure 5.14: The dynamic resonance response of the dual resonator device to a 100 fM solution of BSA in PBS. The upper panel shows the resonance shift of both the reference and probe resonators. The lower panel shows the differential signal.

BSA. Resonator coverage is incomplete and studies on mass transfer and transport phenomena are beyond the scope of this work.

Chapter 6

Conclusion

6.1 Summary of the thesis

The goal of this work has been to introduce improvements to important aspects of label-free optical biosensing in order to usher the technique from a laboratory demonstration to a useful analytical and diagnostic tool. This has been accomplished via the avenues of the interrogating laser source, the refractive index transducer, and the analyte delivery system.

We have introduced a low cost, non-mechanical tunable laser source capable of producing highly linear broadband optical frequency sweeps. This optoelectronic swept frequency laser leverages the unique direct modulation (frequency-current) tuning characteristic of single section semiconductor laser diodes to produce optical chirps with bandwidths ranging from 100 GHz to 500 GHz and durations as short as 100 μs. An electronic feedback loop and predistorted drive current are used to linearize the slope of the frequency sweep and lock the starting frequency of successive sweeps. The precisely linear optical chirps generated by the SFL enable transmission spectroscopy measurements of the exact nature needed in label-free optical biosensing systems. We demonstrated using the SFL to perform label-free optical biosensing measurements with both microtoroid and microdisk optical resonators.

The potential of the SFL architecture to adapt to laser sources at shorter wavelengths is also a key advantage. An SFL source operating at a wavelength of 1064 nm is expected to allow operation of high-Q planar microdisk resonators beyond the wa-

ter absorption limit in an aqueous environment with the potential for detection limits near $\Delta n = 1 \times 10^{-7}$.

We have designed, fabricated, and demonstrated a high-Q planar integrated microdisk resonator and waveguide using a silicon nitride on silica material system. The resonators were designed to be highly flexible with respect to wavelength of operation, enabling a future transition to shorter wavelength lasers. Careful consideration was given to the resonator waveguide coupling physics. Designs were studied using a coupled mode approach in order to obtain critical coupling for the fundamental and higher radial order modes. We realized resonators with loaded Qs greater than 7×10^6. These are the highest quality factors reported for planar integrated microdisks on silicon nitride of this size at 1310 nm.

The planar on-chip resonator design was also shown to be friendly to microfluidic integration. PDMS microfluidic channels were fabricated using standard methods and bonded onto resonator chips enabling precise and controlled analyte fluid delivery. Using the integrated sensor device, we demonstrated bulk refractive index sensing, as well as specific and non specific adsorption of model proteins onto the resonator surface. The experimentally measured bulk refractive index response of the sensor was shown to be in excellent agreement with simulated values.

Lastly, but perhaps most importantly, we have conceived and implemented a differential measurement scheme to alleviate the sensing measurement from several considerable sources of noise and frequency drift. The differential measurement utilized two high-Q microdisk resonators coupled to the same bus waveguide within a dual laminar flow microfluidic channel. The unique properties of laminar flow were used to maintain separation of analyte and reference flows while both resonators were subjected to identical environmental drift factors including temperature, pressure, and flow cooling. Differential measurements were shown to significantly reduce measurement noise and improve the reliability and performance of bulk refractive index sensing measurements.

Overall, this work has made significant improvements in the implementation of an on-chip integrated label-free biosensing system. We have prepared the foundation

for future work using this platform and for the evolution of label-free sensing from a highly complex laboratory based assay to a powerful tool for life sciences research and medical diagnostics.

6.2 Future outlook

6.2.1 Covalent surface functionalization

The next major development necessary for the biosensing system to move towards practicality, is the development of a covalent chemistry for the functionalization of the resonator surface. The label-free sensing approach requires the immobilization of one half of a protein or biomolecule conjugate pair onto the active sensing surface of the silicon nitride microdisk resonator in order to capture the other half. Fortunately, there are are several well established chemical methods that can potentially be used to do so. Here we will briefly describe one of the more promising methods that is compatible with silica, and potentially silicon nitride.

The functionalization procedure has several steps and can be performed by flowing solutions through previously bonded microfluidic channels or by treating the resonator chip prior to bonding. The first step involves the deposition of an amino silane; either (3-Aminopropyl)triethoxysilane (APTES) or (3-aminopropyl)-trimethoxysilane (APTMS) can be used. These silane molecules react with hydroxyl (-OH) groups that form on the surface of the silicon nitride or oxide forming a covalent bond. Both APTES and APTMS are terminated with an amine (-NH_2) group allowing for further covalent bonds to be formed with many other functional groups including N-hydroxysuccinimide esters. APTES can be deposited on the resonator surface in the vapor phase, or by immersion in a 2% APTES in ethanol solution, or by flowing such a solution over the chip through a microfluidic channel. Depending on the type of assay desired, various heterobifunctional linking molecules can be intruduced to the chip to bind with the amine on one end and provide another different functional group to bind a biomolecule of choice. The heterobifunctional biolinker acts as a brige between the

amine terminated resonator surface and an antibody, single stranded DNA fragment or protien. The final step involves immobilization of the probe molecule. These surface functionalization steps are depicted in Figure 6.1.

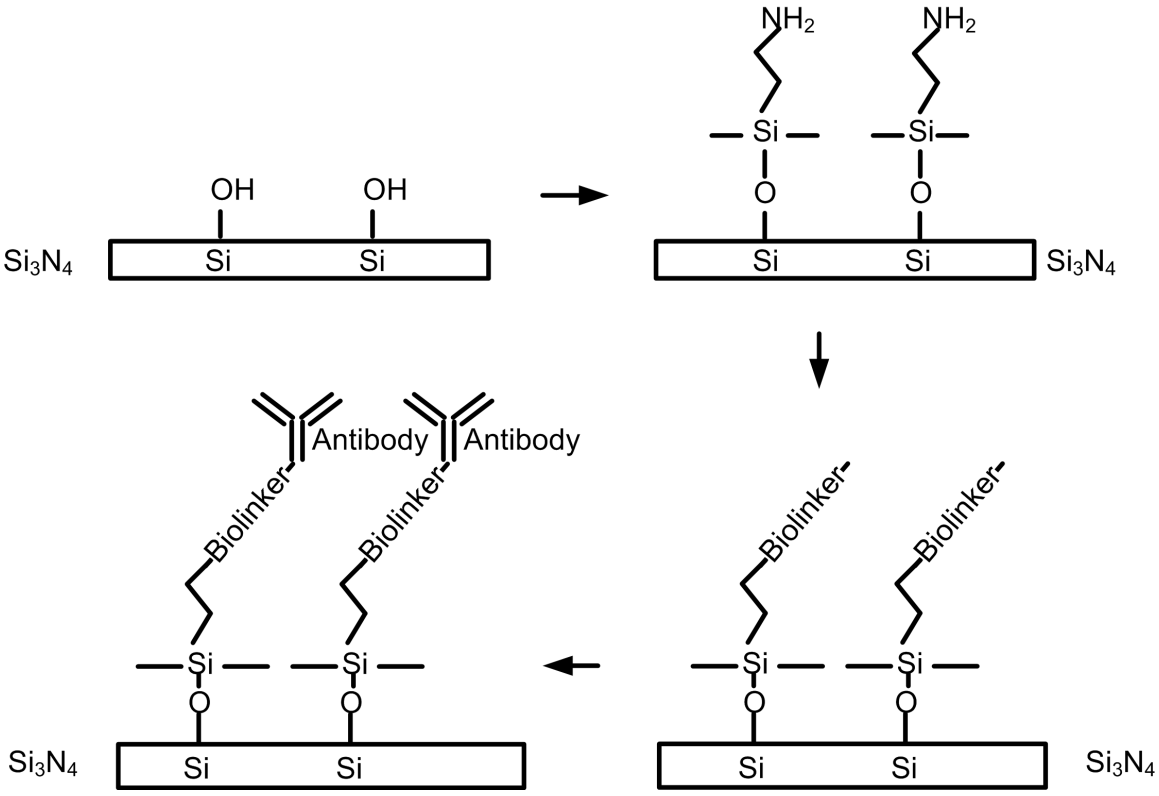

Figure 6.1: A diagram of the proposed covalent surface functionalization process.

6.2.2 Analyte transport efficiency

Measurement time is a critical parameter for a practical analytical or diagnostic instrument. The duration of measurements observed in Chapters 4 and 5 were on the order of an hour and need to be shortened. Limiting factors for sensing measurement duration included length of plumbing leading from syringe pumps to the microfluidic channel inlet, valve dead volume, and analyte diffusion within the flow channel. Dead volume and tubing length can be easily reduced by utilizing smaller valves, and closer placement of pumps and valves to the device. Alternatively, multilayer microfluidic systems can be implemented, integrating pumps and valves with the sensor chip [83].

A careful analysis of analyte transport within the channel is also necessary to improve measurement times. Laminar flow, a feature used to advantage in the dual flow differential measurement, increases measurement time by limiting dilute species' transport to diffusion. The microdisk resonator is located on the wall of the fluid channel well within the velocity boundary layer. Analyte molecules must therefore diffuse from the bulk fluid flow in the center of the channel through the boundary layer (≈ 2 μm thick) to the disk surface [84]. Turbulent mixing within a flow channel could be used to remove the diffusion bottle neck and decrease measurement times [83].

6.2.3 Wavelength of operation

As discussed in Chapter 4, optical absorption losses due to the aqueous sensing environment limit the loaded Q of the resonator and therefore the frequency resolution of the sensing measurement. The fabrication-limited Q in air has been measured to be nearly ten million. Moving the SFL wavelength to 1064 nm will result in an increase in the measured wet quality factor of nearly an order of magnitude. As shown in Table 4.1 the calculated water absorption Q at 1064 nm for the nitride microdisk used in this work is 8.6×10^6, on par with the loaded fabrication Q of the resonator in air. At such a value, water absorption ceases to be the dominant loss channel.

An SFL sources have been developed in parallel with this work using both DFB lasers and VCSELs with a nominal wavelength of 1064 nm. The transmission spectra of a nitride microdisk with both water and air environments measured using the 1064 nm SFL are shown in Figures 6.2a through 6.2d. The measured loaded wet Q determined by a Lorentzian fit is 1.7×10^6. This value should be compared to the loaded dry Q of 1.9×10^6 for a similar resonance on the same device prior to water immersion. The loaded wet quality factor measured here is the highest reported for a planar integrated optical mirco-resonator of any type at any wavelength by nearly two orders of magnitude.

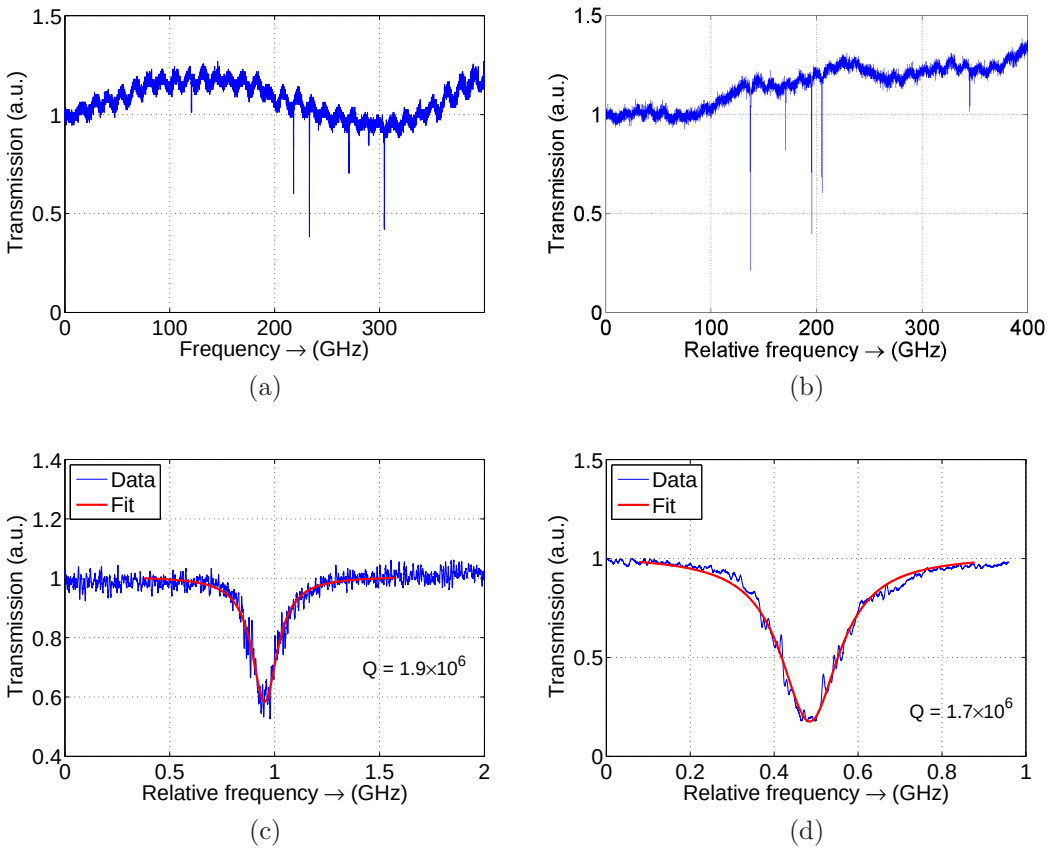

Figure 6.2: Transmission spectra from a silicon nitride microdisk resonator as measured with a 1064 nm optoelectronic swept frequency laser.(a) 400 GHz wide spectrum in an air environment, (b)400 GHz wide spectrum in a water environment,(c) detailed spectrum of a single resonance mode in an air environment, (d) detailed spectrum of a single resonance mode in a water environment.

Appendix A

Bandwidth enhancement of linearly chirped optical waves by four-wave mixing in nonlinear media

A.1 Introduction

Linear swept frequency laser sources have applications in three dimensional imaging and ranging [85], spectroscopy, [41] and sensing [86, 87]. The total range B (Hz) (bandwidth) of the frequency sweep is the key parameter in many of these applications. In linear chirp ranging and imaging, the axial resolution δz is related to B by [36]:

$$\delta z = \frac{c}{2B}. \tag{A.1}$$

It is clear from Equation A.1 that swept frequency lasers with larger chirp bandwidths enable the resolution of smaller features in frequency modulated continuous wave (FMCW) imaging systems. Many laser systems for generating large frequency sweeps have been demonstrated including those using Fourier domain mode locking [22] and rotating polygonal mirrors within the laser cavity [23]. Though these laser systems have large optical tuning bandwidths and therefore high axial resolution, they suffer from low coherence length, limiting the range in which they can be used to several centimeters. The mechanical nature of the tuning mechanism also limits the robustness of these lasers. Additionally, the frequency sweeps generated

by such lasers are not linear and extensive post processing is necessary to correct the nonlinearity and compose a target image.

Previously, we have demonstrated the generation of broadband precisely linear optical frequency sweeps using a semiconductor laser in an optoelectronic phase-lock loop [24]. This approach takes advantage of the electronic tunability of semiconductor DFB lasers and VCSELs to construct light sources with frequency sweeps of up to 500 GHz in 100 μs. From Eq.(A.1) this provides an axial resolution of 300 μm in air.

Some imaging applications, including optical coherence tomography (OCT), are aimed at imaging biological structures [88] and require axial resolutions on the order of 15 μm corresponding to a chirp bandwidth of 10 THz. It is therefore desirable to increase the chirp bandwidth of the optoelectronic swept frequency laser (SFL). This can be accomplished using multiple SFLs covering adjacent frequency bands and stitching together the resultant signals in post processing similar to synthetic aperture radar [39]. Another method for increasing the bandwidth of the optoelectronic SFL is to perform chirp multiplication by taking advantage of the nonlinear optical effect of four wave mixing (FWM) [40]. The doubling of high bandwidth input chirps via FWM is the subject of this appendix.

FWM can occur in a variety of materials including specialty highly nonlinear silica optical fibers (NLF), integrated optical waveguides, and semiconductor optical amplifiers (SOAs) amongst other media. Here, we will discuss FWM in NLF and preliminary work on chirp doubling by FWM in silicon waveguides on chip.

A.2 FWM in NLF

Nonlinear optical fibers (NLF) exhibit four-wave optical interaction. The nonlinear gain γ in these fibers is roughly an order of magnitude greater than in standard single mode optical fiber (SMF) ($\gamma = 11.3$ km^{-1}W^{-1} in NLF). Given two input fields to a length of NLF, it can be shown that the power generated in the FWM output is given by

$$P_{out}(L) = \gamma^2 P_{ch}^2 P_R e^{-\alpha L} \left(\frac{1 - e^{-\alpha L}}{\alpha} \right)^2 \frac{\alpha^2}{\alpha^2 + \Delta\beta^2} \left(1 + \frac{4e^{-\alpha L} \sin^2 \frac{\Delta\beta L}{2}}{(1 - e^{-\alpha L})^2} \right), \qquad \text{(A.2)}$$

where α is the loss per unit length and $\Delta\beta = 2\beta_{ch} - \beta_R - \beta_{out}$ which, to lowest order in $\Delta\omega$ can be written as $\Delta\beta = -\beta_2 \Delta\omega^2$, where $\Delta\omega$ is the frequency difference between the chirped and reference waves [40]. It is clear from Equation A.2 that the phase mismatch $\Delta\beta$ between the three waves, E_{ch}, E_R, andE_{out} has a large effect on the FWM output power generated at the end of a fiber. Using the group velocity dispersion (GVD) parameter $\beta_2 = -\lambda^2 D_c / 2\pi c$, we can show that $\Delta\beta = -\lambda^2 D_c \Delta\omega^2 / 2\pi c$. In order to achieve large nonlinear gain, NLF fibers with lengths of 100 m and dispersion parameters of less than 1 ps/nm-km were used. As seen in Figure A.1, even in these low dispersion fibers the phase mismatch accrued between the the input chirp and reference fields at large frequency differences over 100 m of fiber hinders the FWM process.

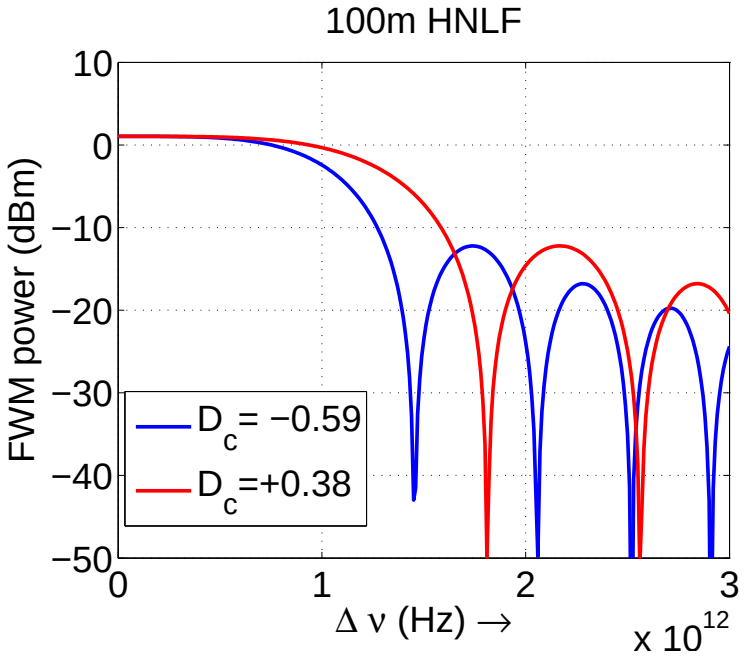

Figure A.1: A comparison of the conversion efficiency spectra of 100 m segments of NLF with different dispersion coefficients. In both cases the chirp and reference input powers are 100 mW and $\gamma = 11.3$ km^{-1}W^{-1}

To double a chirp of bandwidth B, the minimum separation between the frequency of the reference wave ω_R and the starting frequency of the chirped wave ω_{ch0} is B. This ensures that chirp doubled output frequency, given by $\omega_{out} = 2\omega_{ch0} - \omega_R$, does not overlap with the input chirp. Consider an input chirp with a bandwidth of 500 GHz. The frequency separation is 500 GHz at the start of the chirp and 1 THz at the end of the chirp. From Figure A.1 it is clear that the amplitude of the FWM output will be modulated by the nonuniform conversion efficiency and could even have nulls for certain values of D_c. To efficiently double high bandwidth chirps, it is necessary to employ a nonlinear medium with a larger conversion efficiency bandwidth. One way to do this in NLF is to use the technique of quasi phase matching via dispersion compensation.

A.3 FWM with QPM NLF

A.3.1 Theory

Quasiphase matching (QPM), is a method of dispersion compensation that utilizes short fiber segments of alternating dispersion (β_2) sign to construct a single long fiber with low dispersion and therefore a low phase mismatch. This enables a QPM NLF to achieve a long nonlinear interaction length while maintaining a large conversion efficiency bandwidth.

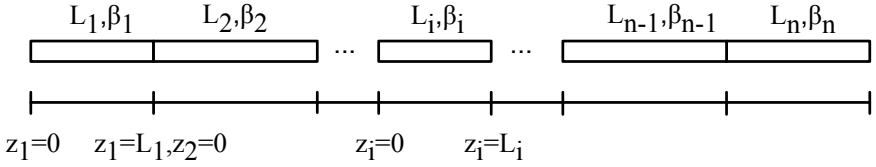

Figure A.2: A multiple segment nonlinear waveguide for FWM

Consider a fiber that is composed of n segments, each with length L_n and propagation constants $\beta_{ch,n}, \beta_{R,n}$, and $\beta_{out,n}$. We can define a new reference frame in each segment

$$z_n = z - \sum_{i=1}^{n-1} L_i. \tag{A.3}$$

The differential equation that describes the evolution of the FWM output field amplitude, A_{out}, is still valid and it can be shown that the output field at the end of the nth segment is given by

$$A'_{out,n}(L_n) = A'_{out,n-1}(L_{n-1})e^{-\alpha L_n/2} - j\xi A^2_{ch,1}(0)A^*_{R,1}(0)\exp\left(-j\sum_{i=1}^{n-1}\Delta\beta_{out,i}L_i\right) \times \exp\left(-\frac{3\alpha}{2}\sum_{i=1}^{n-1}L_i - \frac{\alpha L_n}{2}\right)\left(\frac{1-e^{-(\alpha+j\Delta\beta_n)L_n}}{\alpha+j\Delta\beta_n}\right), \quad (A.4)$$

where $\xi = nc\epsilon_0\gamma A_{eff}/2$. Expression A.4 is valid up to an overall phase factor. The FWM output power is therefore given by

$$P_{out}\left(\sum_{i=1}^{N}L_i\right) = \frac{1}{2}\left(\frac{\epsilon_0}{\mu_0}\right)^{1/2} nA_{eff}\left|A'_{out,N}\left(L_N\right)\right|^2. \quad (A.5)$$

From Equations A.4 and A.5 we see that the FWM output bandwidth is determined by the phase mismatch, and therefore the length and dispersion, of the individual segments of the fiber and not of the total length of the fiber. Figure A.3 demonstrates the bandwidth advantage of a QPM fiber over a single segment fiber.

Consider a 500 GHz input chirp with the minimum offset of 500 GHz. The fiber, QPM or single segment would require a minimum 3dB conversion efficiency bandwidth of 1 THz and provide enough FWM power to make the chirp doubled output usable. From Figure A.3 it is clear that the $4 \times 50\ m$ QPM fiber is the best choice of those shown.

A.3.2 Experimental results

We measured the conversion efficiency spectrum of both a QPM fiber comprising two 100 m segments of NLF with alternate dispersion coefficient signs and a QPM comprising four 50 m segments of NLF with alternating dispersion signs. We also performed chirp doubling of a 500 GHz input chirp to obtain a 1 THz output chirp using the four 50 m segment QPM fiber. The nonlinear fibers used to construct

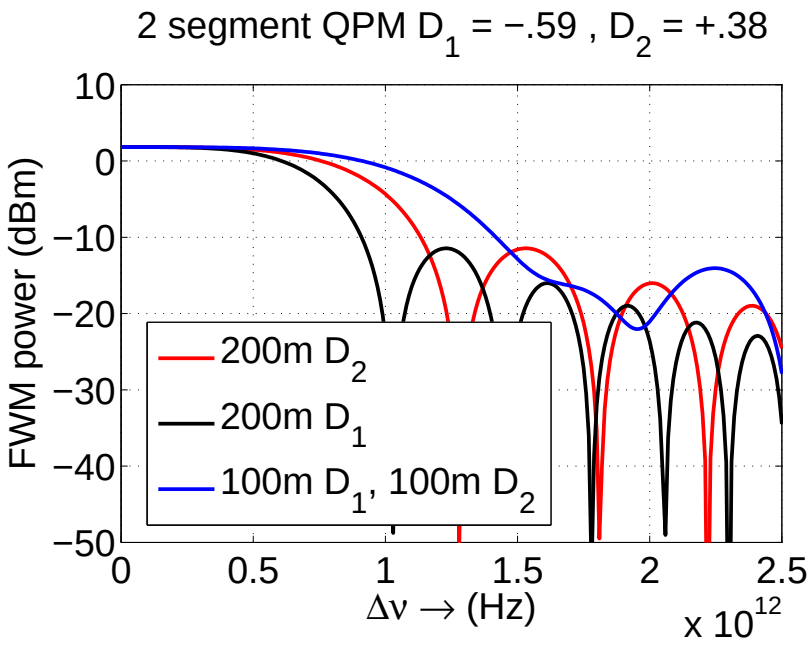

(a)

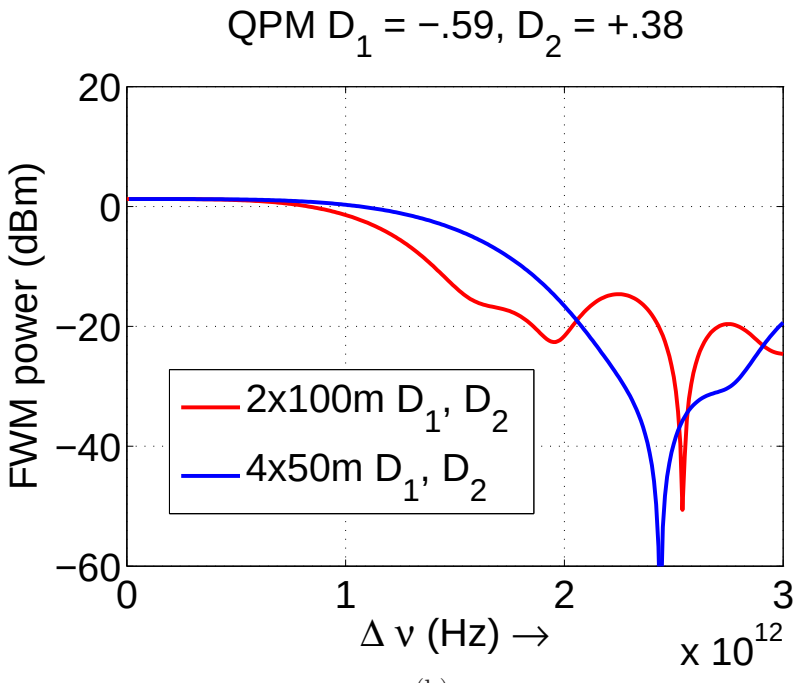

(b)

Figure A.3: Theoretical conversion efficiency spectra (a) demonstrating bandwidth advantage of a two segment QPM fiber over a single non-QPM fiber of the same length, (b) demonstrating the bandwidth advantage of four shorter segments over two segments

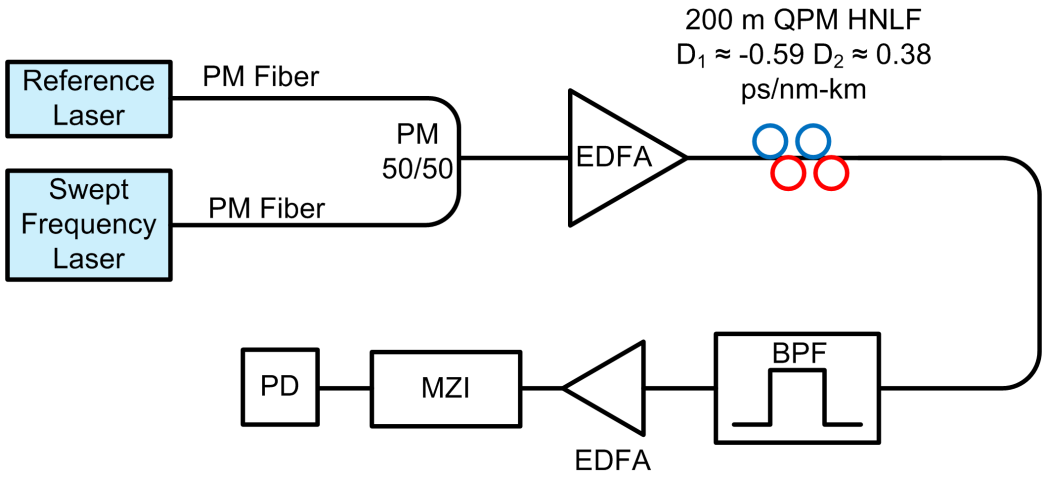

Figure A.4: Schematic diagram of the experimental setup for chirp bandwidth doubling in QPM NLF. EDFA: Erbium doped fiber amplifier, BPF: Band pass filter, MZI: Mach-Zehnder interferometer, PD: Photodetector

the QPM fiber were dispersion flattened NLF manufactured by OFS. The NLF had $\gamma = 11.3$ km^{-1}W^{-1} and $\alpha = 1$ dB/km. The dispersion parameters of the two 100 m parent fibers were $D_1 = -0.59$ ps/nm $-$ km and $D_2 = +0.38$ ps/nm $-$ km. QPM fiber was constructed using a fusion splicer to minimize losses. Both QPM fibers had SMF pigtails with FC/APC connectors.

To measure the conversion efficiency spectrum of the fibers, we used an experimental setup similar to that of Figure A.4 where the output of the fiber was fed into an optical spectrum analyzer (OSA). A 20 dB attenuator was used at the OSA input to avoid damage to the instrument. A CW VCSEL with a nominal wavelength of 1550 nm was used as a reference while an Agilent tunable laser was tuned from a frequency separation of 0 to 2.2 THz. The power of the FWM product waves was measured using the OSA. Typical input powers for both the chirped and reference waves were on the order of 100 mW.

The conversion efficiency spectra of the two QPM fibers is shown in Figure A.5. The theoretical predictions and the experimentally measured values are in good agreement for both fibers for detuning values up to 1.5 THz. At larger detuning values, the effects of higher order dispersion, which are not included in the theoretical model, cause the deviation between experiment and theory.

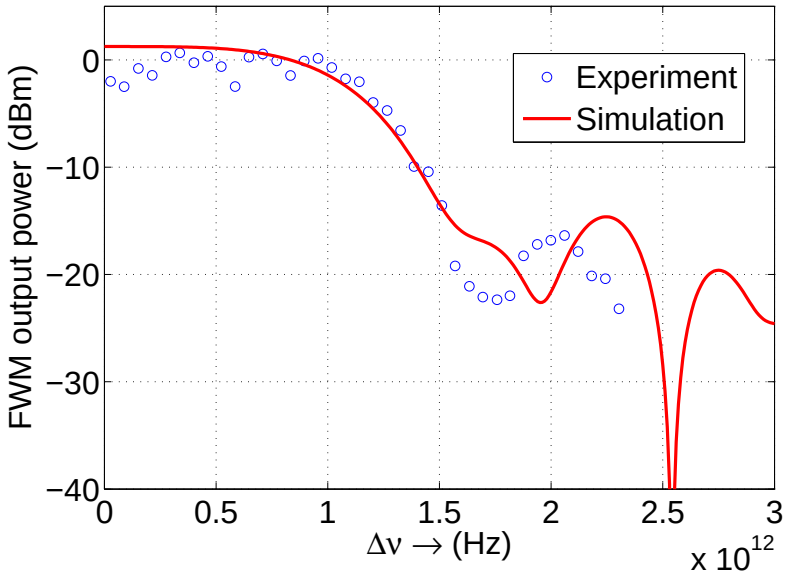

(a)

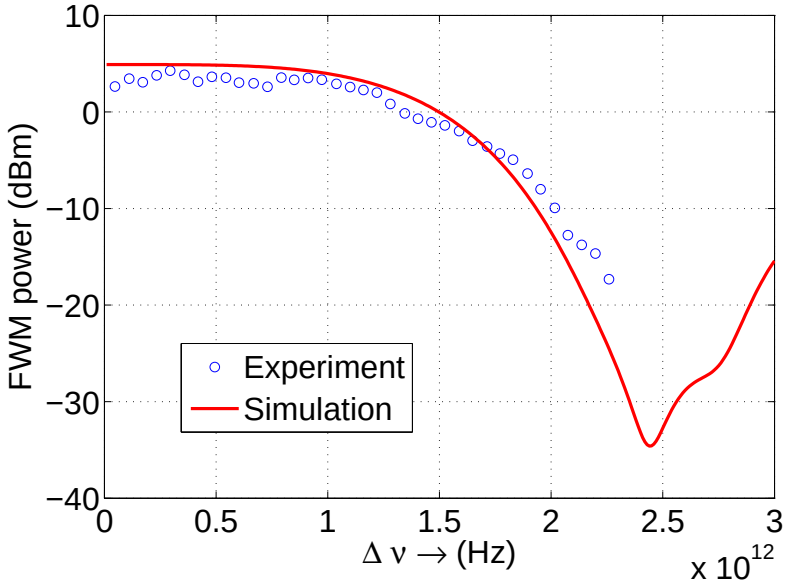

(b)

Figure A.5: Experimental measurement of the conversion efficiency spectrum of (a) two segment QPM NLF and (b) four segment QPM NLF. In both arrangements, the total fiber length is approximately 200 m.

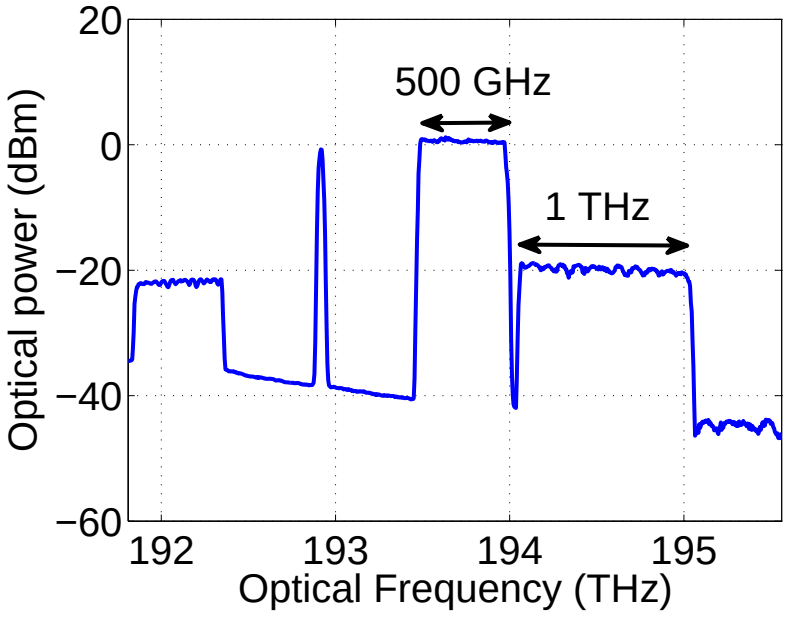

(a)

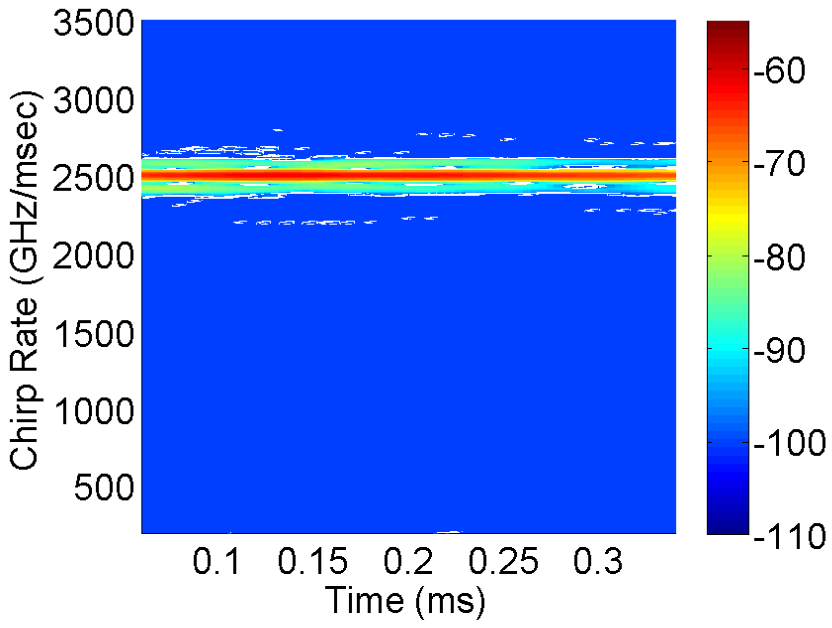

(b)

Figure A.6: (a)Experimental demonstration of chirp doubling in a four segment QPM NLF and (b) the spectrogram of photocurrent of the filtered FWM output. The total length of the fiber is approximately 200m. $P_{ch} = 100$ mW and $P_R = 100$ mW.

We also performed a chirp doubling experiment using the four 50 m segment QPM NLF fiber. The input chirp field was produced by a VCSEL based optoelectronic swept frequency laser. This SFL produced linear frequency sweeps of 500 GHz over 400 μs. The CW reference field was provided by an TLD. The output optical spectrum in Figure A.6(a) clearly shows the 500 GHz input chirp and the 1 THz output chirp. To demonstrate the linearity of the chirp doubled output, the FWM output was filtered from the input chirp and reference fields. This output was amplified by a telecom EDFA to compensate for losses from the filtering process and measured using a Mach-Zehnder interferometer and photodetector. The spectrogram of the filtered output chirp in Figure A.6(b) shows the constant sweep rate of the chirp doubled output at 1 THz/400 μs.

A.4 FWM in integrated silicon waveguides

Silicon on insulator (SOI) waveguides have been used to demonstrate wavelength conversion [89–91] and parametric amplification [92] via four wave mixing on chip. Silicon is a strongly nonlinear material and has been shown to possess a nonlinear index coefficient that is several orders of magnitude greater than that of silica. The effective mode area of silicon waveguides is also much smaller than that of nonlinear silica fibers. This enables the use of relatively short SOI waveguides with lengths on the order of 1 cm to achieve the nonlinear gain of hundreds of meters of NLF. Additionally, the group velocity dispersion (GVD) of SOI waveguides can be engineered via the waveguide dimensions to achieve low dispersion and therefore large FWM conversion efficiency bandwidths enabling the efficient doubling of high bandwidth linear chirps on chip. Here, we present some preliminary work in this area demonstrating the wide conversion efficiency bandwidth of 7.5 mm long SOI waveguides and optical spectra showing chirp doubling.

A.4.1 Device design and fabrication

The nonlinear gain coefficient γ of a waveguide or fiber is given by

$$\gamma = \frac{n_2 \omega_0}{c A_{eff}}, \tag{A.6}$$

where n_2 is the nonlinear refractive index coefficient of the material, and A_{eff} is the effective area of the waveguide. From Equation A.6 it is clear that minimizing the effective area of the waveguide will result in a larger nonlinear gain allowing for shorter device lengths. As in the case of NLF, shorter waveguides will also result in a larger FWM conversion efficiency bandwidth due to smaller phase mismatch.

Assuming a waveguide thickness of 220nm (the thickness of the Si device layer in our SOI wafer) and a 2 μm thick silica upper cladding layer, we simulated the mode profiles of various single mode wave guides with widths varying from 360 nm to 560 nm in Comsol. Waveguides with widths larger than 440 nm are above the single mode cutoff and are not of practical use but were included to illustrate the effect of waveguide width on effective area. In our calculations we set the nonlinear index $n_2 = 4 \times 10^{-18}$ m^2/W. This has been shown to be in good agreement with experimental results from similar silicon waveguide structures [91]. From Figure A.7 (b) we see that as the core of the waveguide becomes wider, the optical mode is more confined to the silicon and the effective mode area decreases. If we design our waveguide to be 440 nm wide, we can achieve the smallest effective area (while maintaining a single mode waveguide), and therefore the highest nonlinear gain. In this case $\gamma = 89250$ km^{-1}W^{-1}.

In silicon waveguides, the majority of the dispersion is a result of waveguide dispersion. We simulated the modes of waveguides of several widths over the range of wavelengths 1537–1570 nm to compute the propagation constant $\beta(\omega)$. Material dispersion was incorporated into the simulations using the Sellmeier model for the refractive index of both the silicon core and silica cladding. The dispersion coefficient for the waveguide is then given by $D_c = -2\pi c \beta_2 / \lambda^2$, where β_2 is the second derivative of $\beta(\omega)$ with respect to ω.

From Figure A.8 we can see that as the waveguide width increases, the dispersion decreases. Again, we are limited by the single mode criteria to a width of 440 nm

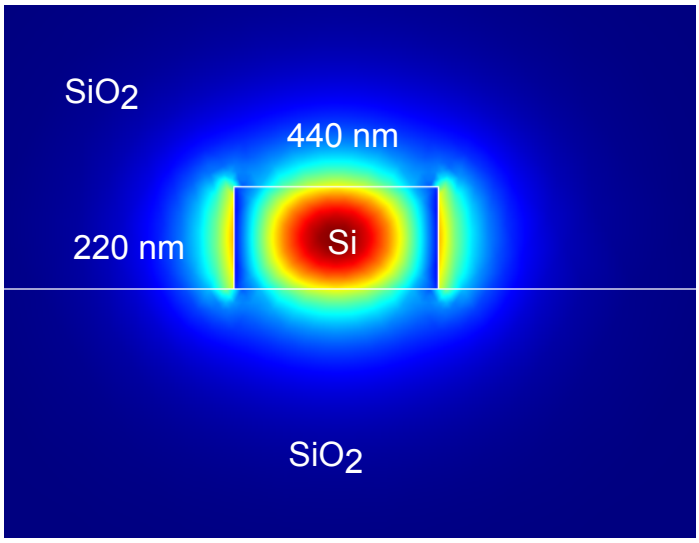

(a)

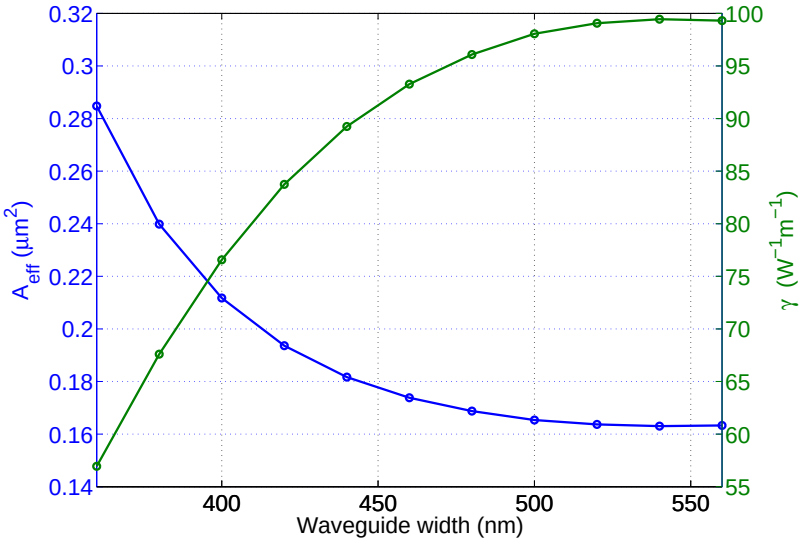

(b)

Figure A.7: (a) Mode profile of a single mode Si ridge waveguide with dimensions 440 nm×220 nm. (b) The effective area A_{eff} and nonlinear coefficient γ of the of Si ridge waveguides as a function of waveguide width. For waveguide larger than 440 nm wide (the single mode cutoff) the values shown are for the fundamental mode

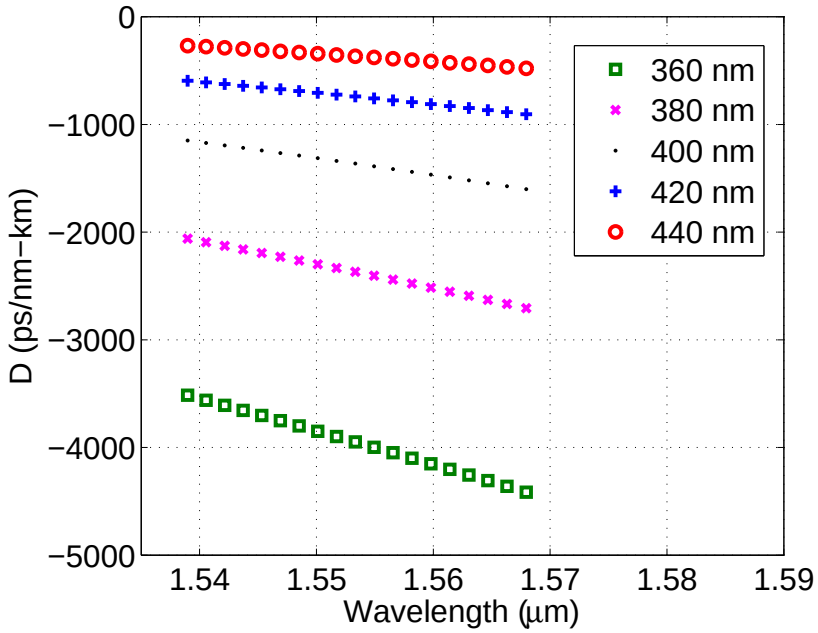

Figure A.8: The dispersion parameter D_c as a function of wavelength for 220 nm thick silicon waveguides with a 2μm silica upper cladding. The width of each waveguide is given in the legend.

which provides a dispersion parameter in this wavelength range of -600 to -900 ps/nm-km.

We fabricated 7.5 mm long silicon waveguides using 220 nm thick SOI. Waveguide widths between 300 nm and 440 nm were designed. However, due to fabrication issues the actual waveguide widths were narrower. Inverse taper spot size converters were designed and implemented to minimize input and output coupling losses. The devices were patterned using electron beam lithography. A short oxygen plasma "resist trimming" step was used to reduce e-beam resist sidewall roughness. The devices were dry etched using a combination of C_4F_8 and SF_6 in an ICP RIE etcher. The silica upper cladding was deposited using PECVD.

A.4.2 Experimental results

Using an experimental setup similar to that in Figure A.4 we measured the FWM conversion efficiency as a function of the detuning between the pump and signal waves.

The conversion efficiency spectrum is shown in Figure A.9 (a).

From Figure A.4 (a) we can clearly see a 3 dB bandwidth greater than 1.75 THz which is more than enough to perform chirp doubling with 500 GHz bandwidth input chirps. For pump signal detuning values less than 1 THz there is good agreement between theory and experiment. However, the theoretical calculation does not include higher order dispersion terms which are responsible for the earlier than expected roll off in conversion efficiency observed in the experimental results.

Using a linearly chirped pump wave and CW signal wave, we observed chirp doubling in the output optical spectrum of the silicon waveguide. The output power of the EDFA was 700 mW; however, due to the input coupling losses, the input power of the silicon waveguide is not known. The conversion efficiency achieved was aproximately -28 dB. This can easily be improved by increasing the power of the pump (chirped wave) and by increasing the length of the waveguide and increasing the input power of the pump (chirped) wave. Further improvements of the input and output coupling alignment will also improve the conversion efficiency of the chirp doubled output. The large noise floor visible in Figure A.9 is present due to the use of an extra SOA to boost the optical power of the chirped VCSEL laser prior to the high power EDFA. A tunable bandpass filter can be used after the EDFA to minimize the effect and presence of ASE noise in the FWM process. The “horns” observed in Figure A.9 (b) are an artifact from the OSA measurement and do not represent actual increased optical power at the band edges of the SFL.

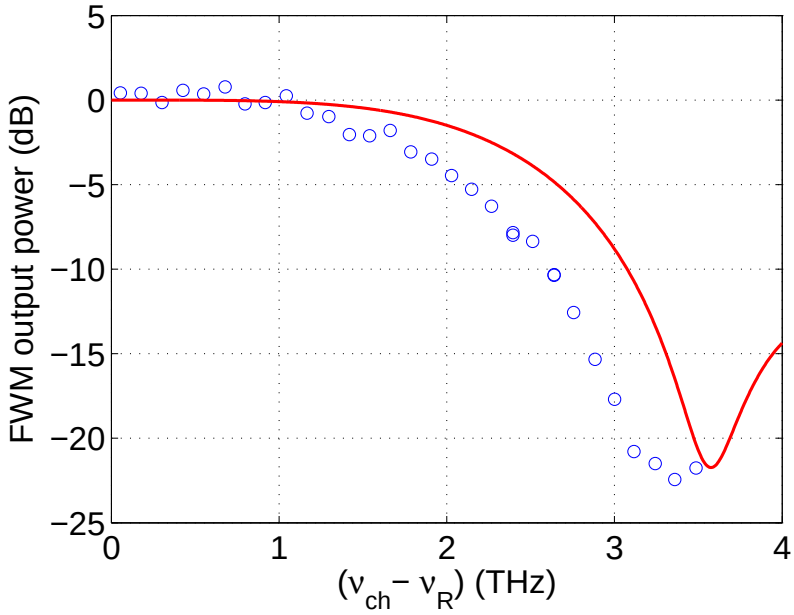

(a)

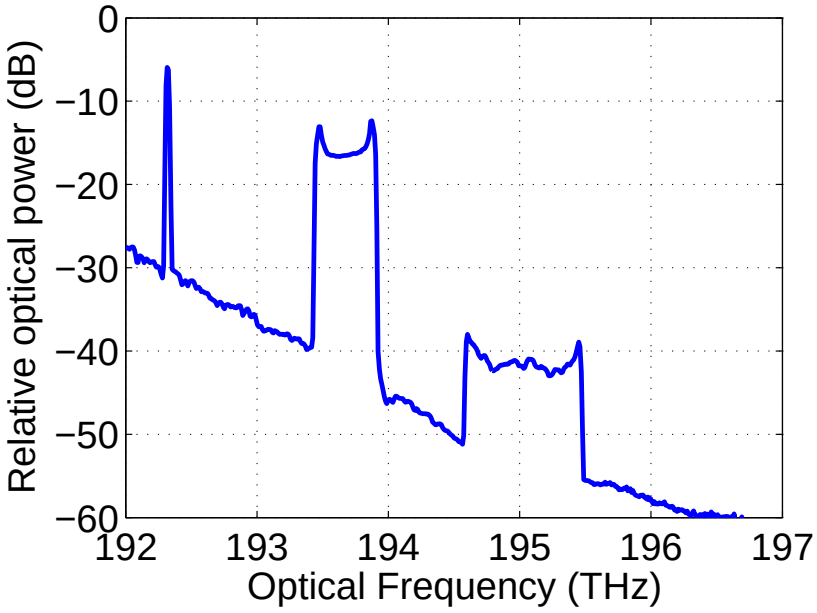

(b)

Figure A.9: (a) The normalized conversion efficiency spectrum of a 400 nm × 220 nm SOI waveguide at a nominal wavelength of 1550 nm. Blue circles are experimental data, red line is theoretical simulation. (b) The output optical spectrum of the same waveguide using a 500 GHz in 400 μs linear chirp as the pump wave, with a CW signal wave.

Bibliography

[1] G. M. Hale and M. R. Querry, "Optical constants of water in the 200-nm to 200-μm wavelength region," *Applied Optics*, vol. 12, pp. 555–563, Mar 1973.

[2] Y. H. Kim, S. J. Park, S.-W. Jeon, S. Ju, C.-S. Park, W.-T. Han, and B. H. Lee, "Thermo-optic coefficient measurement of liquids based on simultaneous temperature and refractive index sensing capability of a two-mode fiber interferometric probe," *Optics Express*, vol. 20, pp. 23744–23754, Oct 2012.

[3] J. Teng, P. Dumon, W. Bogaerts, H. Zhang, X. Jian, X. Han, M. Zhao, G. Morthier, and R. Baets, "Athermal silicon-on-insulator ring resonators byoverlaying a polymer cladding on narrowedwaveguides," *Opt. Express*, vol. 17, pp. 14627–14633, Aug 2009.

[4] K. B. Gylfason, C. F. Carlborg, A. Kazmierczak, F. Dortu, H. Sohlström, L. Vivien, C. A. Barrios, W. van der Wijngaart, and G. Stemme, "On-chip temperature compensation in an integrated slot-waveguide ringresonator refractive index sensor array," *Opt. Express*, vol. 18, pp. 3226–3237, Feb 2010.

[5] I. Goykhman, B. Desiatov, and U. Levy, "Ultrathin silicon nitride microring resonator for biophotonic applications at 970 nm wavelength," *Applied Physics Letters*, vol. 97, Aug 2010.

[6] M. Iqbal, M. Gleeson, B. Spaugh, F. Tybor, W. Gunn, M. Hochberg, T. Baehr-Jones, R. Bailey, and L. Gunn, "Label-free biosensor arrays based on silicon ring resonators and high-speed optical scanning instrumentation," *Selected Topics in Quantum Electronics, IEEE Journal of*, vol. 16, pp. 654 –661, May-June 2010.

[7] S. M. Grist, S. A. Schmidt, J. Flueckiger, V. Donzella, W. Shi, S. T. Fard, J. T. Kirk, D. M. Ratner, K. C. Cheung, and L. Chrostowski, "Silicon photonic microdisk resonators for label-free biosensing," *Optics Express*, vol. 21, pp. 7994–8006, Apr 2013.

[8] K. B. Gylfason, C. F. Carlborg, A. Kazmierczak, F. Dortu, H. Sohlstrom, L. Vivien, C. A. Barrios, W. van der Wijngaart, and G. Stemme, "On-chip temperature compensation in an integrated slot-waveguide ring resonator refractive index sensor array," *Optics Express*, vol. 18, pp. 3226–3237, Feb 2010.

[9] A. Voller, A. Bartlett, and D. Bidwell, "Enzyme Immunoassays with Special Reference to ELISA Techniques," *Journal of Clinical Pathology*, vol. 31, no. 6, pp. 507–520, 1978.

[10] J. Homola, S. Yee, and G. Gauglitz, "Surface plasmon resonance sensors: review," *Sensors and Actuators B-Chemical*, vol. 54, pp. 3–15, Jan 1999.

[11] X. Fan, I. M. White, S. I. Shopova, H. Zhu, J. D. Suter, and Y. Sun, "Sensitive optical biosensors for unlabeled targets: A review," *Analytica Chimica Acta*, vol. 620, no. 12, pp. 8 – 26, 2008.

[12] A. M. Armani, R. P. Kulkarni, S. E. Fraser, R. C. Flagan, and K. J. Vahala, "Label-free, single-molecule detection with optical microcavities," *Science*, vol. 317, pp. 783–787, Aug 2007.

[13] F. Vollmer, S. Arnold, and D. Keng, "Single virus detection from the reactive shift of a whispering-gallery mode," *Proceedings of the National Academy of Sciences of the United States of America* , vol. 105, pp. 20701–20704, Dec 2008.

[14] T. Lu, H. Lee, T. Chen, S. Herchak, J.-H. Kim, S. E. Fraser, R. C. Flagan, and K. Vahala, "High sensitivity nanoparticle detection using optical microcavities," *Proceedings of the National Academy of Sciences of the United States of America* , vol. 108, pp. 5976–5979, Apr 2011.

[15] S. Arnold, M. Khoshsima, I. Teraoka, S. Holler, and F. Vollmer, "Shift of whispering-gallery modes in microspheres by protein adsorption," *Optics Letters*, vol. 28, pp. 272–274, Feb 2003.

[16] S. I. Shopova, R. Rajmangal, Y. Nishida, and S. Arnold, "Ultrasensitive nanoparticle detection using a portable whispering gallery mode biosensor driven by a periodically poled lithium-niobate frequency doubled distributed feedback laser," *Review of Scientific Instruments*, vol. 81, Oct 2010.

[17] F. Vollmer, D. Braun, A. Libchaber, M. Khoshsima, I. Teraoka, and S. Arnold, "Protein detection by optical shift of a resonant microcavity," *Applied Physics Letters*, vol. 80, pp. 4057–4059, May 2002.

[18] E. Chow, A. Grot, L. Mirkarimi, M. Sigalas, and G. Girolami, "Ultracompact biochemical sensor built with two-dimensional photonic crystal microcavity," *Optics Letters*, vol. 29, pp. 1093–1095, May 2004.

[19] A. L. Washburn, L. C. Gunn, and R. C. Bailey, "Label-Free Quantitation of a Cancer Biomarker in Complex Media Using Silicon Photonic Microring Resonators," *Analytical Chemistry*, vol. 81, pp. 9499–9506, Nov 2009.

[20] A. Nitkowski, A. Baeumner, and M. Lipson, "On-chip spectrophotometry for bioanalysis using microring resonators," *Biomedical Optics Express*, vol. 2, pp. 271–277, Feb 2011.

[21] S. Yegnanarayanan, W. Roman, M. Soltani, G. Cremona, H. Lu, and A. Adibi, "On-chip integration of microfluidic channels with ultra-high Q silicon microdisk resonators for lab-on-a-chip sensing applications," in *2007 IEEE LEOS Annual Meeting Conference Proceedings, Vols 1 and 2*, IEEE Lasers and Electro-Optics Society (LEOS) Annual Meeting, pp. 50–51, 2007. 20th Annual Meeting of the IEEE-Lasers-and-Electro-Optics-Society, Lake Buena Vista, FL, OCT 21-25, 2007.

[22] R. Huber, M. Wojtkowski, and J. G. Fujimoto, "Fourier domain mode locking (fdml): A new laser operating regime and applications for optical coherence tomography," *Optics Express*, vol. 14, pp. 3225–3237, Apr 2006.

[23] S. H. Yun, C. Boudoux, G. J. Tearney, and B. E. Bouma, "High-speed wavelength-swept semiconductor laser with a polygon-scanner-based wavelength filter," *Optics Letters*, vol. 28, pp. 1981–1983, Oct 2003.

[24] N. Satyan, A. Vasilyev, G. Rakuljic, V. Leyva, and A. Yariv, "Precise control of broadband frequency chirps using optoelectronic feedback," *Optics Express*, vol. 17, pp. 15991–15999, Aug 2009.

[25] T. Squires and S. Quake, "Microfluidics: Fluid physics at the nanoliter scale," *Reviews of Modern Physics*, vol. 77, pp. 977–1026, Jul 2005.

[26] W. Liang, N. Satyan, A. Yariv, A. Kewitsch, G. Rakuljic, F. Aflatouni, H. Hashemi, and J. Ungar, "Coherent power combination of two master-oscillator-power-amplifier (mopa) semiconductor lasers using optical phase lock loops," *Optics Express*, vol. 15, pp. 3201–3205, Mar 2007.

[27] N. Satyan, W. Liang, and A. Yariv, "Coherence cloning using semiconductor laser optical phase-lock loops," *Quantum Electronics, IEEE Journal of*, vol. 45, no. 7, pp. 755 –761, 2009.

[28] N. Satyan, W. Liang, A. Kewitsch, G. Rakuljic, and A. Yariv, "Coherent power combination of semiconductor lasers using optical phase-lock loops," *Selected Topics in Quantum Electronics, IEEE Journal of*, vol. 15, no. 2, pp. 240 –247, 2009.

[29] G. Pandian and S. Dilwali, "On the Thermal FM Response of a Semiconductor Laser Diode ," *Photonics Technology Letters*, vol. 4, pp. 130–133, Feb 1992.

[30] P. Correc, O. Girard, and I. Defaria, "On the Thermal Contribution to the FM Response of DFB Lasers - Theory and Experiment," *Journal of Quantum Electronics*, vol. 30, pp. 2485–2490, Nov 1994.

[31] K. Iiyama, L.-T. Wang, and K.-I. Hayashi, "Linearizing optical frequency-sweep of a laser diode for fmcw reflectometry," *Lightwave Technology, Journal of*, vol. 14, pp. 173 –178, Feb 1996.

[32] W. Sorin, K. Chang, G. Conrad, and P. Hernday, "Frequency domain analysis of an optical fm discriminator," *Lightwave Technology, Journal of*, vol. 10, pp. 787 –793, Jun 1992.

[33] J. O. White, A. Vasilyev, J. P. Cahill, N. Satyan, O. Okusaga, G. Rakuljic, C. E. Mungan, and A. Yariv, "Suppression of stimulated Brillouin scattering in optical fibers using a linearly chirped diode laser," *Optics Express*, vol. 20, pp. 15872–15881, Jul 2012.

[34] N. Satyan, A. Vasilyev, G. Rakuljic, J. O. White, and A. Yariv, "Phase-locking and coherent power combining of broadband linearly chirped optical waves," *Optics Express*, vol. 20, pp. 25213–25227, Nov 2012.

[35] S. Chinn, E. Swanson, and J. Fujimoto, "Optical coherence tomography using a frequency-tunable optical source," *Optics Letters*, vol. 22, pp. 340–342, Mar 1997.

[36] W. Burdic, *Radar signal analysis*. Prentice-Hall electrical engineering series, Prentice-Hall, 1968.

[37] R. Motaghiannezam, D. M. Schwartz, and S. E. Fraser, "In Vivo Human Choroidal Vascular Pattern Visualization Using High-Speed Swept-Source Optical Coherence Tomography at 1060 nm," *Investigative Opthalmology & Visual Science*, vol. 53, pp. 2337–2348, Apr 2012.

[38] S. H. Yun, G. J. Tearney, B. J. Vakoc, M. Shishkov, W. Y. Oh, A. E. Desjardins, M. J. Suter, R. C. Chan, J. A. Evans, I.-K. Jang, N. S. Nishioka, J. F. de Boer, and B. E. Bouma, "Comprehensive volumetric optical microscopy in vivo," *Nature Medicine*, vol. 12, pp. 1429–1433, Dec 2006.

[39] A. Vasilyev, N. Satyan, S. Xu, G. Rakuljic, and A. Yariv, "Multiple source frequency-modulated continuous-wave optical reflectometry: theory and experiment," *Applied Optics*, vol. 49, pp. 1932–1937, Apr 2010.

[40] N. Satyan, G. Rakuljic, and A. Yariv, "Chirp multiplication by four wave mixing for wideband swept-frequency sources for high resolution imaging," *Journal of Lightwave Technology*, vol. 28, pp. 2077–2083, Jul 2010.

[41] G. C. Bjorklund, "Frequency-modulation spectroscopy: a new method for measuring weak absorptions and dispersions," *Optics Letters*, vol. 5, pp. 15–17, Jan 1980.

[42] K. Srinivasan and O. Painter, "Linear and nonlinear optical spectroscopy of a strongly coupled microdisk-quantum dot system," *Nature*, vol. 450, pp. 862–U15, Dec 2007.

[43] D. Armani, T. Kippenberg, S. Spillane, and K. Vahala, "Ultra-high-Q toroid microcavity on a chip," *Nature*, vol. 421, pp. 925–928, Feb 2003.

[44] P. E. Barclay, K. Srinivasan, O. Painter, B. Lev, and H. Mabuchi, "Integration of fiber-coupled high-Q SiNx microdisks with atom chips," *Applied Physics Letters*, vol. 89, Sep 2006.

[45] Y. Okawachi, K. Saha, J. S. Levy, Y. H. Wen, M. Lipson, and A. L. Gaeta, "Octave-spanning frequency comb generation in a silicon nitride chip," *Optics Letters*, vol. 36, pp. 3398–3400, Sep 2011.

[46] H. Haus, *Waves and fields in optoelectronics*. Solid state physical electronics series, Prentice-Hall, 1984.

[47] A. Yariv and P. Yeh, *Photonics Optical Electronics in Modern Communications*. oxford University Press, sixth ed., 2007.

[48] K. Vahala, *Optical microcavities*. Advanced series in applied physics, World Scientific Publishing Company, Incorporated, 2004.

[49] M. Heiblum and J. Harris, "Analysis of curved optical waveguides by conformal transformation," *Quantum Electronics, IEEE Journal of*, vol. 11, pp. 75–83, Feb 1975.

[50] M. Oxborrow, "Traceable 2-D finite-element simulation of the whispering-gallery modes of axisymmetric electromagnetic resonators," *IEEE Transactions on Microwave Theory and Techniques*, vol. 55, pp. 1209–1218, Jun 2007.

[51] B. Rahman, F. Fernandez, and J. Davies, "Review of Finite-element Methods for Microwave and Optical Wave-guides," *Proceedings of the IEEE*, vol. 79, pp. 1442–1448, Oct 1991.

[52] J. Jin, *The Finite Element Method in Electromagnetics*. A Wiley-Interscience publication, Wiley, 2002.

[53] V. Raghunathan, W. N. Ye, J. Hu, T. Izuhara, J. Michel, and L. Kimerling, "Athermal operation of Silicon waveguides: spectral, second order and footprint dependencies," *Optics Express*, vol. 18, pp. 17631–17639, Aug 2010.

[54] R. C. Kamikawachi, I. Abe, A. S. Paterno, H. J. Kalinowski, M. Muller, J. L. Pinto, and J. L. Fabris, "Determination of thermo-optic coefficient in liquids with fiber Bragg grating refractometer," *Optics Communications*, vol. 281, pp. 621–625, Feb 2008.

[55] S. Spillane, T. Kippenberg, O. Painter, and K. Vahala, "Ideality in a fiber-taper-coupled microresonator system for application to cavity quantum electrodynamics," *Physical Review Letters*, vol. 91, Jul 2003.

[56] M. Soltani, S. Yegnanarayanan, Q. Li, and A. Adibi, "Systematic Engineering of Waveguide-Resonator Coupling for Silicon Microring/Microdisk/Racetrack Resonators: Theory and Experiment," *Journal of Quantum Electronics*, vol. 46, pp. 1158–1169, Aug 2010.

[57] E. S. Hosseini, S. Yegnanarayanan, A. H. Atabaki, M. Soltani, and A. Adibi, "Systematic design and fabrication of high-Q single-mode pulley-coupled pla-

nar silicon nitride microdisk resonators at visible wavelengths," *Optics Express*, vol. 18, pp. 2127–2136, Feb 2010.

[58] A. Gondarenko, J. S. Levy, and M. Lipson, "High confinement micron-scale silicon nitride high Q ring resonator," *Optics Express*, vol. 17, pp. 11366–11370, Jul 2009.

[59] M. Borselli, T. Johnson, and O. Painter, "Beyond the rayleigh scattering limit in high-q silicon microdisks: theory and experiment," *Optics Express*, vol. 13, pp. 1515–1530, Mar 2005.

[60] A. Yariv, "Universal relations for coupling of optical power between microresonators and dielectric waveguides," *Electronics Letters*, vol. 36, pp. 321–322, Feb 2000.

[61] Y. Xu, Y. Li, R. Lee, and A. Yariv, "Scattering-theory analysis of waveguide-resonator coupling," *Physical Review E*, vol. 62, pp. 7389–7404, Nov 2000.

[62] M. Borselli, T. J. Johnson, and O. Painter, "Accurate measurement of scattering and absorption loss in microphotonic devices," *Optics Letters*, vol. 32, pp. 2954–2956, Oct 2007.

[63] E. S. Hosseini, S. Yegnanarayanan, A. H. Atabaki, M. Soltani, and A. Adibi, "High Quality Planar Silicon Nitride Microdisk Resonators for Integrated Photonics in the Visible Wavelength Range," *Optics Express*, vol. 17, pp. 14543–14551, Aug 2009.

[64] M. Soltani, S. Yegnanarayanan, and A. Adibi, "Ultra-high Q planar silicon microdisk resonators for chip-scale silicon photonics," *Optics Express*, vol. 15, pp. 4694–4704, Apr 2007.

[65] N. Na, H. Frish, I.-W. Hsieh, O. Harel, R. George, A. Barkai, and H. Rong, "Efficient broadband silicon-on-insulator grating coupler with low backreflection," *Optics Letters*, vol. 36, pp. 2101–2103, Jun 2011.

[66] R. Hauffe, U. Siebel, K. Petermann, R. Moosburger, J. Kropp, and F. Arndt, "Methods for passive fiber chip coupling of integrated optical devices," *IEEE Transactions on Advanced Packaging*, vol. 24, pp. 450–455, Nov 2001.

[67] Z. Xiao, F. Luan, T.-Y. Liow, J. Zhang, and P. Shum, "Vertical coupling for silicon nitride waveguides using silicon grating couplers and transitions," in *2012 IEEE Photonics Conference (IPC)*, pp. 202–203, IEEE; Kotura; Rockley Grp; Intel; Cisco; Oracle Labs; Corning; Google; Luxtera, Fiber Chip; Rambus; Analog Devices; PMC; Sinoora; Soitec; Photon Design; Nat Photon; Commun Technol Roadmap; Simgui, 2012. 25th IEEE Photonics Conference (IPC), Burlingame, CA, SEP 23-27, 2012.

[68] T. Mizuno, T. Kitoh, M. Itoh, T. Saida, T. Shibata, and Y. Hibino, "Optical spotsize converter using narrow laterally tapered waveguide for planar lightwave circuits," *Journal of Lightwave Technology*, vol. 22, pp. 833–839, Mar 2004.

[69] K. Ikeda, R. E. Saperstein, N. Alic, and Y. Fainman, "Thermal and Kerr nonlinear properties of plasma-deposited silicon nitride/silicon dioxide waveguides," *Optics Express*, vol. 16, pp. 12987–12994, Aug 2008.

[70] F. Liu, S. Lan, and M. Hossein-Zadeh, "Application of dynamic line narrowing in resonant optical sensing," *Optics Letters*, vol. 36, pp. 4395–4397, Nov 2011.

[71] I. S. Grudinin, V. S. Ilchenko, and L. Maleki, "Ultrahigh optical Q factors of crystalline resonators in the linear regime," *Physical Review A*, vol. 74, Dec 2006.

[72] M. Borselli, T. J. Johnson, and O. Painter, "Accurate measurement of scattering and absorption loss in microphotonc devices," *Optics Letters*, vol. 32, pp. 2954–2956, Oct 2007.

[73] M.-C. Tien, J. F. Bauters, M. J. R. Heck, D. T. Spencer, D. J. Blumenthal, and J. E. Bowers, "Ultra-high quality factor planar Si3N4 ring resonators on Si substrates," *Optics Express*, vol. 19, pp. 13551–13556, Jul 2011.

[74] T. Xu, M. S. Wheeler, H. E. Ruda, M. Mojahedi, and J. S. Aitchison, "The influence of material absorption on the quality factor of photonic crystal cavities," *Optics Express*, vol. 17, pp. 8343–8348, May 2009.

[75] J. Lee, C. Park, and G. Whitesides, "Solvent compatibility of poly (dimethylsiloxane) based microfluidic devices," *Analytical Chemistry*, vol. 75, pp. 6544–6554, Dec 2003.

[76] X. Quan and E. S. Fry, "Empirical equation for the index of refraction of seawater," *Applied Optics*, vol. 34, pp. 3477–3480, Jun 1995.

[77] C. A. Barrios, B. Sanchez, K. B. Gylfason, A. Griol, H. Sohlstrom, M. Holgado, and R. Casquel, "Demonstration of slot-waveguide structures on silicon nitride/silicon oxide platform," *Optics Express*, vol. 15, pp. 6846–6856, May 2007.

[78] C. J. de Haas, P.-J. Haas, K. P. van Kessel, and J. A. van Strijp, "Affinities of different proteins and peptides for lipopolysaccharide as determined by biosensor technology," *Biochemical and Biophysical Research Communications*, vol. 252, no. 2, pp. 492 – 496, 1998.

[79] P. C. Weber, D. H. Ohlendorf, J. J. Wendoloski, and F. R. Salemme, "Structural origins of high-affinity biotin binding to streptavidin," *Science*, vol. 243, no. 4887, pp. pp. 85–88, 1989.

[80] M. S. Luchansky and R. C. Bailey, "High-Q Optical Sensors for Chemical and Biological Analysis," *Analytical Chemistry*, vol. 84, pp. 793–821, Jan 2012.

[81] G. Worster, *Understanding Fluid Flow*. AIMS Library Series, Cambridge University Press, 2009.

[82] A. Kamholz and P. Yager, "Theoretical analysis of molecular diffusion in pressure-driven laminar flow in microfluidic channels," *Biophysical Journal*, vol. 80, pp. 155–160, Jan 2001.

[83] S. Mitra and S. Chakraborty, *Microfluidics and Nanofluidics Handbook: fabrication, implementation, and applications*. Microfluidics and Nanofluidics Handbook, CRC PressINC, 2011.

[84] T. Gervais and K. Jensen, "Mass transport and surface reactions in microfluidic systems," *Chemical Engineering Science*, vol. 61, pp. 1102–1121, Feb 2006.

[85] M.-C. Amann, T. Bosch, M. Lescure, R. Myllylä, and M. Rioux, "Laser ranging: a critical review of usual techniques for distance measurement," *Optical Engineering*, vol. 40, no. 1, pp. 10–19, 2001.

[86] E. Strzelecki, D. Cohen, and L. Coldren, "Investigation of tunable single frequency diode lasers for sensor applications," *Lightwave Technology, Journal of*, vol. 6, pp. 1610 –1618, Oct. 1988.

[87] A. Schweinsberg, S. Hocd, N. N. Lepeshkin, R. W. Boyd, C. Chase, and J. E. Fajardo, "An environmental sensor based on an integrated optical whispering gallery mode disk resonator," *Sensors and Actuators B: Chemical*, vol. 123, no. 2, pp. 727 – 732, 2007.

[88] M. Gora, K. Karnowski, M. Szkulmowski, B. J. Kaluzny, R. Huber, A. Kowalczyk, and M. Wojtkowski, "Ultra high-speed swept source oct imaging of the anterior segment of human eye at 200 khz with adjustable imaging range," *Optics Express*, vol. 17, pp. 14880–14894, Aug 2009.

[89] K. Yamada, H. Fukuda, T. Tsuchizawa, T. Watanabe, T. Shoji, and S. Itabashi, "All-optical efficient wavelength conversion using silicon photonic wire waveguide," *Photonics Technology Letters*, vol. 18, pp. 1046–1048, May-Jun 2006.

[90] R. Espinola, J. Dadap, R. Osgood, S. McNab, and Y. Vlasov, "C-band wavelength conversion in silicon photonic wire waveguides," *Optics Express*, vol. 13, pp. 4341–4349, May 30 2005.

[91] W. Mathlouthi, H. Rong, and M. Paniccia, "Characterization of efficient wavelength conversion by four-wave mixing in sub-micron silicon waveguides," *Optics Express*, vol. 16, pp. 16735–16745, Oct 2008.

[92] M. Foster, A. Turner, J. Sharping, B. Schmidt, M. Lipson, and A. Gaeta, "Broadband optical parametric gain on a silicon photonic chip," *Nature*, vol. 441, pp. 960–963, Jun 22 2006.